

EROSION OF SOFT MUDS BY WAVES

BY

P.-Y. MAA

A DISSERTATION PRESENTED TO THE
GRADUATE SCHOOL OF THE UNIVERSITY OF FLORIDA
IN PARTIAL FULFILLMENT OF THE REQUIREMENTS
FOR THE DEGREE OF DOCTOR OF PHILOSOPHY

UNIVERSITY OF FLORIDA

1986

ACKNOWLEDGEMENTS

The author would like to express his sincerest appreciation to his research advisor and supervisory committee chairman, Dr. A.J. Mehta, Associate Professor of Civil Engineering and of Coastal and Oceanographic Engineering, for his continuous guidance and encouragement throughout this research. Appreciation is also extended for the valuable advice and suggestions of the supervisory committee cochairman, Dr. B. A. Christensen, Professor of Civil Engineering, as well as the guidance received from the other committee members: Dr. R. G. Dean, Graduate Research Professor of Coastal and Oceanographic Engineering, Dr. B. A. Benedict, Professor of Civil Engineering, and Dr. A. K. Varma, Professor of Mathematics.

Sincere thanks also go to Dr. R. A. Dalrymple, Dr. J. T. Kirby, Dr. M. C. McVay, Dr. L. E. Malvern and Mr. M. Ross for their suggestions and help in this study.

Special thanks go to Mr. Vernon Sparkman, Mr. C. Broward, and other staff of the Coastal Engineering Laboratory for their assistance with the experiments performed during this research. In addition, the author thanks Ms. L. Lehmann and Ms. H. Twedell of the Coastal Engineering Archives for their assistance.

Gratitude is due to the U.S. Army Corps of Engineers Waterway Experiment Station, Vicksburg, Mississippi, for their financial support of this research under Contract DACW39-84-C-0013.

Finally, the author thanks his wife, Tai-Fang, for her love,
encouragement and patience, and his parents for their love and support.

TABLE OF CONTENTS

	Page
ACKNOWLEDGEMENTS.....	ii
LIST OF TABLES.....	vii
LIST OF FIGURES.....	viii
LIST OF SYMBOLS.....	xv
ABSTRACT.....	xx
CHAPTERS	
1 INTRODUCTION.....	1
1.1 Significance of Wave Erosion of Soft Mud.....	1
1.2 Factors Characterizing the Wave Erosion Process.	3
1.3 Objectives and Scope of the Present Study.....	7
1.4 Outline of Presentation.....	8
2 BACKGROUND STUDY.....	10
2.1 Introduction.....	10
2.2 Wave Erosion/Resuspension.....	10
2.3 Constitutive Models for Soft Mud.....	17
2.3.1 Nature of Clayey Soil.....	18
2.3.2 Elastic Model.....	21
2.3.3 Poro-elastic Model with Coulomb Friction,	21
2.3.4 Viscous Fluid Model.....	22
2.3.5 Viscoplastic Model.....	26
2.3.6 Viscoelastic Model.....	32
2.4 Bed Shear Stress.....	36
2.5 Wave Diffusion Coefficient.....	39
3 NUMERICAL ONE-DIMENSIONAL BINGHAM FLUID MODEL.....	44
3.1 Introduction.....	44
3.2 Problem Formulation.....	44
3.3 Results.....	50
3.4 Conclusion.....	55
4 TWO-DIMENSIONAL MULTI-LAYERED HYDRODYNAMIC MODEL.....	57
4.1 Introduction.....	57
4.2 Formulation.....	57
4.3 Solution Technique.....	64
4.4 Input Data.....	66

4.5	Model Results.....	69
4.5.1	Velocity.....	70
4.5.2	Pressure.....	73
4.5.3	Shear Stress.....	75
4.5.4	Water Wave Decay.....	77
4.5.5	Interfacial Wave Amplitude.....	78
4.6	Resonance Characteristics.....	80
5	VISCOELASTIC PROPERTY TESTS.....	87
5.1	Introduction.....	87
5.2	Relaxation Test.....	87
5.2.1	Apparatus.....	88
5.2.2	Procedure.....	92
5.2.3	Results.....	93
5.3	Tests for Material Constants of Voigt Element.....	97
5.4	Tests for Rheological Properties of Bingham Fluid Model.....	102
6	EROSION TESTS: FACILITY AND PROCEDURE.....	105
6.1	Introduction.....	105
6.2	Wave Flume	105
6.2.1	Wave Reflection.....	107
6.2.2	Wave Horizontal Velocity.....	108
6.2.3	Wave Decay for Rigid Bed.....	108
6.3	Sediment.....	109
6.3.1	Kaolinite.....	109
6.3.2	Cedar Key Mud.....	110
6.4	Eroding Fluid.....	113
6.5	Instrumentation.....	116
6.5.1	Wave Gauges.....	116
6.5.2	Pressure Transducers.....	116
6.5.3	Light Meter.....	118
6.5.4	Data Acquisition System.....	120
6.5.5	Suspended Sediment Sampler.....	122
6.5.6	Bed Sampler.....	124
6.5.7	Current Meter.....	124
6.6	Procedure.....	125
6.6.1	Process of the Digital Data.....	126
6.6.2	Suspension Samples.....	128
6.6.3	Wave-averaged Mud Surface Elevation.....	130
7	EROSION TESTS: RESULTS AND DISCUSSION.....	131
7.1	Introductory Note.....	131
7.2	Results.....	131
7.2.1	Bed Density.....	131
7.2.2	Pressure Response.....	137
7.2.3	Instantaneous Sediment Concentration.....	142
7.2.4	Time-averaged Sediment Concentration.....	146
7.2.5	Wave-averaged Mud Surface Elevation.....	151

7.3	Wave Erosion and Entrainment.....	156
7.3.1	Erosion.....	156
7.3.2	Erosion Rate.....	165
7.3.3	Entrainment.....	174
7.4	Dye Diffusion Tests.....	182
7.5	Concluding Comments.....	185
8	SUMMARY, CONCLUSIONS AND RECOMMENDATIONS.....	190
8.1	Summary and Conclusions.....	190
8.2	Recommendations for Future Study	197
APPENDICES		
A	BOUNDARY CONDITIONS FOR MULTI-LAYERED MODEL.....	200
B	COMPARISON BETWEEN PREDICTION AND MEASUREMENT: DYNAMIC PRESSURE AND HORIZONTAL VELOCITY.....	208
C	MISCELLANEOUS CONSIDERATIONS FOR THE WAVE EROSION EXPERIMENT.....	222
D	DATA ON EROSION TESTS.....	238
REFERENCES.....		270
BIOGRAPHICAL SKETCH.....		277

LIST OF TABLES

	Page
2-1 Diffusion Coefficients in Wave Flow.....	42
4-1 Input Thickness for Each Layer.....	68
4-2 Interfacial Shear Stresses and Mud Wave Amplitudes.....	78
5-1 Vane Dimensions.....	91
5-2 Coefficients of the Correlation Equations.....	101
6-1 Sediment Properties.....	113
6-2 Composition of Clay Fraction.....	113
6-3 Chemical Composition of the Eroding Fluid.....	115
6-4 Eroding Fluid Properties.....	115
6-5 Wave Conditions for Erosion Tests.....	129
7-1 Average Erosion and Entrainment Rates.....	163
7-2 Coefficients for the Erosion Function.....	171
7-3 Measured Diffusion Coefficient in the Upper Layer.....	179
7-4 Constants for Steady Flow Erosion Function.....	187

LIST OF FIGURES

	Page
1-1 Schematic Depiction of Response of Wave-Mud Interaction.....	5
2-1 A Plot of the Suspended Solids and Bed Shear Stress for a Wave Resuspension Test.....	12
2-2 Measured Suspended Sediment Concentration Profiles from a Wave Resuspension Test.....	14
2-3 Shear Stress-Strain Loop for Clay under Cyclic Load.....	19
2-4 Energy Dissipation Ratio λ versus Shear Strain.....	19
2-5 Shear Stress-Strain Loops and Effects of Cyclic Load....	20
2-6 A Plot of the Horizontal Velocity Amplitude Profiles by Using the Two-Layered Viscous Fluid Model.....	25
2-7 Relationship between Yield Strength and Sediment Concentration.....	28
2-8 Relationship between Apparent Viscosity and Sediment Concentration.....	29
2-9 System Diagram for Simple Viscoelastic Models and Response under Constant Loading.....	33
2-10 Viscoelastic Behavior of Clay.....	33
2-11 Wave Friction Factor.....	38
3-1 System Diagram for the 1-D Numerical Bingham Fluid Model.....	45
3-2 Horizontal Velocity Profiles for Two Steady Flows. (a) Two-Layerd Viscous Fluid; (b) Bingham Fluid with Exponentially Increasing K and v.....	51
3-3 Comparison of the Wave Velocity Amplitude Profiles from 1-D model and Dalrymple and Liu's Model with $p_1 = 1000 \text{ kg/m}^3$, $p_2 = 1160 \text{ kg/m}^3$, $v_1 = 1 \times 10^{-6}$ and $v_2 = 2 \times 10^{-4} \text{ m}^2/\text{s}$	52
3-4 Wave Velocity Profiles for the Water-Bingham Fluid System with $T = 3 \text{ sec}$. (a) $H = 2.5 \text{ cm}$ and $k_{im} = 0.0011 \text{ m}^{-1}$; (b) $H = 5 \text{ cm}$ and $k_{im} = 0.016 \text{ m}^{-1}$	54

3-5	Shear Stress versus Shear Strain Rate for Kaolinite Bed with Two-Day Consolidation Period.....	56
3-6	Wave Velocity Profiles for Water-Bingham Fluid System with Measured Yield Strength and Viscosity.....	56
4-1	Schematic Figure for the Multi-Layered Model.....	58
4-2	Layout of the Coefficient Matrix for the Multi-Layered Model.....	65
4-3	Comparison of Computed Bed Shear Stress (model and Kamphuis) at the Interface to Determine the Eddy Viscosity of Water.....	68
4-4	Comparison of the Model Prediction and Measurement for Run 1-2. (a) Velocity; (b) Pressure.....	71
4-5	Comparison of the Model Prediction and Measurement for Run 5-2. (a) Velocity; (b) Pressure.....	72
4-6	An Example of the Model-Predicted Shear Stress Profile..	76
4-7	Comparison of the Measured and Predicted Wave Decay Coefficient.....	79
4-8	Non-Dimensional Interfacial Wave Amplitude versus Complex Reynolds Number.....	82
4-9	Resonance Phénoménon of Water-Mud System. (a) with $d_2 = 0.05$ m; (b) with $d_2 = 0.14$ m.....	84
4-10	Frequency Response of the Water-Mud System. Mud is Assumed as (a) Viscoelastic Material; (b) Viscous Fluid.	85
5-1	Apparatus for Relaxation Tests and Viscoelastic Constant Measurement. (a) System Diagram; (b) Top View..	88
5-2	Structure of Brookfield Viscometer.....	89
5-3	Miniature Vanes and Sample Container.....	90
5-4	A Plot of the Residual Torque and Angular Displacement versus Elapsed Time for Run 1, Kaolinite with One-Week Consolidation Period.....	94
5-5	A Plot of the Residual Torque and Angular Displacement versus Elapsed Time for Run 4, Cedar Key Mud with One-Week Consolidation Period.....	95

5-6	A Plot of the Residual Torque and Angular Displacement versus Elapsed Time for Run 5, Cedar Key Mud with Two-Day Consolidation Period.....	96
5-7	A Plot of Shear Stress against Shear Strain for Determination of Viscoelastic Constant.....	99
5-8	Relationship between Viscoelastic Constants and Mud Dry Density. (a) Viscosity; (b) Shear Modulus.....	100
5-9	Shear Stress versus Shear Strain Rate obtained from Kaolinite Bed, Run 1, 6.2 cm below Mud Surface.....	104
6-1	Wave Flume for the Erosion Experiments.....	106
6-2	Water-Mud Interface Elevations during Deposition and Consolidation of the Kaolinite Slurry.....	111
6-3	Dispersed Grain Size Distribution for Sediment in Runs 4, 5, and 6.....	114
6-4	Pressure Transducer, Druck Model PDCR 135/A/F.....	117
6-5	System Diagram of the Photo-Sensing Light Meter.....	119
6-6	Suspended Sediment Sampler.....	123
6-7	Wave Loading for the Erosion Test, Run 3.....	127
6-8	A Plot of Wave Height Decay in the Wave Flume.....	129
7-1	Measured Mud Density Variation due to Wave Action, Run 1.....	132
7-2	Volumetric Swelling of Mud Bed Caused by Wave Action. (a) Run 1; (b) Run 4.....	134
7-3	Depth-Averaged Bed Density Variation Caused by Wave Action.....	135
7-4	Dimensionless Mud Dry Density Profiles. (a) Kaolinite; (b) Cedar Key Mud.....	136
7-5	Instantaneous Pressure Response in the Kaolinite Bed, Run 1. (a) Wave Profile; (b) Pressure.....	138
7-6	Average Pressure Response in the Kaolinite Bed, Run 1. (a) Dynamic Pressure Fluctuation; (b) Wave-Averaged Pressure.....	140

7-7 Variation of Dimensionless Apparent Bulk Density Caused by Wave Action, Run 1, Normalized by the Initial Value..	141
7-8 Instantaneous Sediment Concentration Response in the Water Column. (a) Run 3; (b) Run 5.....	143
7-9 Wave-Averaged Response from Light Meter during Wave Erosion Process.....	144
7-10 Average Sediment Concentration Fluctuation Detected by the Light Meter during Wave Erosion Process.....	145
7-11 Sample Profiles for the Suspended Sediment Concentration for Run 1. (a) at STA. B; (b) at STA. D...	147
7-12 Sample Profiles for the Suspended Sediment Concentration for Run 5. (a) at STA. B; (b) at STA. D...	148
7-13 Longitudinal Variation of the Depth-Averaged Sediment Concentration, Run 4.....	150
7-14 Mud Surface Profiles at Selected Times. (a) Run 1.....	152
7-14 (continued). (b) Run 2; (c) Run 3.....	153
7-15 Response of the Spatially-Averaged Mud Surface Elevation. (a) Kaolinite Bed; (b) Cedar Key Mud Bed....	155
7-16 Wave Erosion/Entrainment Behavior for Kaolinite. (a) Run 1.....	157
7-16 (continued). (b) Run 2.....	158
7-16 (continued). (c) Run 3.....	159
7-17 Wave Erosion/Entrainment Behavior for Cedar Key Mud. (a) Run 4; (b) Run 5.....	160
7-17 (continued). (b) Run 6.....	161
7-18 Shear Strength Profiles for Resistance of Wave Erosion. (a) Kaolinite Bed; (b) Cedar Key Mud.....	167
7-19 Influence of the Period of Consolidation on Erosion Resistance. (a) Kaolinite; (b) Cedar Key Mud.....	168
7-20 Erosion Rate versus Dimensionless Excess Shear Stress. (a) Kaolinite; (b) Cedar Key Mud.....	170
7-21 Dimensionless Erosion Rate versus Dimensionless Excess Shear Stress.....	172

7-22 Erosion Rate versus Bed Shear Stress, Run 5.....	173
7-23 Suspended Sediment Concentration Profiles at Steady State. (a) Run 1; (b) Run 2.....	175
7-23 (continued). (c) Run 3; (d) Run 4.....	176
7-23 (continued). (e) Run 5; (f) Run 6.....	177
7-24 Settling Velocity versus Sediment Concentration for Kaolinite.....	179
7-25 Spatially-Averaged Variation of (a) the Distance between the Lowest Tap and Mud Surface; (b) Sediment Concentration at the Lowest Tap.....	181
7-26 Diffusion of a Line-Source Dye in a Wave Flow with $T = 1.2\text{ s}$, $H = 7\text{ cm}$. (a) $t = 0.5\text{ s}$; (b) $t = 5\text{ s}$; (c) $t = 14\text{ s}$; (d) $t = 20\text{ s}$	183
B-1 Comparison between Observed and Predicted Horizontal Velocity Amplitudes in the Bed.....	210
B-2 Comparison of Model Prediction and Measurement for Run 1-1. (a) Velocity; (b) Pressure.....	211
B-3 Comparison of Model Prediction and Measurement for Run 2-1. (a) Velocity; (b) Pressure.....	212
B-4 Comparison of Model Prediction and Measurement for Run 2-2. (a) Velocity; (b) Pressure.....	213
B-5 Comparison of Model Prediction and Measurement for Run 3-1. (a) Velocity; (b) Pressure.....	214
B-6 Comparison of Model Prediction and Measurement for Run 3-2. (a) Velocity; (b) Pressure.....	215
B-7 Comparison of Model Prediction and Measurement for Run 4-1. (a) Velocity; (b) Pressure.....	216
B-8 Comparison of Model Prediction and Measurement for Run 4-2. (a) Velocity; (b) Pressure.....	217
B-9 Comparison of Model Prediction and Measurement for Run 5-1. (a) Velocity; (b) Pressure.....	218
B-10 Comparison of Model Prediction and Measurement for Run 6-1. (a) Velocity; (b) Pressure.....	219
B-11 Comparison of Model Prediction and Measurement for Run 6-2. (a) Velocity; (b) Pressure.....	220

B-12 Comparison of Model Prediction and Measurement for Run 6-3. (a) Velocity; (b) Pressure.....	221
C-1 Normalized Frequency Response of the Current Meter.....	225
C-2 Circuit Diagram for the LED Driver of Light Meter.....	227
C-3 Light Meter Probe.....	228
C-4 Circuit Diagram for the Pre-Amplifier of Light Meter....	230
C-5 Circuit Diagram for the Main Processor of Light Meter...	231
C-6 Light Meter Calibration Device.....	232
C-7 Light Meter Calibration Curves for Kaolinite.....	233
C-8 Light Meter Calibration Curves for Cedar Key Mud.....	234
C-9 Response Function of the Low-Pass Filter.....	236
C-10 Comparison of Data Record with/without the Low-Pass Filter.....	237
D-1 Wave Loading for the Wave Erosion Test, Run 1.....	253
D-2 Wave Loading for the Wave Erosion Test. (a) Run 2; (b) Run 4.....	254
D-3 Wave Loading for the Wave Erosion Test. (a) Run 5; (b) Run 6.....	255
D-4 Wave-Averaged Pressure Response in the Mud Bed. (a) Run 2; (b) Run 3.....	256
D-5 Wave-Averaged Pressure Response in the Mud Bed. (a) Run 4; (b) Run 5.....	257
D-6 Wave-Averaged Pressure Response in the Mud Bed, Run 6...	258
D-7 Average Dynamic Pressure Fluctuation in the Mud Bed, Run 2.....	258
D-8 Average Dynamic Pressure Fluctuation in the Mud Bed. (a) Run 3; (b) Run 4.....	259
D-9 Average Dynamic Pressure Fluctuation in the Mud Bed. (a) Run 5; (b) Run 6.....	260
D-10 Average Apparent Bulk Density Variation. (a) Run 2; (b) Run 3.....	261

D-11 Average Apparent Bulk Density Variation. (a) Run 4; (b) Run 5.....	262
D-12 Average Apparent Bulk Density Variation, Run 6.....	263
D-13 Variation of Kaolinite Bed Density Profile Due to Wave Action, Run 2.....	264
D-14 Variation of Kaolinite Bed Density Profile Due to Wave Action, Run 3.....	265
D-15 Variation of Cedar Key Mud Bed Density Profile Due to Wave Action, Run 4.....	266
D-16 Variation of Cedar Key Mud Bed Density Profile Due to Wave Action, Run 5.....	267
D-17 Variation of Cedar Key Mud Bed Density Profile Due to Wave Action, Run 6.....	268
D-18 Wave-Averaged Response from Light Meter, Run 6. (a) Sediment Concentration; (b) Sediment Concentration Fluctuation.....	269

LIST OF SYMBOLS

- a: Wave amplitude in the x wave propagation direction.
- a_0 : Wave amplitude at $x = 0$.
- a_b : Semi-excursion distance of a water particle just outside δ .
- A/D: Analog to digital.
- b_{oi} : The i-th interfacial mud wave amplitude at $x = 0$, a complex no.
- C: Suspended sediment concentration (g/l).
- c: Complex coefficient matrix $c(i,j)$ or wave celerity.
- c_d : Damping coefficient in the disk-shaft system.
- c_g : Wave group velocity.
- $\langle c_T \rangle$: Average suspended sediment concentration at the 3 lowest taps.
- d_i : Thickness of i-th layer.
- d_m : Total thickness of mud bed.
- D: Rate of deformation tensor, $D_{ij} = \frac{1}{2} (\frac{\partial u_i}{\partial x_j} + \frac{\partial u_j}{\partial x_i})$.
- D' : Deviator part of the rate of deformation tensor, $D'_{ij} = D_{ij} - \frac{1}{3} D_{rr}$.
- D_m : Apparent Diffusion coefficient (molecular diffusion + turbulent diffusion + dispersion).
- D_v : Diameter of the miniature vane.
- D_{90} : Grain size through which 90% of the total soil mass is finer than this size.
- E' : Deviator part of the small strain tensor, $E'_{ij} = E_{ij} - \frac{1}{3} E_{rr}$.
- E: Small strain tensor, $E_{ij} = \frac{1}{2} (\frac{\partial e_i}{\partial x_j} + \frac{\partial e_j}{\partial x_i})$.
- \dot{e} : Rate of strain.
- \dot{E}' : Rate of shear strain.
- E_n : Wave energy.
- E_d : Time-averaged energy dissipation per unit surface area.

- f_w : Wave friction factor.
- g : Acceleration due to gravity.
- g/l : gm/liter.
- G : Shear Modulus of elasticity.
- G_0 : A constant coefficient.
- h : Water depth.
- H : Wave height.
- H_v : Height of the miniature vane.
- i : Free index.
- j : Free index or $\sqrt{-1}$.
- J : Grid number at the water surface.
- k : Complex wave number, $k = k_r + j k_{im}$.
- k_{im} : Imaginary part of the complex wave number, also the wave decay coefficient, defined as $a(x) = a_0 \exp(-k_{im} \Delta x)$.
- k_r : The real part of the complex wave number, $k_r = 2\pi/L$.
- K : Yield strength of Bingham Fluid.
- L : Wave length.
- m : Constant coefficient, or free index.
- M_n : Sediment mass entrained into water column measured by water samples withdrawn from water column.
- M_r : Sediment mass eroded by waves.
- n : Constant coefficient.
- N : Number of layers in the hydrodynamic model presented in Chapter 4.
- p : Dynamic pressure.
- p^0 : Correction term for the static pressure due to density difference.
- p^t : Total pressure;
- \hat{p} : Dynamic pressure amplitude.
- r : Radius, or free index.

R: Complex Reynolds number, $R = R_r + j R_{im}$.

R_w : Wave Reynolds number, $R_w = u_b^2 / \sigma v_e$.

RMS: Root mean square.

S_u : Undrained shear strength.

SWL: Still water level.

t: Time.

T: Wave period or stress tensor.

T' : Deviator part of the stress tensor, $T'_{ij} = T_{ij} - \frac{1}{3} T_{rr}$.

T_{dc} : Period of Consolidation of a sediment slurry.

$\dot{\tau}'$: Rate of shear stress.

u_i : Velocity in the x_i direction; horizontal velocity for i-th layer.

u_b : Horizontal velocity amplitude just outside the boundary layer.

\hat{u}_i : Horizontal velocity amplitude.

w_i : Vertical velocity.

\hat{w}_i : Vertical velocity amplitude.

\hat{w}'_i : First derivative of \hat{w}_i with respect to z.

\hat{w}''_i : Second derivative of \hat{w}_i with respect to z.

w_s : Settling velocity of a sediment particle or floc.

x: Longitudinal direction, or x_1 .

x_i : Cartesian coordinate using index notation, $i = 1, 2, 3$.

X: Column matrix containing $A_1, B_1, \dots, C_N, D_N$, and $b_{o,N-1}$.

y: Lateral direction, or x_2 .

z: Vertical coordinate, or x_3 , starting from the water surface, positive upward.

z' : Vertical coordinate, starting from mud surface, positive downward.

z'' : Vertical coordinate, starting from bed, positive upward.

z_m : An elevation where a pressure transducer was mounted.

z_n : An elevation where a pressure transducer was mounted.

$\langle \Delta h \rangle$: Average distance from the 3 lowest taps to the bed surface.

Δt : Increment in the time domain.

Δx : Increment in the x direction.

Δz : Increment in the z direction.

α : Constant coefficient.

α_0 : Constant coefficient.

β : Constant coefficient.

ω : Wave frequency, $\omega = 2\pi/T$.

δ : Thickness of wave boundary layer.

δ_L : Thickness of the viscous wave boundary layer.

ρ : Material density.

ρ_B : Bulk density of mud.

ρ_D : Dry density of mud.

$\bar{\rho}_D$: Depth-averaged dry density of mud at a time.

$\bar{\rho}_{D0}$: Depth-averaged dry density of mud before wave loading.

ρ_e : Average apparent bulk density of mud between two sensors.

ρ_{e0} : ρ_e value at the beginning of wave loading.

ρ_s : Density of sediment grain.

ρ_w : Density of water.

ρ' : Normalized apparent bulk density between two sensors, $= \rho / \rho_{e0}$

τ : Shear stress.

$\hat{\tau}$: Shear stress amplitude.

$\tau_b(x)$: Bed shear stress amplitude at $x=x$.

τ_{bo} : Bed shear stress amplitude at $x=0$.

$\langle \tau_b \rangle$: Spatially-averaged bed shear stress amplitude.

- τ_c : Critical shear stress. The minimum bed shear stress that will cause erosion of sediment bed.
- τ_e : Excess shear stress, $\tau_e = \tau_b - \tau_s(z')$.
- τ_s : Erosion resistance or bed shear strength.
- τ_{so} : Erosion resistance at the bed surface.
- $\bar{\tau}_s$: Depth-averaged (top 5 mm) erosion resistance of mud bed.
- n : Water surface displacement.
- ϵ : A constant eddy viscosity coefficient.
- ϵ_o : Erosion rate constant for wave flow.
- ϵ_f : Erosion rate constant for steady flow.
- ϵ_n : Rate of upward entrainment of sediment.
- ϵ_r : Erosion rate.
- ξ : Interfacial wave displacement, $\xi = b_0 e^{j(kx-\omega t)}$.
- ζ_i : Displacement in the x_i direction.
- μ : Dynamic viscosity.
- μ_e : Apparent dynamic viscosity, $\mu_e = \rho_B v_e$.
- ν_o : Constant coefficient.
- ν_w : Dynamic viscosity of water.
- ν_m : Dynamic viscosity of mud.
- ν : Kinematic viscosity.
- v_e : Apparent kinematic viscosity.
- θ : Angular shear strain.
- $d\theta/dt$ or $\dot{\theta}$: Rate of angular shear strain.
- II_D' : Second invariant of the deviator part of D' .
- ϕ : Diameter.
- Ω : Angular speed.
- λ : Energy dissipation ratio.

Abstract of Dissertation Presented to the Graduate School
of the University of Florida in Partial Fulfillment of the
Requirements for the Degree of Doctor of Philosophy

EROSION OF SOFT MUDS BY WAVES

By

P.W.Y. Maa

August 1986

Chairman: Dr. A. J. Mehta
Cochairman: Dr. B. A. Christensen
Major Department: Civil Engineering

The influence of water waves on soft muds can result in high turbidity and significant wave attenuation. A multi-layered 2D hydrodynamic model was developed and experimentally verified in order to evaluate the bed shear stress at the water-mud interface, for interpreting results on interfacial sediment erosion. In the model, the mud bed was discretized into layers of constant density, viscosity and shear modulus of elasticity. The last two parameters characterize mud as a linear viscoelastic material. Layering was essential for simulating the depth-varying bed properties. For given non-breaking, regular waves, the model gives profiles of velocities, pressure and shear stress as well as wave attenuation coefficient.

Laboratory flume tests of sediment erosion under waves were conducted using a commercial kaolinite and an estuarine mud. Sediment concentration response in the water column and the variation of total eroded sediment mass with elapsed time under different wave loading were measured. Additional tests were conducted to evaluate the viscoelastic constants of the selected sediments.

Two types of erosion process were identified. The first is applicable to a partially consolidated bed, in which erosion resistance, $\tau_s(z')$, increases with depth, z' , and the erosion rate, ϵ_r , decreases as erosion proceeds. The proposed erosion rate function is

$$\frac{\epsilon_r}{\epsilon_0} = \left[\frac{\tau_b}{\tau_s(z')} + 1 \right]^\alpha, \quad \tau_b > \tau_s(z')$$

where τ_b is the bed shear stress, ϵ_0 is a rate constant and α is an empirical exponent. The average value of α for all test data was close to one, which reveals a simple, linear relationship. The second type of erosion process is for a newly deposited bed, in which the erosion resistance is a small constant, and the erosion proceeds at a constant rate.

Measured suspended sediment concentration profiles indicated relatively low concentrations in the upper 80% of the water column and the formation of a high density fluid mud layer near the bed. Low upward diffusion, high longitudinal dispersion and advective transport characterized the near-bed layer. Bed softening and fluid-mud-generating capacity of waves appear to be significant features of the wave erosion process.

CHAPTER 1 INTRODUCTION

1.1 Significance of Wave Erosion of Soft Muds

Most estuaries and several reaches of shorelines have soft muddy bottoms consisting primarily of silt and clay comprising a cohesive sediment. With the rapid development of coastal and estuarine harbors and increasing concerns from the environmental protection point of view, the need to predict the erosion of soft mud has increased. Basically, in these environments, tidal currents and water waves are the two forces that cause erosion of sediments. Extensive studies of the erosion behavior of cohesive sediment under tides, in quasi-steady flow, have been conducted by various researchers. Expressions of the erosion rate have been proposed (Partheniades, 1965; Krone, 1962; Mehta et al., 1982; Parchure, 1984). Mathematical models for cohesive sediment transport by current are also available (Odd and Owen, 1972; Ariathurai, 1974; Hayter, 1983). However, the influence of water waves on the erosion of cohesive sediment has by and large remained unexplored. Only a few important laboratory studies have been made (Alishahi and Krone, 1964; Anderson, 1972; Jackson, 1973; Thimakorn, 1980). However, data obtained have been scattered and incomplete. A comprehensive and systematic study of wave erosion behavior is necessary to elucidate the mechanism of the wave erosion process. Here the

physical processes which have been observed at muddy coasts are introduced first.

The most obvious feature of the muddy coastal zone is the lack of large waves due to the great damping ability of the soft mud beds (Wells, 1983). This has been noticed since the early 1800s in southwest India and northeastern South America. The damping ability comes from the motion of the mud bed, a phenomenon observed in both laboratory and field studies (Tubman and Suhayda, 1976; Schuckman and Yamamoto, 1982). An immediate benefit of this high damping ability is protection of shorelines. Fishermen in the Gulf of Mexico have taken refuge during stormy weather in waters over the "mud hole," a localized accumulation of soft mud bottom (Morgan *et al.*, 1953).

High suspended sediment concentration (0.1 -2 g/l) is another feature of soft muddy coasts even in calm weather (wave height ~ 10 cm). In severe wave conditions, the entire soft mud can be stirred up resulting in great turbidity.

The mechanism of wave transformation when propagating over soft mud beds and the resulting erosion of mud are important to both coastal and environmental engineers because waves and the associated sediment transport are major factors for design of most coastal waterways and harbors, e.g., the maintenance of navigation channels, and the control of pollutants. However, studies on this subject are limited apparently because the change of characteristics of surface water waves caused by the dissipation of wave energy in the mud and resuspension of mud are interlinked and complex. Added complexities arise from the influences of physicochemical properties of the sediment and the fluid (Mehta,

1983), the effect of bed structure (Parchure, 1984), and the time dependence of bed structure (Schuckman and Yamamoto, 1982) on the overall problem.

1.2 Factors Characterizing the Wave Erosion Process

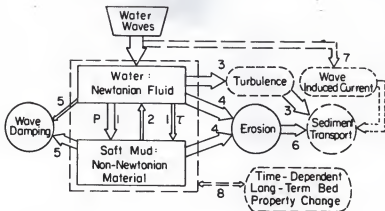
A summary of the parameters which influence the wave erosion problem is presented in Fig. 1-1. Thick arrows show the dominant processes, and thin arrows are the less important processes. Dashed lines represent processes or parameters that are known to have influences on the dynamics of wave-mud interaction, but which were not considered in detail in this study. The responses of this wave-mud system, contained in the dashed rectangular box, subjected to dynamic wave loading, are dependent on the characteristics of both wave and mud. Pressure and shear stress at the water-mud interface are the two forces that have linked the water and mud bed together. Two immediate responses are wave damping and erosion, shown in the circles. The contribution of pressure fluctuation at the interface is mainly responsible for the motion of the mud beds, and therefore, wave damping. Shear stresses mainly contribute to the erosion process, a conclusion from steady flow studies. Turbulence in the water flow influences the bed shear stress and the sediment transport process as well. Erosion is dependent on the properties related to waves, i.e., bed shear stress, as well as erosion resistance of the mud material, i.e., shear strength. Therefore, development of a hydrodynamic model that can simulate the water wave decay and the interfacial shear stress (also called bed shear stress, τ_b) is necessary before an erosion rate

expression can be developed. With τ_b known, the results from wave erosion tests can be better interpreted.

Defining the properties of soft mud beds is in itself an interesting subject. Such beds were assumed to be a viscous fluid by Gade (1958) and Dalrymple and Liu (1978); an elastic material by Mallard and Dalrymple (1977) and Dawson (1978); a poro-elastic material by Yamamoto and Takahashi (1985); a viscoelastic material by MacPherson (1980) and Hsiao and Shemdin (1980); a Bingham fluid by Migniot (1968), Krone (1965), Pazwash and Robertson (1971), Gularce (1978), Vallejo (1979, 1980) and Englund and Wan (1984). However, what is important in this case is to find a model that can reasonably simulate the two important parameters: bed shear stress and mud motion. These two parameters are directly related to wave erosion and wave attenuation. This is the first step in studying the wave erosion process.

Initially a 1-D numerical Bingham fluid model was developed by the author to simulate these two observed phenomena. However, the results demonstrated that it could not appropriately simulate wave-mud interactions. A linearized multi-layered model was then developed to predict the wave decay and the bed shear stress. In this model, the mud bed was arranged as layers of linear viscoelastic material to meet the depth variation of mud properties. The water layer was characterized by having a constant viscosity. Velocities, pressure, shear stress profiles and wave attenuation coefficient were the products.

Following the selection of a model for the soft mud, an effort was made to measure the mud properties by using the viscometer and other auxiliary equipment.



1. Pressure and shear stress at the water-mud interface contribute to the motion and erosion of the soft mud.
2. Momentum transfer from waves to muds alters the kinematics of water waves.
3. Turbulence structure of the water determines the suspended sediment distribution.
4. Bed shear stress and the mud resistance to erosion determine the rate of erosion.
5. Mud motion and associated energy dissipation plus the minor energy loss from the water viscosity cause the attenuation of water waves.
6. Eroded sediment mass serves as a sediment source in the sediment transport.
7. Wave-induced second order current contributes to the sediment transport process.
8. Successive oscillatory shear deformation in the mud bed alters the mechanical properties of the mud, and therefore, the dynamic response of the wave-mud system.

Legend: Box with dashed line represents the system, ovals show the processes, circles show the results.

Fig. 1-1. Schematic Depiction of Response of Wave-Mud System.

Because of the complexity of the erosion process itself, laboratory tests to observe wave erosion under clearly specified conditions were absolutely necessary. Alishahi and Krone (1964), Jackson (1973), and Thimakorn (1980) have all done some initial studies. However, their data were not complete enough to give an expression for the erosion rate function. Therefore, wave erosion tests were performed to provide information on the actual erosion and entrainment behavior. In the present study, quantities of sediment mass eroded were obtained and incorporated with the bed shear stress calculated from the 2-D mathematical model to develop an erosion rate function.

The diffusion process in the wave flow field was studied by observing the spreading of dye and the suspended sediment concentration profiles. A conclusion concerning the possible profile of the diffusion coefficient is proposed.

Marine sediment beds tend to change their physical properties under wave action. Alishahi and Krone (1964) reported a sudden loosening of the bed. Schuckman and Yamamoto (1982) reported the reduction of shear strength of a bentonite bed. Both observations point to the degradation and possible liquefaction of mud bed under wave loading. This may result in a change of flow structure and a change in the interfacial shear stress and energy dissipation as well. Therefore, this long-term bed property change was also monitored in the wave erosion tests.

In addition to the above, there are other complexities which need to be briefly addressed: the effects of salinity differences between

the eroding fluid and the pore water; the construction of a mattress-like layer by organic material; the effects of wave-induced current, etc. Although these were not here studied, they may be considered in future investigations.

1.3 Objectives and Scope of Study

The objectives of this study were as follows:

1. to develop a hydrodynamic model that can be used to simulate the two important parameters of wave-mud interaction: mud bed motion and bed shear stress,
2. to conduct laboratory experiments to obtain necessary data as input for the model,
3. to conduct laboratory experiments to verify model results,
4. to conduct laboratory experiments on the wave erosion and entrainment of soft mud beds, and
5. to propose an erosion rate function.

The scope of this study was defined as follows:

1. The hydrodynamic model developed was limited to the primary forcing mechanism only, i.e., linear waves; secondary effects were excluded.
2. Water and mud were considered immiscible layers in the model.
3. The equations of motion were linearized by neglecting the convective acceleration terms.
4. Verification of model results was limited to comparing measurements of wave attenuation, velocities, and pressures to calculated values.
5. Wave erosion tests were conducted in a wave flume to be described in Chapter 6. Mud bed thicknesses were limited to within 10 - 15 cm.

Waves were restricted to regular (monochromatic), progressive and non-breaking types.

6. The pore fluid and the eroding fluid were the same. This was achieved by equilibrating the sediment with the eroding fluid.
7. Vertical sediment concentration profiles were observed but no attempt was made to develop a theoretical approach for simulating the depth-distribution.
8. Three consolidation periods, 2 days, 1 week, and 2 weeks, for the mud beds were selected, and limited to self-weight consolidation.
9. Erosion rate studies were limited to two flocculated sediments and one fluid. Kaolinite and Cedar Key (Florida) mud were the two sediments. Tap water without added salt was the eroding fluid.

1.4 Outline of Presentation

This study is presented in the following order. A brief review of previous studies on wave erosion of soft muds is given in Chapter 2, followed by a discussion of problems in those studies, including those related to constitutive models for the soft mud, bed shear stress, and diffusion features in the wave flow. Chapter 3 describes an effort to develop a 1-D numerical Bingham fluid model to simulate the water-mud system and the conclusion that the 1-D model is not necessarily a good approach. Chapter 4 presents a 2-D hydrodynamic model which treats muds as a viscoelastic material. Bed shear stresses needed for correlation with the erosion data from Chapter 6 are also presented. Chapter 5 describes the experimental procedures used to obtain the viscoelastic constants for the mud beds used in the wave

erosion tests. Experiments to measure the erosion of kaolinite and Cedar Key mud are given in Chapter 6 and Chapter 7. Erosion rates are also presented. Summary and conclusions of the study are given in Chapter 8. The derivation of boundary conditions for the multi-layered hydrodynamic model is presented in Appendix A. In Appendix B the horizontal velocity and pressure predicted by the model are compared with measurements. Calibration of the current meter in an oscillatory flow, design of the light meter, and development of a numerical low-pass filter are given in Appendix C. In Appendix D, data from the wave erosion experiments are presented.

CHAPTER 2 STUDY BACKGROUND

2.1 Introduction

Previous studies on the wave erosion, constitutive models for mud and their behaviors, and wave diffusion coefficients will be reviewed. These subjects are important in the understanding of the wave-mud system and provide necessary information to simulate the dynamics of this system.

2.2 Wave Erosion/Resuspension

Water waves apply periodic shear stresses at the water-mud interface. Whenever the shear stress exceeds the bonding force (cohesive forces and self weight) between particles, erosion occurs. The eroded material is transported and dispersed into the water column and high turbidity is subsequently observed.

Investigations of wave erosion phenomena have been made primarily on cohesionless material, i.e., sand beds. Only a few experiments deal with cohesive sediment. In this section, erosion studies with cohesive sediment under non-breaking wave conditions are discussed.

Alishahi and Krone (1964) conducted the earliest wind wave erosion experiments for the San Francisco Bay mud. The test section, where the

mud was placed, was 1.2 m in length and located at the downstream side of the wave flume (18 m in length). The average thickness of the mud beds was about 1 cm. Water samples were taken at several locations via a special device that gave only depth-averaged sediment concentration. Total suspended sediment mass was then obtained by summation of the product of sediment concentration and water volume. Figure 2-1 shows one of their two test results. Their most significant result was "the demonstration of the existence of critical wave induced shear for suspension of the bed surface." No or negligible erosion occurred for a bed shear stress less than the critical shear. See the response in the first 4 hr in Fig. 2-1. Another interesting response reported was "a sudden loosening of the bed and direct movement of sediment into suspension." This phenomenon occurred in both runs and was responsible for a significant increase of suspended sediment. See the response after 4.5 hr in Fig. 2-1. However, possible reasons for this sudden loosening were not given. Their Run 1 showed that an equilibrium state had been reached during the erosion process. Unfortunately, Run 2 was not sufficiently long for an equilibrium condition to have been reached, as was noted by the investigators.

Anderson (1972) performed field experiments in The Great Bay estuarine system in New Hampshire. He took records of tide, wind speed, wind direction, wave height, and suspended sediment concentration. He found a linear relationship between suspended sediment concentration and water wave height at flood tide, while at ebb tide these two factors could not be correlated. He also concluded that wave force is most important for introducing sediment into the water column.

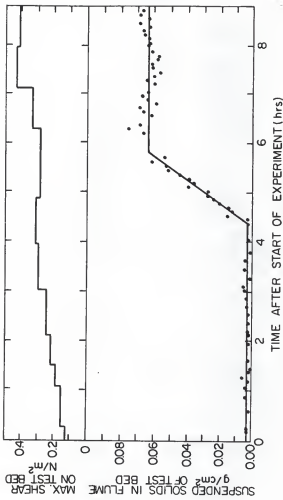
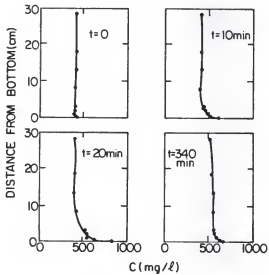


Fig. 2-1. A Plot of the Suspended Solids and Bed Shear Stress for a Wave Resuspension Test (After Aliahi and Krone, 1964).

Jackson (1973) conducted laboratory experiments to study the effects of water waves on the resuspension of muds on a beach. Breaking waves were involved because of the sloping beach. He found that waves produced little erosion or resuspension when the bottom orbital velocity was less than 10 - 12 cm/s. For orbital velocities greater than 20 cm/s, particle-by-particle erosion behavior shifted to mass erosion.

Thimakorn (1980) conducted non-breaking wave resuspension tests of mud taken from the Sakohon River mouth, an estuary in central Thailand. His wave flume had dimensions of 45 cm width, 60 cm depth, and 45 m length. The grain size distribution and clay composition were not given but the investigator noted that all sediments were washed through a U.S. standard sieve no. 200. The mud was rinsed with fresh water and the experiments were conducted in fresh water. Mud slurry was uniformly distributed in the entire flume, and was allowed to settle for two weeks. The final bed thickness was 2.5 cm. He took water samples at nine elevations at only one location. Figure 2-2 shows examples of the concentration profile. The data show a strong vertical mixing mechanism illustrated by the uniform concentration profile for the top 25 cm and gradient over the bottom 5 cm. He integrated these profiles and obtained the time variation of total suspended sediment concentration. From these data, he concluded that the wave erosion process did reach a steady state after 3 or 4 hours. However, the possibility of a strong sediment concentration gradient in the longitudinal direction was not considered. This gradient, for example, could be induced by the longitudinal variation of bed shear stress. Therefore, his statement regarding the steady state condition may not be fully



$$\begin{aligned}
 h &= 29.4 \text{ cm} \\
 H &= 5.4 \text{ cm} \\
 T &= 1.7 \text{ s} \\
 R_w &= 4900
 \end{aligned}$$

Fig. 2-2. Measured Suspended Sediment Concentration Profiles from a Wave Resuspension Test (after Thimakorn, 1980).

justified in case of a strong longitudinal gradient of sediment concentration.

Thimakorn (1984) also presented a mathematical model to simulate the suspended sediment concentration profile. This was composed of (1) a shear model for predicting the sediment mass eroded by wave shear stress (which had a similar function to that of the erosion rate) and (2) a diffusion model for distributing the eroded sediment into the water column. The diffusion model, based on a constant diffusivity, should have had the well-known log-linear distribution curve for the sediment concentration profile at steady state. However, Thimakorn did not demonstrate this characteristic but introduced a depth-varying diffusivity profile and asserted that the results were good compared to measured data.

Some relevant conclusions based on the aforementioned studies are as follows:

1. The critical shear stress concept for erosion by steady flow (Partheniades, 1965; Mehta *et al.*, 1982) can also be applied for wave erosion. In other words, wave-induced bed shear stress must exceed a critical value to cause noticeable erosion.
2. The mud beds used in these studies were quite thin. They were on the order of 1 to 2.5 cm. Therefore, the interaction between the mud bed and water waves was limited. Water wave attenuation was not mentioned in these studies, possibly because it was not noticeable for such a small mud thickness. However, this is not the case in the prototype, where significant wave decay has been reported

- (Tubman and Suhayda, 1976; Wells, 1983). Therefore, a thicker mud bed should be employed for wave erosion/resuspension tests.
3. Wave erosion rates were not mentioned even though this information is most important for estimation of sediment transport.
 4. Data on the vertical structure of suspended sediment profiles are rare. One practical reason is the huge amount of sediment samples that must be gathered for this purpose. An easy and reliable measurement technique for rapidly recording cohesive sediment concentration is not available yet. It is believed that light attenuation caused by individual sediment particles or flocs can be utilized for this purpose, e.g., the Iowa Sediment Concentration Measuring System for suspended sand (Glover *et al.*, 1969). However, unresolved problems still remain in measuring silt and clay suspensions.
 5. It remains unclear whether the wave erosion process reaches a steady state or not. Suppose a steady state can be reached, then it must reflect a downward increase of erosion resistance in the bed, provided no deposition is occurring. A similar behavior has been observed for steady flow erosion processes (Mehta *et al.*, 1982). However, more data are required to support the premise of a steady state for wave erosion.
 6. The sudden movement of bed material may be caused by the cyclic mobility or liquefaction of the bed by water waves. The former, for clays subjected to oscillatory shear loads, has been demonstrated by Schuckman and Yamamoto (1982) for bentonite beds. The latter, for silt or fine sand under cyclic loads, also has been

verified by Turcotte *et al.* (1984). Pamukcu *et al.* (1983) claimed that these two terminologies (cyclic mobility and liquefaction) actually describe the same phenomenon but for a different type of soil. The important results from this "loosening" are the changing flow structure (for both water and mud) as well as the erosion behavior.

7. In the previous studies noted, the bed layers were assumed to be rigid. Bed shear stresses were evaluated from linear wave theory and the wave friction factor concept. Such an assumption is valid for a hard soil or compacted sediment of low water content. In general, particularly for soft muds, motion within the bed can be significant, and the shear stress between the eroding fluid and the bed must be evaluated by considering the dynamics of mud motion. However, the question of which bed properties should be selected has not been resolved.

2.3 Constitutive Models for Soft Muds

Elastic, poro-elastic, viscous fluid, viscoplastic, and visco-elastic behavior are the five behavioral models which have been proposed for simulating mud properties. They are discussed in this section. It may be unrealistic to say that any simple model, such as those described below, is good enough to represent the rather complex behavior of mud. However, in general, the goal is not to obtain an absolutely correct answer but to find a relatively reasonable predictive model.

Before discussing any model, it may be helpful to examine the nature of a clayey soil under a dynamic shear load. Although the

characteristics of the clay bed discussed are for quite low water contents, it does give some insight into soft bed behavior.

2.3.1 Nature of Clayey Soil

Hardin and Drnevich (1972) measured clayey soil response under cyclic load. They followed the definition of energy loss ratio given by Kolsky (1963) as the ratio of the energy dissipation in taking a specimen through a stress cycle and the elastic energy stored in the specimen when the strain is a maximum. See Fig. 2-3. For a stress-strain cycle not too far from the linear range, the energy dissipation is small (see the small hysteresis loop). However, when the strain is far off the linear range, the stress-strain path follows the large hysteresis loop and results in high energy dissipation. Kovacs et al. (1971) indicated that the ratio of energy dissipation, λ , increases at large shear strains. See Fig. 2-4. This implies that, for a given shear load, soft muds have high energy dissipation rates due to the large shear strain. The more dense muds, however, have smaller strains and consequently small energy dissipation as well. This also implies that energy dissipation is velocity-dependent (strickly speaking, shear displacement-dependent) since high velocities usually mean large shear displacements.

Thiers and Seed (1968) demonstrated that the shear strength of clays can be reduced when subjected to a sufficient number of cyclic shear loads. See Fig. 2-5. This phenomenon was also observed by Schuckman and Yamamoto (1982) for marine sediment from measurement of the undrained shear strength, S_u , of a bentonite bed before and after

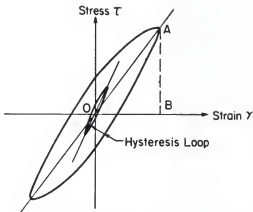


Fig. 2-3. Shear Stress-Strain Loop for Clay under Cyclic Loading.

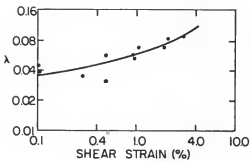


Fig. 2-4. Energy Dissipation Ratio λ versus Shear Strain (after Kovacs et al., 1971).

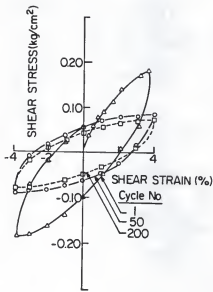


Fig. 2-5. Shear Stress-Strain Loops and Effects of Cyclic Loading (after Thiers and Seed, 1968).

wave loading. S_u (N/m^2) was empirically related to the shear modulus G (N/m^2) according to $G = \alpha S_u^m$, with $\alpha = 0.66$ and $m = 1.75$, applicable to G values on the order of 10^2 to 10^4 N/m^2 . A maximum reduction of S_u of about 55% was reported. The reduction was fully recovered 9 days after stopping the wave action. The reduction of shear modulus is typically due to dynamic softening experienced by the sediment when subjected to cyclic shear stresses.

2.3.2 Elastic Model

For an isotropic and homogeneous linear elastic body, the constitutive equation for an incompressible material can be represented by

$$T' = 2G E' \quad (2-1)$$

with

$$E_{ij}' = \frac{1}{2} \left(\frac{\partial \tau_i}{\partial x_j} + \frac{\partial \tau_j}{\partial x_i} \right) \quad (2-1a)$$

where T and E are the stress and strain tensor, respectively, the prime indicates the deviator parts of those two tensors, i, j , are free indices, and τ_i is the displacement in the x_i direction. Mallard and Dalrymple (1977) used this model to study the stress and displacement of a soil bed. Dawson (1978) also used this model but included the inertia term to improve upon Mallard and Dalrymple's results.

A serious drawback of this model is that no damping effects can be obtained because no viscous or friction terms are involved. Therefore, this model can not justifiably represent the interaction of the wave-mud system, where energy dissipation is important.

2.3.3 Poro-elastic Material with Coulomb Friction

Yamamoto and Takahashi (1985) suggested that the internal loss of energy is due to Coulomb friction and is independent of the velocity of soil movement. Because of the nature of the energy loss mechanism they chose, a direct measure of the energy dissipation of mud was selected. This direct measure does not require any assumption concerning the nature of internal friction. However, the results are dependent on the strain amplitude as well as the previous stress experience. This approach complicates the modeling of soil behavior because more parameters are involved.

Yamamoto (1982) incorporated the inviscid fluid flow assumption for the water waves (therefore, the momentum is transferred to the mud by normal pressure only). He then solved the equations of motion for a poro-elastic soil skeletal frame and Darcy's equation for the pore water pressure. Energy dissipation was evaluated by using a complex shear modulus, in which the imaginary part stands for the friction damping coefficient. Because of their inviscid fluid assumption for water, the bed shear stress (an important parameter for erosion) was ignored. The applicability of "poro-elastic material" to muds (which have low permeability and can be considered as a continuum) is not apparent.

2.3.4 Viscous Fluid Model

In this model the sediment bed is treated as a fluid which has a greater viscosity and higher density than water. The constitutive equation is

$$\mathbf{T}' = 2\mu \mathbf{D}' \quad (2-2)$$

with

$$D_{ij} = \frac{1}{2} \left(\frac{\partial u_i}{\partial x_j} + \frac{\partial u_j}{\partial x_i} \right) \quad (2-2a)$$

where D' is the deviator part of the rate of deformation tensor D which is close to E for small strains, and u_i is the velocity in the x_i direction.

Gade(1958) may have been the first to adopt this model to simulate energy dissipation in a two-layered system. He assumed the overlying water to be an inviscid fluid and the driving force to be restricted to long waves only. In addition to theoretical derivation, he also conducted experiments to verify his results. Unfortunately, his experiments did not provide any information on real mud behavior because he used a sugar solution instead of mud. Since a general model based on the same viscous fluid assumption was developed later by Dalrymple and Liu (1978), Gade's work is not further discussed.

Dalrymple and Liu (1978) published their "complete model," in which they used two layers of (laminar) viscous fluid to represent the overlying water and the soft mud bed. They then solved the linearized Navier-Stokes equations for wave propagation. The boundary conditions were specified as follows. First, the no-slip condition was satisfied at the rigid bottom. Second, at the mud-water interface the horizontal velocity, vertical velocity, shear stress, and normal stress were matched. Third, the zero shear stress and zero normal stress conditions were specified at the free surface. Finally, the linearized kinematic boundary condition at the free surface and the water-mud interface were invoked. This resulted in 10 equations and 10 unknowns. After some

manipulations, the 10 equations were reduced to a single one, and a numerical method was utilized to solve it. Velocities, pressure, and the interfacial wave amplitude were typical outputs. Although the shear stress profile was not shown it can be worked out easily from the velocity gradients.

Based on their model, Fig. 2-6 shows the horizontal velocity amplitude profiles for four mud viscosities, v_2 . All other parameters are the same: wave height, $H = 0.026$ m, period, $T = 1.75$ sec, water density, ρ_1 , and mud density, ρ_2 , equal to 1000 and 1260 kg/m^3 , respectively, and water viscosity $v_1 = 10^{-6} \text{ m}^2/\text{sec}$. The interfacial shear stress, τ_b , and the decay coefficient, k_{lm} , are also displayed. It is observed that because of the viscous fluid assumption, the interfacial shear stress turns out to be small. Figure 2-6 indicates that the horizontal velocity in the bottom layer is of the same order as that in the upper water layer provided the kinematic viscosity of mud is less than $0.01 \text{ m}^2/\text{sec}$ (1000 times higher than that for water). The difference in the velocity phase for these two layers is found to be about 45 degrees. This means that the velocity gradient at the water-mud interface is small, which explains why the interface shear stress was small.

Also notice in Fig. 2-6, that for small v_2 , e.g., less than $10^{-3} \text{ m}^2/\text{sec}$, the viscous wave boundary layer $\sqrt{v_2/2\sigma}$ is limited to the mud layer. For high mud viscosity, the wave boundary layer thickness extends up to the interface and a second wave boundary layer in the water layer is developed. This second wave boundary is characterized by the velocity overshoot above the interface. This overshooting is due

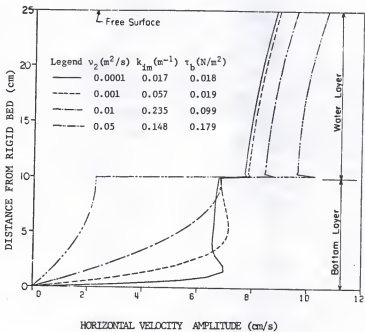


Fig. 2-6. A Plot of the Horizontal Velocity Amplitude Profiles by Using the Two-Layered Viscous Fluid Model.

to the influence of the viscosity within the second boundary layer. This phenomenon has been explained by Dean and Dalrymple (1984) and observed by Sleath (1970) for a smooth bed, and Jonsson and Carlsen (1976) for a rough bed.

The velocity in the lower layer is significantly reduced for high viscosity because the entire mud layer is inside the viscous wave boundary layer. However, the fact that measured viscosity data (see Chapter 5) indicate typically low viscosities, e.g., 10^{-3} to 10^{-4} m²/sec, for the soft mud prohibits the use of high viscosity in the model. However, model results from a high viscosity are closer to what has been observed (Migniot, 1968; Nagai *et al.*, 1982; Schuckman and Yamamoto, 1982). This hints at another velocity restraining mechanism, which can be incorporated, for instance, into the viscosity term to create a high apparent viscosity. This can then be used to simulate the mud motion. Either the Bingham model's yield strength or the viscoelastic model's elasticity could be used. These two models will be discussed next.

Despite the drawback in the selection of a viscous fluid model to simulate wave-mud interaction, Dalrymple and Liu's model is indeed the one with the most complete approach. Efforts to generalize their approach as well as to incorporate other restraining mechanisms have been made and are presented in Chapter 4.

2.3.5 Viscoplastic model

Viscoplastic material, also called a Bingham plastic, is characterized by a special feature recognized as the yield strength. Basically, a viscoplastic material can sustain a shear stress even when it

is at rest, but when the shear stress intensity reaches a critical value the material flows, with viscous stresses proportional to the excess stress intensity. The constitutive equation (Malvern, 1969) is

$$\tau = (\mu + \frac{K}{\sqrt{II_D}}) D' \quad (2-3)$$

with

$$II_D = \frac{1}{2} D_{ij} D'_{ij} \quad (2-3a)$$

where II_D is the second invariant of the deviator part of the rate of deformation tensor, K and μ are the yield strength and apparent viscosity. Notice that the extra term, i.e., the second invariant in the constitutive equation, results in a nonlinear equation of motion which is difficult to solve analytically except in a few simple steady-flow cases. Unfortunately, the wave propagation problem is not included. Although many researchers have studied the rheological properties of mud by using this model, none has been able to solve the equations of motion of a Bingham material under an oscillatory force.

Krone (1965) used a fairly extensive experimental procedure to measure the rheological properties, i.e., yield strength and apparent viscosity, of cohesive sediment. The maximum sediment concentration in his experiments was about 110 g/l. The period of consolidation was not mentioned. However, it can be inferred that he did not allow the sediment to settle down because he remolded the mud quite frequently to keep the sediment in suspension. He found that the yield strength for all the samples in his experiments was proportional to the 2.5th power of sediment concentration. See Fig. 2-7. The apparent viscosity for mud, μ_m , was 1 to 10 times higher than those for water, μ_w . See Fig. 2-8.

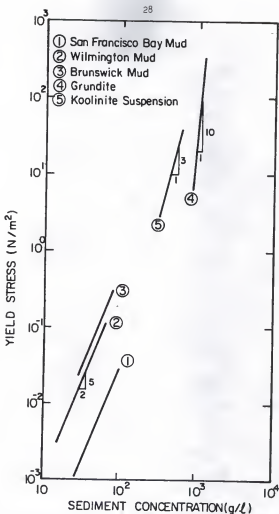


Fig. 2-7. Relationship between Yield Strength and Sediment Concentration (Data from Krone, 1965; Gularate, 1978; Engelund and Wan, 1983).

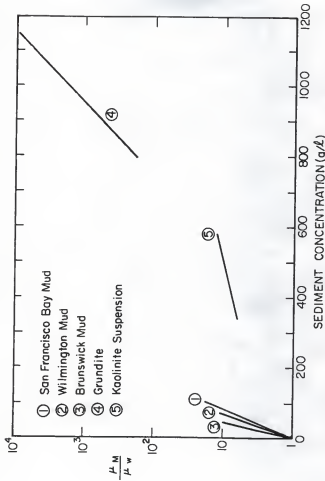


Fig. 2-8. Relationship between Apparent Viscosity and Sediment Concentration.
(Data from Krone, 1965; Gulari, 1978; Engelund and Wan, 1983).

Migniot (1968) also made a series of laboratory experiments to study the physical properties of cohesive sediments and their behavior under hydrodynamic forces. He observed that muds have an "initial rigidity" and that it is proportional to the 5th power of sediment concentration, ranging from 120 to 800 g/l. The initial rigidity was defined as the yield strength extrapolated from a curve (not a straight line) which fitted the measured data on shear stress versus rate of shear strain. The apparent viscosities were small for low sediment concentration but increased in significance when the sediment concentration became greater than 200 g/l. For example, $\mu_m = 20 \mu_w$ when the sediment concentration was around 200 g/l. However, $\mu_m = 150 \mu_w$ when the concentration went up to 500 g/l.

Gularte (1978) used a vane viscometer to measure the viscosity and yield strength of grundite, which is an equal mixture of illite and silt. The sediment concentration ranged from 600 g/l to 1000 g/l. He found that the Bingham yield strength was proportional to the 10th power of sediment concentration. See Fig. 2-7. The apparent viscosity, μ_m , was 1000 times higher than μ_w . See Fig. 2-8.

Englund and Wan (1984) studied the instability of the hyper-concentrated flow. They found that the Bingham model is quite satisfactory for the description of the instability of the fluid surface elevation. They found the yield strength to be proportional to the 3rd power of sediment volume concentration. The correlation between μ_m and sediment concentration is also shown in Fig. 2-8.

Parker and Kirby (1982) pointed out that, although mud suspensions have been characterized as Newtonian fluid at low solid concentration,

to Bingham plastic at high concentration, the true behavior should follow a pseudoplastic model, and that the yield strengths obtained by many researchers are really extrapolations (to zero shear strain rate) based on measurements at higher shear strain rates. They also presented data from Williams and James (1978) to support their view point.

To summarize the afore-described studies on the viscoplastic model, some conclusions may be stated as follows:

1. The yield strengths and apparent viscosities observed vary significantly. No unique, correlative relationships have so far been found.
2. Mud suspensions at high sediment concentration do not follow Newtonian fluid behavior. Although a Bingham model is commonly suggested, a pseudoplastic model may be more appropriate.
3. In previous studies, attention does not seem to have been paid to the effects of self-weight consolidation. This may be important, however, because muds possess a shear strength and a behavior which approaches that of an elastic solid. Field-measured acceleration data (in two horizontal and one vertical direction) of mud do not seem to show the quiescence-moving-quiescence behavior predicted by the Bingham fluid model (Tubman and Suhayda, 1976). Instead, a continuously varied acceleration, which implies an elastic behavior, is observed.
4. The Bingham model predicts no motion in the mud whenever the shear stress is less than the yield strength. Therefore, no energy loss can be predicted under this condition. However, unless the equation

of motion for a Bingham fluid can be solved, it would be difficult to say whether there is a movement or not.

5. To further examine the suitability of the Bingham model for the wave-mud system, solving the velocity field for both water and mud, even one-dimensionally, is important. The velocity and associated energy dissipation data can provide information for the justification of using this model. Efforts to evaluate the one-dimensional water-mud system have been made and the results are discussed in Chapter 3.

2.3.6 Viscoelastic Model

Muds can have elastic properties when the sediment concentration exceeds a specific value. Golden *et al.* (1982) reported that kaolinite suspensions can have a shear strength when the solid fraction exceeds 0.04 (sediment concentration over 107 g/l) and it increases markedly with higher sediment concentration. Mud beds usually have a sediment concentration greater than 200 g/l. Therefore, elasticity can not be neglected. Furthermore, in order to account for the energy loss due to mud motion, a dissipation function must be included. Therefore, viscoelastic models may be used.

Viscoelastic models account for the energy loss in an elastic solid in an indirect manner. It is assumed that the restoring forces are proportional to the amplitude of vibration, while the dissipative forces are proportional to the velocity.

Two simple linear models, namely those based on the Voigt and Maxwell elements, are available. These are based on the analogy of a

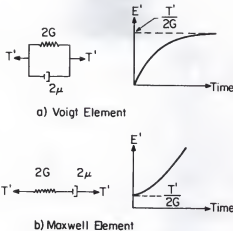


Fig. 2-9. System Diagram for Simple Viscoelastic Models and Response under Constant Loading.

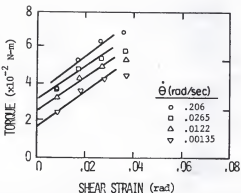


Fig. 2-10. Viscoelastic Behavior of Clay (after Stevenson, 1973). The rate of angular displacement is denoted by $\dot{\theta}$.

spring-dashpot system. They are plotted in Fig. 2-9 and the constitutive equations are presented as

$$\text{Voigt element: } T' = 2G E + 2\mu \dot{E}' \quad (2-4a)$$

$$\text{Maxwell element: } T' + \mu/G \dot{T}' = 2\mu \ddot{E}' \quad (2-4b)$$

where T and E are the stress and strain tensor, respectively, the prime indicates the deviator part of those two tensors, the dot indicates the derivative with respect to time, and G and μ are constants. Figure 2-9 shows the shear strain as function of time under a constant shear load. For the Voigt element, the response of elastic shear strain is delayed, but it finally reaches the value that the spring alone would reach. However, the Maxwell element will keep creeping because of the nature of the dashpot. The Maxwell element is often used to describe the relaxation of shear stresses under a constant strain. In the Voigt element, the spring and dashpot are subject to the same displacement but different stresses. It is easily shifted between a fluid and an elastic solid and the behavior is frequency-independent. The Maxwell element, however, behaves as an elastic solid at a high frequency load and as a fluid at a low frequency load.

Hsiao and Shemdin (1980) studied the wave decay problem by assuming that soft muds have Voigt properties. They solved the linearized two dimensional equation of motion for the Voigt element given by Kolsky (1963) and assumed the overlying water to be an inviscid fluid. Kolsky gave

$$\rho \frac{\partial^2 \zeta_1}{\partial t^2} = - \frac{\partial p}{\partial x_i} + G \frac{\partial^2 \zeta_1}{\partial x_j^2} + \mu \frac{\partial^2}{\partial x_j^2} \left(\frac{\partial \zeta_1}{\partial t} \right) \quad (2-5)$$

where ζ_i is the displacement in the x_i direction, t is the time, p is the pressure, and ρ is the material density. Hsiao and Shemdin (1980) gave results showing a rapid wave energy dissipation.

Macpherson (1980) also studied the wave attenuation problem by assuming that muds have the properties of a Voigt element. He had a different treatment of Eq. 2-5 and arrived at a linearized Navier-Stokes equation but with a complex viscosity. His apparent viscosity for the mud is given in Eq. 2-6a. Here he represented the shear modulus as the imaginary part of the apparent viscosity term and kept the kinematic viscosity as the real part. Although his model could not predict a bed shear stress because he neglected the viscosity of the water layer, his approach greatly simplified Eq. 2-5.

$$\text{Voigt element: } v_e = v + j \frac{G}{\mu \sigma} \quad (2-6a)$$

$$\text{Maxwell element: } v_e = \frac{v}{1 + (\mu \sigma / G)^2} \left(1 + j \frac{\mu \sigma}{G} \right) \quad (2-6b)$$

Following Macpherson's approach for an oscillatory load, the apparent viscosity for a Maxwell element is also given in Eq. 2-6b. However, unlike the Voigt element, the apparent viscosity is frequency-dependent. For an infinite G , the Maxwell element behaves as a viscous fluid but the Voigt element becomes a rigid body. For zero μ , the Voigt element is a perfect elastic material while the Maxwell element is not defined. Also the Maxwell element is not defined for zero G ; however, the Voigt element is a viscous fluid at this condition.

Questions concerning which element simulates mud behavior more closely are not discussed by Macpherson (1980) or by Hsiao and Shemdin (1980) and still remain unclear. Stevenson's (1973) data, see Fig. 2-10, showed that the Voigt element was applicable for his soil samples. However, his samples had a high shear strength and were not like a soft mud. Therefore, experiments to observe the response of mud under constant shear loads were conducted in the present study. The objective was to find whether the Voigt model or the Maxwell model was better in modeling the stress-strain relation, and also to find the material constants G and μ . Details are given in Chapter 5.

2.4 Bed Shear Stress

The bed shear stress is well known as the most important factor in the erosion process in steady flow as well as in an oscillatory wave flow. Unlike steady flow, for a smooth bed (ratio of the bed roughness r to the semi-excursion distance just outside the boundary layer a_b , $r/a_b < 0.01$), the wave bed shear stress has a period which is basically equal to the wave period. For a rough bed, $r/a_b > 0.01$, higher order harmonics may be induced by the rhythmic formation and release of vortices (Lofquist, 1980). Most papers dealing with bed shear stress in the oscillatory flow assume that the bed is rigid and that the water is free of sediment. This is a reasonable assumption for a sandy bed or a clayey bed with low water content since there is no appreciable motion in the bed. However, for a cohesive sediment bed with high water content, this assumption is not always applicable because the bed may also move (Tubman and Suhayda, 1976; Nagai *et al.*, 1982). This would

mean that the bed shear stress would be different because the velocity gradient is altered at the interface. Therefore, to accurately estimate the bed shear stress one must consider the dynamic response of mud as well. In this section, only the wave bed shear stress for a rigid bed is briefly summarized.

Jonsson (1966) proposed the following equation to evaluate the maximum bed shear stress (which is one of the most popular equations still used):

$$\tau_b = \frac{1}{2} \rho f_w u_b^2 \quad (2-7)$$

where $u_b = a_b \sigma$ is the maximum particle velocity just outside the bottom wave boundary layer which can be predicted by classical wave theory, and f_w is the wave friction factor. This is a simple form and the only unknown is f_w .

The wave friction factor is a function of the surface roughness and wave Reynolds number R_w , defined by Jonsson (1966):

$$R_w = u_b^2 / v\sigma \quad (2-8)$$

Here v is the kinematic viscosity of the water. For the case when $R_w < 1.25 \times 10^4$, the viscous wave boundary condition, Jonsson (1966) gave

$$f_w = 2 / \sqrt{R_w} \quad (2-9)$$

At higher wave Reynolds numbers, the bottom roughness is involved. This is the transition zone between viscous and full turbulent flow. Kamphuis (1975) presented a chart (Fig. 2-11) to evaluate f_w . For

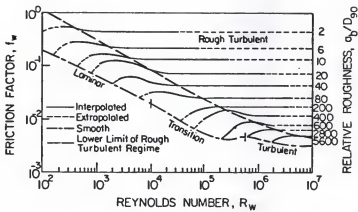


Fig. 2-11. Wave Friction Factor (after Kamphuis, 1975). The grain size, which is larger than 90% of the total mass of soil sample, is denoted as D_{90} .

higher R_w , only the roughness is important. Jonsson (1966, 1975, 1980) also gave a formula to evaluate the wave friction factor under this condition.

2.5 Wave Diffusion Coefficient

Fisher (1968) pointed out that the concept of the apparent diffusion coefficient D_m (turbulent diffusion and dispersion) has been widely employed to predict the transport of pollutants. This concept has been used for sediment transport as well. However, the problem of evaluation of the diffusion coefficient for a non-breaking wave environment has not been fully clarified yet. Previous studies relative to this coefficient, although having no consistent results, are briefly summarized here.

Kennedy and Locher (1972) gave a good summary of the early studies. Key points are given here. The pioneering experimental work done by Shinohara *et al.* (1958) showed that a constant diffusivity is good for sand with a mean diameter of 0.2 mm. However, specifying only one constant diffusivity for pulverized coal with a mean diameter of 0.3 mm was not sufficient. This was because of the discontinuity in the concentration profile near the bed. Hattori (1969) also employed the constant diffusion concept and showed good agreement with his experiments for the top 80% of the water column.

Das (1971) concluded, from his oscillating bed experiment, that the diffusion coefficient varies linearly with distance above the bed.

Hom-ma and Horikawa (1963) gave Eq. 2-10 for the diffusion coefficient under a wave field.

$$D_m = \frac{1}{2B} \frac{Hc}{\sinh kh} \frac{\sinh^3 kz''}{\cosh^2 kz''} \quad - (2-10)$$

where B is a constant related to the ripple geometry, H is wave height, h is water depth, k is wave number, z'' is elevation above bed, and c is wave celerity. This formula uses the velocity profile from the small amplitude wave theory and, therefore, the diffusion coefficient increases slowly upward since the velocity profile does not vary sharply with elevation. However, their sediment concentration data (for the upper 70% of water layer) showed quite good linearity on a log-linear plot which implies a constant D_m .

Horikawa and Watanabe (1970) measured the turbulent velocity fluctuations, u' and w' , rather than deduce the variation of diffusion coefficient from the vertical distribution of the mean sediment concentration. They concluded that the root mean square (RMS) value of w' is almost independent of z , whereas the RMS value of u' , which is greatest near the bed, decreases first just above the bed, and then becomes nearly constant for the most part.

Jonsson and Carlsen (1976) measured wave velocity profiles and then calculated the profile of eddy viscosity, ϵ . Their flow had a high R_w and a rough bed. Their results showed that the maximum ϵ is located within the turbulent wave boundary layer. Outside the boundary layer, ϵ decreases drastically and approaches zero for the upper water column. Here $\epsilon = 0$ reflects the fact that turbulence is not important in the calculation of velocity for wave flows. However, turbulence is indeed important in sediment transport. For cohesive sediment, momentum transfer coefficients are almost the same as mass transfer coefficient,

diffusion coefficient, (Jobson and Sayre, 1970). Therefore, it can be inferred that the turbulent diffusion coefficient should be also the largest near a rough bed.

Wells *et al.* (1978) presented Eq. 2-11 as "the most justifiable estimate for suspended-sediment concentration" along the Louisiana coast as a result of wave resuspension:

$$C(z) = 5.31 \exp(-1.8 z'') \quad (2-11)$$

where C is the sediment concentration in kg/m^3 and applies to a water depth $h < 5 \text{ m}$. Their result implies a constant diffusion coefficient since there is a log-linear relationship between C and the vertical coordinate, z'' .

Hwang and Wang (1982) summarized the models available for the turbulent diffusion coefficient outside the wave boundary and suggested that a modified version of their model, Eq. 2-12, would be the most plausible one:

$$D_m = a H^2 c \frac{\sinh^2 kz''}{2 \sinh^2 kh} \quad (2-12)$$

where a is a constant.

Thimakorn (1984) also gave an equation for the diffusion coefficient profile, which was close to that given by Hwang and Wang (1982), based on the concept of turbulent energy.

The above information is summarized in Table 2-1. The wave Reynolds number, R_w , which indicates the flow regime near the mud surface, is also included. Notice that some of the laboratory studies

have had a wide range of R_w which indicates that both the viscous and turbulent wave boundary layers were included. Two types of diffusion coefficient profiles have been introduced. Data from Shinohara *et al.* (1958), Hattori (1969), Horikawa and Watanabe (1970), and Wells *et al.* (1978) suggest a constant coefficient for the top 80% of the water layer, the remainder apparently having another constant value. However, to the contrary, the others (Hom-ma and Horikawa, 1963; Das, 1971; Hwang and Wang, 1982; Thimakorn, 1984) suggest a minimum diffusivity at the bottom and increasing upward.

Table 2-1. Diffusion Coefficients in Wave Flow

Researcher	Sediment	R_w	Suggested D_m
Shinohara <i>et al.</i>	Sand, Coal	< 6700	Constant
Hattori	Sand	< 24000	Constant
Hom-ma & Horikawa	Sand	< 26400	Eq. 2-10
Horikawa & Watanabe	-	> 12000	Constant
Wells <i>et al.</i>	Mud	> 12000	Constant
Hwang & Wang	Sand	-	Eq. 2-12
Thimakorn	Mud	< 10000	similar to Eq. 2-12

It is interesting to note that none of these studies has mentioned a possible longitudinal dispersion phenomenon. In actual shear flow, fluid layers near the bottom tend to exhibit a sharp velocity gradient. This results in a much greater longitudinal dispersion. Taylor (1954)

gave the example of steady uniform pipe flow and showed that the dispersion coefficient can be about 200 times larger than the mean value of the turbulent diffusion coefficient. However, Awaya (1969) pointed out that in an oscillatory flow the dispersion coefficient can not be that high, because of the limited time-scale associated with this type of flow, tidal flow in his case. It can still be inferred, however, for wave-induced flow, that there must be a strong longitudinal mixing layer above the bed surface because of sharp velocity gradients in the bottom boundary layer. It is further noted that the bed surface is the main source of turbulence (Nielsen, 1984). This may explain what was observed by Shinohara et al. and others mentioned. To further understand the wave diffusion behavior, dye diffusion tests were conducted in the present study. Suspended sediment concentration profiles were also collected. Details are discussed in Chapter 6 and Chapter 7.

CHAPTER 3 ONE-DIMENSIONAL BINGHAM FLUID MODEL

3.1 Introduction

In this chapter a numerical solution of the velocity field and energy dissipation in a vertical one-dimensional water-mud system is presented. The mud is assumed to have Bingham plastic properties with constant density but variable viscosity and yield strength. The overlying water is assumed to have constant density and viscosity. The objectives are to examine the velocity profile and the associated energy dissipation in this system, and to justify this 1-D model for simulating the water-mud system.

3.2 Problem Formulation

Figure 3-1 shows the system diagram. A variable grid system, with grid size Δz_j , was chosen to give better resolution at the bottom, the interface, and the free surface. The grid number starts from 1 at the rigid bottom, and ends at the free surface with number J. The total depth is h. The fluid properties, e.g., density ρ , kinematic viscosity v , and yield strength K, as well as the horizontal velocity u , are specified at the center of each grid element. Shear stresses, τ , are specified at the node points. The one-dimensional linearized equation of motion is

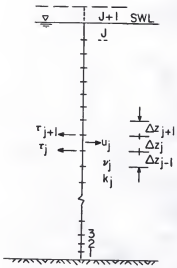


Fig. 3-1. System Diagram for the 1-D Numerical Bingham Fluid Model.

$$\frac{du}{dt} = -g \frac{dn}{dx} + \frac{1}{\rho} \frac{d\tau}{dz} \quad (3-1)$$

with

$$\tau = (\mu + \frac{K}{|du/dz|}) \frac{du}{dz} \quad (3-1a)$$

where dn/dx is the slope of the water surface profile, t is time, g is gravity, and z is the vertical direction. The boundary conditions are as follows:

1. no-slip at the rigid bottom, $u=0$ at $z=0$.
2. velocity is maximum at the free surface, $du/dz=0$ at $z=h$, or,

$$u_J = u_{J+1}$$

3. The initial condition says that the fluid is at rest at the beginning, $u=0$ at $t=0$.

To ensure that the flow velocity is maximum at the free surface, a fictitious layer (from J to $J+1$) is added at the top of the water column. Equation 3-1, with the boundary conditions, can be solved by the double sweep method (Abbott, 1980). The finite difference formulation is

$$\frac{u_J^{n+1} - u_J^n}{\Delta t} = -g \left(\frac{dn}{dx} \right)^{n+1/2} + \frac{1}{2\rho_j} \left(\frac{\tau_{J+1}^{n+1} - \tau_J^{n+1}}{\Delta z_j} \right) + \frac{1}{2\rho_j} \left(\frac{\tau_{J+1}^n - \tau_J^n}{\Delta z_j} \right) \quad (3-2)$$

where

$$\tau_{J+1}^{n+1} = [u_{J+1} + \frac{k_{J+1}(\Delta z_j + \Delta z_{J+1})}{2 |u_{J+1}^n - u_J^n|}] \frac{2(u_{J+1}^{n+1} - u_J^{n+1})}{(\Delta z_j + \Delta z_{J+1})} \quad (3-2a)$$

$$\tau_J^{n+1} = [u_J + \frac{k_j(\Delta z_j + \Delta z_{j-1})}{2 |u_J^n - u_{j-1}^n|}] \frac{2(u_J^{n+1} - u_{j-1}^{n+1})}{(\Delta z_j + \Delta z_{j-1})} \quad (3-2b)$$

Notice that the velocities at time n are also used to evaluate the velocity gradient in the denominator for the shear stress term at time $n+1$. The superscript $n+1/2$ implies the center of each time step. Equation 3-2 can be rearranged in terms of u^{n+1} and rewritten as

$$A u_{j+1}^{n+1} + B u_j^{n+1} + C u_{j-1}^{n+1} = D \quad (3-3)$$

where

$$A = -\left(u_{j+1} + \frac{K_{j+1}(\Delta z_j + \Delta z_{j+1})}{2 |u_{j+1}^n - u_j^n|}\right) \frac{\rho_j (\Delta z_j + \Delta z_{j+1}) \Delta z_j}{\rho_j (\Delta z_j + \Delta z_{j+1}) \Delta z_j} \quad (3-3a)$$

$$\begin{aligned} B = & 1 + \left(u_{j+1} + \frac{K_{j+1}(\Delta z_j + \Delta z_{j+1})}{2 |u_{j+1}^n - u_j^n|}\right) \frac{\rho_j (\Delta z_j + \Delta z_{j+1}) \Delta z_j}{\rho_j (\Delta z_j + \Delta z_{j+1}) \Delta z_j} \\ & + \left(u_j + \frac{K_j(\Delta z_j + \Delta z_{j-1})}{2 |u_j^n - u_{j-1}^n|}\right) \frac{\rho_j (\Delta z_j + \Delta z_{j-1}) \Delta z_j}{\rho_j (\Delta z_j + \Delta z_{j-1}) \Delta z_j} \end{aligned} \quad (3-3b)$$

$$C = -\left(u_j + \frac{K_j(\Delta z_j + \Delta z_{j-1})}{2 |u_j^n - u_{j-1}^n|}\right) \frac{\rho_j (\Delta z_j + \Delta z_{j-1}) \Delta z_j}{\rho_j (\Delta z_j + \Delta z_{j-1}) \Delta z_j} \quad (3-3c)$$

$$\begin{aligned} D = & -g \Delta t \left(\frac{dn}{dx}\right)^{n+1/2} + \\ & \left(u_{j+1} + \frac{K_{j+1}(\Delta z_j + \Delta z_{j+1})}{2 |u_{j+1}^n - u_j^n|}\right) \frac{\rho_j (\Delta z_j + \Delta z_{j+1}) \Delta z_j}{\rho_j (\Delta z_j + \Delta z_{j+1}) \Delta z_j} u_{j+1}^n \\ & + [1 - \left(u_{j+1} + \frac{K_{j+1}(\Delta z_j + \Delta z_{j+1})}{2 |u_{j+1}^n - u_j^n|}\right) \frac{\rho_j (\Delta z_j + \Delta z_{j+1}) \Delta z_j}{\rho_j (\Delta z_j + \Delta z_{j+1}) \Delta z_j} \\ & - \left(u_j + \frac{K_j(\Delta z_j + \Delta z_{j-1})}{2 |u_j^n - u_{j-1}^n|}\right) \frac{\rho_j (\Delta z_j + \Delta z_{j-1}) \Delta z_j}{\rho_j (\Delta z_j + \Delta z_{j-1}) \Delta z_j}] u_j^n \end{aligned}$$

$$+ \left(u_j + \frac{K_j(\Delta z_j + \Delta z_{j-1})}{2 |u_j^n - u_{j-1}^n|} \right) \frac{\Delta t}{p_j(\Delta z_j + \Delta z_{j-1}) \Delta z_j} u_{j-1}^n \quad (3-3d)$$

Now introduce the auxiliary equation, Eq. 3-4, and substitute into Eq. 3-3 to obtain Eq. 3-5

$$u_{j+1}^{n+1} = E_j u_j^{n+1} + F_j \quad (3-4)$$

$$\begin{aligned} u_j^{n+1} &= \frac{-C}{A E_j + B} u_{j-1}^{n+1} + \frac{(D - A F_j)}{(A E_j + B)} \\ &= E_{j-1} u_{j-1}^{n+1} + F_{j-1} \end{aligned} \quad (3-5)$$

Comparing Eq. 3-4 and Eq. 3-5 reveals that E_j and F_j , from $j=J-1$ to 1, can be obtained because $E_{j=1}$ and $F_j=0$ are specified by the zero velocity gradient condition. Therefore, the first sweep yields all the E_j and F_j . The second sweep, from Eq. 3-4 and the no-slip boundary condition, $u_1=0$, solves for the velocity for all the grid elements.

Because there is a velocity gradient term in the denominator (Eq. 3-1a) for evaluating the shear stress of the Bingham fluid, a problem of calculating A , B , C , and D was encountered because of the zero velocity gradient at the onset. However, letting the first sweep stop at the uppermost element, S , where the yield strength is zero, and moving the no-slip condition to the element one cell below element S , allows calculation of the velocity profile above this element. By comparing the shear stress acting at the bottom of the moving fluid and the yield strength one layer below, a decision can be made as to whether the next layer will move or not and therefore to stop the first sweep

for the next time step. If this is done, the first sweep can go down step-by-step to a cell where the shear stress and shear strength are equal, or to the rigid bottom provided the driving force is large enough.

Wave energy components are evaluated separately as kinetic energy and potential energy. The time-averaged total energy per unit surface area is

$$\begin{aligned} E_n &= \frac{1}{T} \int_0^T \int_0^h \rho g dz dt + \frac{1}{2T} \int_0^T \int_0^h \rho u_j^2 dz dt \\ &= \alpha a^2 \\ &= \alpha a_0^2 \exp(-2k_{im}x) \end{aligned} \quad (3-6)$$

where α is a constant coefficient, k_{im} is the wave decay coefficient, and a_0 is the wave amplitude at $x = 0$. The time-averaged energy dissipation per unit surface area is calculated as follows:

$$\begin{aligned} E_d &= \frac{1}{T} \int_0^T \int_0^h \tau \frac{du}{dz} dz dt \\ &= \frac{1}{T} \sum_{n=1}^N \left[\sum_{j=1}^J (\tau_{j+1}^n u_{j+1/2}^n - \tau_j^n u_{j-1/2}^n) \right] \Delta t \end{aligned} \quad (3-7)$$

where τ and u are given by the model and N is the total number of time steps for a complete wave cycle. The energy dissipation can also be written as

$$\begin{aligned} E_d &= c_g \frac{\partial E}{\partial x} = 2 c_g \alpha k_{im} a_0^2 \exp(2k_{im}x) \\ &= 2 c_g k_{im} E_n \end{aligned} \quad (3-8)$$

where c_g is the wave group velocity and can be replaced by \sqrt{gh} because of the long wave assumption. Therefore, the decay coefficient can be obtained as

$$k_{im} = E_d / (2\sqrt{gh} E_n) \quad (3-9)$$

3.3 Results

The numerical scheme was tested for the steady-state solutions first, simply because analytical solutions are available. The water surface gradient was arbitrarily selected to be 10^{-5} . The time increment was also arbitrarily chosen as 50 seconds since the implicit scheme is unconditionally stable. Figure 3-2a shows the velocity profile for a two-layered viscous fluid at selected times. Squares show the analytical solution. Figure 3-2b shows the velocity profile for an assumed fluid which has exponentially distributed yield stress and viscosity. The results are satisfactory in both cases.

The pressure forcing term (dn/dx) in Eq. 3-1 was then changed to a cosine function to simulate a periodic wave load. The time increment was also reduced to 0.05 second because the wave period was relatively short and also to minimize possible error introduced by the step-by-step downward computational procedure. The scheme was compared with the results from Dalrymple and Liu's two-layered viscous fluid model and showed reasonable agreement. See Fig. 3-3. The observed discrepancy was due to the long wave assumption in the numerical model. In this example, the long wave assumption could not account for the viscosity variation at the interface. This may be interpreted as follows. Long waves are characterized by a constant dynamic pressure in the entire water depth (i.e., pressure is hydrostatic) and by the absence of

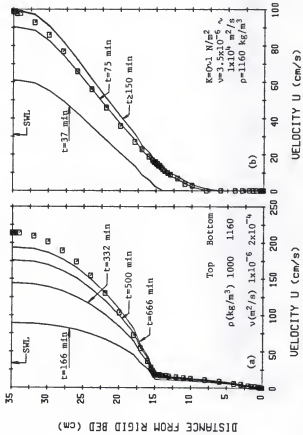


Fig. 3-2. Horizontal Velocity Profiles for Two Steady Flows. (a) Two-Layered Viscous Fluid; (b) Bingham Fluid with Exponentially Increasing K and η .

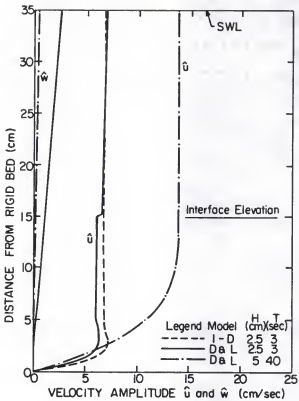


Fig. 3-3. Comparison of Wave Velocity Amplitude Profiles from 1-D Model and Dalrymple and Liu's Model with $\rho_1=1000$ kg/m³, $\rho_2=1160$ kg/m³, $v_1=1 \times 10^{-6}$ and $v_2=2 \times 10^{-4}$ m²/s.

vertical velocity. For cases where the viscosity of the bottom layer is not too large, the viscous boundary layer, of thickness δ_L , is far below the interface. Then the equation of motion, for the part outside δ_L , can be simplified by neglecting the shear stress term, the last term in Eq. 3-1. Although the shear stress in the bottom layer is larger than in water, because $v_2 \gg v_1$, it is still small when compared with the pressure and inertia terms. Therefore, a single equation can be used from the water surface down to a particular elevation which is below the interface but above the viscous boundary layer. This phenomenon was demonstrated by another run of Dalrymple and Liu's model (see Fig. 3-3) but with a long wave period, $T = 40$ sec.

A simulation of water-Bingham fluid system was then performed. Input data were specified as follows. The water layer had a constant density (1000 kg/m^3) and viscosity ($1 \times 10^{-6} \text{ m}^2/\text{sec}$). The bottom Bingham layer also had a constant density, 1160 kg/m^3 , viscosity, $0.0002 \text{ m}^2/\text{sec}$, and yield strength, 0.1 N/m^2 . Fig. 3-4a,b shows the velocity profiles under two wave conditions.

It was expected that the low layer would not move for a small wave height (Fig. 3-4a). This is because the bed shear stress for this wave was less than the yield strength. For larger waves, the lower layer is observed to move with a zero velocity gradient in much of the lower layer, indicating a plastic sliding. Nevertheless, the results show that the velocities in the mud bed were either zero or close to that in the water layer.

Energy dissipation and total energy at each time step were evaluated. Time-averaged values over one wave period were calculated next.

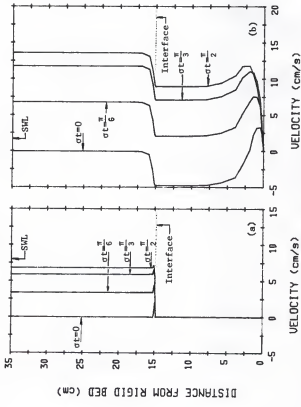


Fig. 3-4. Wave Velocity Profiles for the Water-Bingham Fluid System with $T = 3$ sec.
 (a) $H = 2.5$ cm and $k_{im} = 0.0011 \text{ m}^{-1}$; (b) $H = 5$ cm and $k_{im} = 0.016 \text{ m}^{-1}$.

The decay coefficient was then obtained based on Eq. 3-9 and is given in Fig. 3-4.

Yield strength and dynamic viscosity data were obtained from viscometer measurement (see Chapter 5 for detail) for a kaolinite bed with a two-day consolidation period, which was the softest mud bed in the wave erosion tests (described later in Chapter 6 and Chapter 7). Results are given in Fig. 3-5. The yield strength and dynamic viscosity varied from 2.5 to 4.4 N/m² and 0.1 to 0.2 N-s/m², respectively. The corresponding kinematic viscosity was on the order of 1×10^{-4} m²/s. Because of the relatively high yield strength, the model-simulated mud bed showed no motion at all. See Fig. 3-6. The energy dissipation was significantly low because there was no motion in the bottom layer.

3.4 Conclusion

It must be realized that muds can dissipate energy only if they are moving. The 1-D numerical model presented here shows no motion in the mud layer, therefore no energy dissipation, when the yield shear strength is higher than the bed shear stress. However, such a condition of no motion - no dissipation was not observed in experiments described later, and thus indicated that the 1-D Bingham model is not generally applicable for the simulation of water-mud interaction in erosion studies.

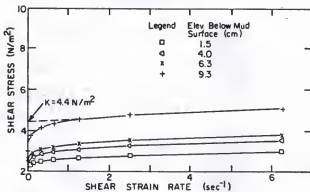


Fig. 3-5. Shear Stress versus Shear Strain Rate for Kaolinite Bed with Two-Day Consolidation Period.

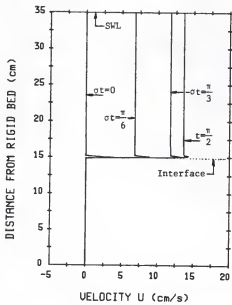


Fig. 3-6. Wave Velocity Profiles for Water-Bingham Fluid System with Measured Yield Strength and Viscosity.

CHAPTER 4
TWO-DIMENSIONAL MULTI-LAYERED HYDRODYNAMIC MODEL

4.1 Introduction

A multi-layered hydrodynamic model to simulate the two important parameters, wave damping coefficient and interfacial shear stress, is presented in this chapter. The water layer was assumed to be characterized by a constant kinematic and eddy viscosity. A simple linear viscoelastic behavior, the Voigt element, and the linearized equations of motion were selected for modeling mud response under wave loading. This selection was based on the discussion presented in Chapter 2, Chapter 3 and the results from Chapter 5.

Depth variation of mud properties can be simulated by further dividing the mud bed into layers. The equations of motion for the water layer are also linearized to simplify the problem. The water and mud layers are considered incompressible and immiscible such that density, viscosity, and shear modulus are constant in each layer.

4.2 Formulation

Figure 4-1 is a definition sketch of the water-mud system. Water waves propagate in the x -direction. The water layer has a thickness, d_1 , and the underlying mud bed can be considered as composed of several layers of linear viscoelastic material with thicknesses d_i . The free

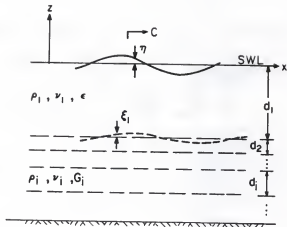


Fig. 4-1. Schematic Figure for the Multi-Layered Model.

surface displacement is η . Here $i = 2, 3, \dots, n$. The displacement at each interface is ξ_i . The displacements η and ξ_i can be expressed as

$$\eta = a_0 \exp[j(kx - \omega t)] \quad (4-1a)$$

$$\xi_i = b_{0i} \exp[j(kx - \omega t)] \quad (4-1b)$$

where a_0 is the given water wave amplitude at $x = 0$, b_{0i} are unknown complex variables for interface wave amplitudes and phases at $x = 0$, $j = \sqrt{-1}$, $c = 2\pi/T$, T is the wave period, t is time, and k is a complex wave number. The real part, $k_r = 2\pi/L$, is related to the wave length, L . The imaginary part, k_{im} , represents the decay coefficient defined as

$$a(x) = a_0 \exp(-k_{im}x) \quad (4-2)$$

This expression correctly represents the wave decay in a flume (Schuckman and Yamamoto, 1982; Nagai et al., 1982).

The linearized equations of motion for the incompressible upper fluid and incompressible, viscoelastic Voigt element layers under oscillatory load are

$$\frac{\partial u_1}{\partial t} = -\frac{1}{\rho_1} \frac{\partial p_1}{\partial x} + v_{ei} \left(\frac{\partial^2 u_1}{\partial x^2} + \frac{\partial^2 u_1}{\partial z^2} \right) \quad (4-3a)$$

$$\frac{\partial w_1}{\partial t} = -\frac{1}{\rho_1} \frac{\partial p_1}{\partial z} + v_{ei} \left(\frac{\partial^2 w_1}{\partial x^2} + \frac{\partial^2 w_1}{\partial z^2} \right) \quad (4-3b)$$

where u and w are velocities in x and z direction, respectively. The apparent viscosity, v_{ei} , actually contains two terms. For the water layer, it contains the kinematic viscosity, v_1 , and a constant eddy viscosity, ϵ . The purpose of involving ϵ in the model is for the bed shear stress calculation. The approach presented later demonstrates that this choice of ϵ is not connected with the turbulent diffusion coefficient, D_m . Each mud layer is characterized by a kinematic viscosity, v_1 , and a shear modulus, G_1 , as discussed in Chapter 2. The

subscript $i=1, 2, \dots, N$ indicate the top, second, and subsequent layers, respectively, p_t^i is the total pressure defined as

$$p_t^i = p_i - \rho_i g z - p_i^0$$

and

$$p_i^0 = \begin{cases} 0, & \text{if } i = 1 \\ \sum_{m=1}^{i-1} ((\rho_m - \rho_{m-1}) g [\sum_{r=1}^{m-1} d_r]), & \text{if } i > 1 \end{cases} \quad (4-4)$$

where m and r are dummy indices. The continuity equation is

$$\frac{\partial u_i}{\partial x} + \frac{\partial w_i}{\partial z} = 0 \quad (4-5)$$

The solutions of these variables are assumed separable according to

$$\begin{aligned} u_i(x, z, t) &= \hat{u}_i(z) \exp(j(kx - \omega t)) \\ w_i(x, z, t) &= \hat{w}_i(z) \exp(j(kx - \omega t)) \\ p_i(x, z, t) &= \hat{p}_i(z) \exp(j(kx - \omega t)) \end{aligned} \quad (4-6)$$

Substituting u_i , w_i into the continuity equation one obtains

$$\hat{u}'_i = \frac{j}{k} \hat{w}'_i \quad (4-7)$$

where the prime indicates differentiation with respect to z . Introducing this equation for \hat{u}'_i into the horizontal momentum equation (4-3a) yields an expression for \hat{p}'_i , i.e.,

$$\hat{p}'_i = \left(\frac{\mu_{ei}}{k^2} \right) \left(\hat{w}''_i - \hat{w}'_i \lambda_i^2 \right) \quad (4-8)$$

with

$$\lambda_i^2 = k^2 - j \sigma v_{ei}^{-1}$$

Substituting \hat{p}'_i into Eq. 4-3b yields

$$\hat{w}_1''' = (k^2 + \lambda_1^2) \hat{w}_1'' + k^2 \lambda_1^2 \hat{w}_1 = 0 \quad (4-9)$$

The solutions for the water layer and the subsequent mud layers are in the form:

$$\hat{w}_1(z) = A_1 \sinh Z_1 + B_1 \cosh Z_1 + C_1 \exp(\lambda_1 z) + D_1 \exp(-\lambda_1(z+d_1)) \quad (4-10a)$$

$$\hat{w}_1(z) = A_1 \sinh Z_1 + B_1 \cosh Z_1 + C_1 \sinh N_1 + D_1 \cosh N_1 \quad (4-10b)$$

with $i=2,3,\dots,N$, $Z_i = k(d_1 + d_2 + \dots + d_{i-1} + z)$, and $N_i = \lambda_i(d_1 + d_2 + \dots + d_{i-1} + z)$. For only one mud layer, there are eight unknown complex coefficients (A_1, \dots, D_2) for the vertical velocities and the two unknown complex variables, i.e., wave number, k , and interfacial wave amplitude b_{01} . Therefore, 10 boundary conditions are required for solving for the 10 unknown coefficients. The 10 boundary conditions will be summarized here to show how the coefficient matrix is constructed. Details are shown in Appendix A.

At the free surface there is no external driving force, i.e., normal stress, $\sigma_n = -p + 2\mu_e \frac{\partial w}{\partial z}$, and shear stress, $\tau = \mu_e (\frac{\partial u}{\partial z} + \frac{\partial w}{\partial x})$, are zero. Because the actual free surface is unknown a priori, these two boundary conditions are applied at the mean or still water surface. Taylor expansion technique is applied as shown in Appendix A to obtain an approximate solution. Only the basic harmonic term is considered. All high harmonic terms are neglected. The zero normal stress condition at the free surface gives

$$M_1(A_1 \cosh kd_1 + B_1 \sinh kd_1) - 2v_{e1} \lambda_1 C_1 = p_1 g a_0 \quad (4-11)$$

The linearized kinematic free surface boundary condition yields

$$A_1 \sinh kd_1 + B_1 \cosh kd_1 + C_1 = -j \omega_0 \quad (4-12)$$

Equations 4-11 and 4-12 are combined to give Eq. 4-13

$$c_{1,1} A_1 + c_{1,2} B_1 + c_{1,3} C_1 = 0 \quad (4-13)$$

The coefficients $c_{i,j}$ are given in Appendix A. The zero shear stress condition at the mean free surface gives

$$c_{2,1} A_1 + c_{2,2} B_1 + c_{2,3} C_1 = 0 \quad (4-14)$$

At the water-mud interface E_1 (a priori unknown elevation), the horizontal and vertical velocities for the water and mud layer are matched. See Eq. 4-15 and 4-16. The linearized kinematic boundary condition at the interface gives Eq. 4-17. The matched normal stresses and shear stresses conditions between the water layer and the mud layer give Eqs. 4-18 and 4-19. For details, see Appendix A.

$$c_{3,1} A_1 + c_{3,4} D_1 + c_{3,5} A_2 + c_{3,6} B_2 + c_{3,7} C_2 + c_{3,8} D_2 = 0 \quad (4-15)$$

$$c_{4,2} B_1 + c_{4,4} D_1 + c_{4,5} A_2 + c_{4,6} B_2 + c_{4,7} C_2 + c_{4,8} D_2 = 0 \quad (4-16)$$

$$c_{5,2} B_1 + c_{5,4} D_1 + c_{5,9} b_{10} = 0 \quad (4-17)$$

$$\begin{aligned} c_{6,1} A_1 + c_{6,4} D_1 + c_{6,5} A_2 + c_{6,6} B_2 + c_{6,7} C_2 + \\ c_{6,8} D_2 + c_{6,9} b_{10} = 0 \end{aligned} \quad (4-18)$$

$$c_{7,2} B_1 + c_{7,4} D_1 + c_{7,5} A_2 + c_{7,6} B_2 + c_{7,7} C_2 + c_{7,8} D_2 = 0 \quad (4-19)$$

At the rigid bottom ($z=-d_1-d_2$), the no-slip condition ($u=w=0$) must be satisfied, i.e.,

$$c_{8,5} A_2 + c_{8,7} C_2 = 0 \quad (4-20)$$

$$c_{9,6} B_2 + c_{9,8} D_2 = 0 \quad (4-21)$$

These nine equations, Eq. 4-13 through Eq. 4-21, can be written as

a homogeneous matrix equation $c X = 0$, where c is a 9 by 9 matrix with non-zero terms specified from Eqs. 4-13 through 4-21. Here X is a column matrix which contains coefficients $A_1, B_1, C_1, D_1, A_2, B_2, C_2, D_2$, and b_{01} . The unknown complex wave number k is involved in the coefficient matrix c . This is an Eigenvalue problem since the system has solutions only for special k values such that the matrix c is singular, i.e., the determinant of matrix c is zero.

Adding one more mud layer in the bottom gives five more unknowns: four coefficients (A_3, B_3, C_3, D_3) in the added vertical velocity equation, and one (b_{02}) for the unknown new interfacial amplitude and phase. Five more boundary conditions must also be specified similar to Eq. 4-15 through 4-19. The newly added layer should be specified as the lowest one, directly above the rigid bottom. Then, the added equations can be listed as

$$c_{8,5}A_2 + c_{8,7}C_2 + c_{8,10}A_3 + c_{8,11}B_3 + c_{8,12}C_3 + c_{8,14}D_3 = 0 \quad (4-22)$$

$$c_{9,6}B_2 + c_{9,8}D_2 + c_{9,10}A_3 + c_{9,11}B_3 + c_{9,12}C_3 + c_{9,13}D_3 = 0 \quad (4-23)$$

$$c_{10,6}B_2 + c_{10,8}D_2 + c_{10,14}b_{20} = 0 \quad (4-24)$$

$$c_{11,5}A_2 + c_{11,7}C_2 + c_{11,10}A_3 + c_{11,11}B_3 + c_{11,12}C_3 + c_{11,13}D_3 + c_{11,14}b_{20} = 0 \quad (4-25)$$

$$c_{12,6}B_2 + c_{12,8}D_2 + c_{12,10}A_3 + c_{12,11}B_3 + c_{12,12}C_3 + c_{12,13}D_3 = 0 \quad (4-26)$$

The no-slip condition, now at $z=-d_1-d_2-d_3$, is replaced by

$$c_{13,10}A_3 + c_{13,12}C_3 = 0 \quad (4-27)$$

$$c_{14,11}B_3 + c_{14,13}D_3 = 0 \quad (4-28)$$

The size of the new coefficient matrix is then expanded to 14 by 14, and five more coefficients ($A_3 - D_3$, and b_{02}) are appended to the column matrix X . The homogeneous matrix equation, however, remains in a similar form, and the same technique may be utilized to solve it. When adding one more layer, matching conditions at the new interface and the no-slip condition at the rigid bottom are similar to Eqs. 4-22 through 4-28 because of the same equation for \hat{w} . However, the subscripts are increased by 5. The matrix c expands to 19 by 19. Figure 4-2 shows the layout of matrix equation, $c X = 0$, for N layers. The calculation of matrix c may be performed in an iterative manner (a DO-loop in the computer program). This approach allows greater flexibility to add layers in meeting the depth variation of mud properties. Any number of mud layers may be assigned provided this is necessary. Basically, the fewer the layers, the faster the rate of convergence.

4.3 Solution Technique

To find the complex wave number k for a zero determinant, the Newton-Raphson method was used. The principle of this method for a complex function is the same as that for a real function. The first guess of k value used is the wave number obtained from Airy's (linear) wave theory for a water depth d_1 . The second guess is arbitrarily set to be 1% off from the first one. These two values of k are real numbers, but then k shifts to a complex number because the coefficient matrix is a complex function. Examining the trajectory of the complex wave number and the value of the determinant suggests that the function

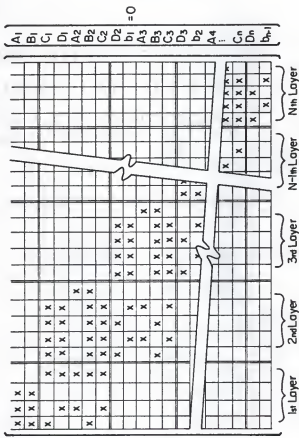


Fig. 4-2. Layout of the Coefficient Matrix for the Multi-layered Model.

has a tornado-like shape. To hit the target (exact k value for zero determinant), high precision in the computer program is required. Sometimes, an absolute zero determinant is difficult to obtain due to the large matrix and limited accuracy of the computer. Therefore, another convergence criterion was desirable. Comparing the results, e.g., velocity and pressure, obtained from a finite determinant value but with $\Delta k < 10^{-14}$ and that from a zero determinant showed no accountable difference. Therefore, $\Delta k < 10^{-14}$ was selected as the new convergence criterion. This criterion requires a reasonable number of iterations, i.e., less than 20, to obtain the results.

The elements of the column matrix X , after solving the matrix equation, do not represent the true answer but are proportional to the true value. Equation 4-11 (or Eq. 4-12) is invoked to obtain the proportionality constant and then to obtain the true A_1, B_1, \dots , and $b_{l=1}$. Pressure and velocity profiles are then determined easily from Eqs. 4-7, 4-8, and 4-10. Shear stress profile is obtained as

$$\begin{aligned}\tau &= \mu_e \left(\frac{\partial u}{\partial z} + \frac{\partial w}{\partial x} \right) \\ &= \frac{j}{k} \mu_e (\hat{w}^m + k^2 \hat{w}) \exp[j(kx - \sigma t)]\end{aligned}\quad (4-29)$$

4.4 Input data

The model was run through all the experimental cases (see Chapter 6 for detail). Wave amplitude, period, and the thickness, bulk density, viscosity, and shear modulus for each layer are the input data needed. The number of layers and thicknesses d_i were selected to meet the variation of measured density profile. For the water layer, the

density was selected to be 1000 kg/m³. The kinematic viscosity, v_1 , was 1×10^{-6} m²/sec. The eddy viscosity, ϵ , is dependent on the wave Reynolds number and is discussed later. Details for measuring G_1 and v_1 for the selected muds are given in Chapter 5. In this study, G and μ for the six experimental runs were correlated with the dry density. The correlative equations are presented in Chapter 5. See Table 5-2. Bed density information follows in Chapter 7, see Eq. 7-1 through 7-3. Wave conditions for the six experimental runs are presented in Chapter 6 (Table 6-4). The thickness of each layer for the six experimental runs are listed in Table 4-1. Each run had two wave loadings except Run 6 which had three. See Chapter 6 for detail.

An assumption concerning the eddy viscosity was that ϵ (water layer) is only a function of the water-wave parameters and is independent of mud bed rigidity. In other words, the eddy viscosity in the water column for a rigid bed was assumed to be the same as for a soft movable bed, given the same wave conditions. This assumption allows the determination and use of eddy viscosity in the model. Details are described next.

Given a high shear modulus for the mud layer, e.g., $G > 10000$ N/m², the model may be used to simulate the wave bed shear stress for a rigid bed. By comparing the model-predicted bed shear stress and that calculated from Jonsson's friction factor concept (using the friction factor diagram presented by Kamphuis, 1975: see Fig. 2-11 in Chapter 2), a value of the apparent eddy viscosity, $v_{e1} = v_1 + \epsilon$, can be estimated. From this, ϵ can be obtained given v_1 . Figure 4-3 shows an example with $d_1 = 3$ m, $a_0 = 0.25$ m, $\sigma = 0.79$ rad/sec, $\rho_1 = 1035$ kg/m³,

Table 4-1. Input Thickness for Each Layer (cm)

Run	d_1	d_2	d_3	d_4	d_5
1-1	21.65	2.5	2.5	4.0	5.0
	2	24.15	1.5	3.0	3.0
2-1	19.15	1.5	3.0	3.0	4.0
	2	19.65	1.0	3.0	3.0
3-1	16.15	2.5	3.0	4.0	5.0
	2	18.15	1.5	2.0	4.0
4-1	26.35	1.3	2.0	3.0	3.0
	2	28.65	1.0	1.0	2.0
5-1	19.65	2.0	3.0	5.0	6.0
	2	21.05	1.6	2.0	5.0
6-1	24.65	1.0	2.0	3.0	5.0
	2	25.15	0.5	2.0	3.0
3	25.15	0.5	2.0	3.0	5.0

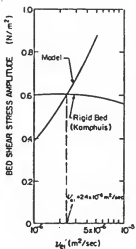


Fig. 4-3. Comparison of Computed Bed Shear Stress (Model and Kamphuis) at the Mud Surface to Determine the Eddy Viscosity of Water.

$v_1 = 1 \times 10^{-6} \text{ m}^2/\text{s}$, bed surface roughness $r = 20 \mu\text{m}$ and $R_w = 3.0 \times 10^5$. Values of d_2 , ρ_2 , and μ_2 were immaterial because of the high G_2 value. With a f_w from Kamphuis' diagram, Eq. 2-7 gives a maximum bed shear stress of 0.6 N/m^2 which is equivalent to the model having a total viscosity of $2.4 \times 10^{-6} \text{ m}^2/\text{sec}$. Therefore, the corresponding eddy viscosity would be $1.4 \times 10^{-6} \text{ m}^2/\text{sec}$ and may be used to calculate the interfacial shear stress for a soft movable bed under the same wave load. This procedure illustrates a practical method for estimating the water-mud interfacial shear stress for any wave flow condition. For the six experimental runs, however, the value of ϵ was set to be equal to zero because all $R_w < 10^4$ (presented later in Table 4-2). This is because $R_w < 10^4$ indicates a viscous sub-layer just above the mud surface and consequently zero eddy viscosity for the purpose of calculating the bed shear stress.

In oscillatory flows, the pressure force is balanced mainly by the inertia force. The shear force plays little role when outside the bottom boundary layer, δ , even though turbulence is involved. This can be understood by noting that a high value of Reynolds number, $R = ud_1/v_{e1} = 300 - 2000$, implies that the shear stress term can be neglected outside the boundary layer. This explains why the potential flow approach works quite well for water wave problems. For wave flows involving viscosity, an example of the horizontal velocity profile given by Dean and Dalrymple (1984, p. 264) indicates that the only influence of increased v_{e1} is an increase in δ . The velocity profile above δ does not change at all. Therefore, the value of ϵ for the water layer is primarily necessary for the determination of the bed shear stress.

4.5 Model Results

Model results in terms of velocities, pressure, and shear stress as well as the corresponding phase angles for the six experimental runs are summarized as follows. Details are presented in Appendix B. Five layers were chosen in all runs.

4.5.1 Velocity

Two types of vertical water velocity profiles are obtained by model simulation. In the first example (see Fig. 4-4a), the vertical velocity decreased to a minimum a few centimeters above the mud surface and then increased to a maximum at the mud surface. The vertical velocity profile in the mud started from maximum at the mud surface and decreased to zero at the rigid bottom. This profile tends to show that there is a "false bottom" above the mud surface. The tendency to have a false bottom is due to the vertical motion of mud being about 90 degrees out of phase with the surface wave. Mallard and Dalrymple (1977) have shown mathematically that a false bottom can exist for a perfectly elastic bed which has a vertical motion 180 degrees out of phase with the surface wave. In the present example the viscosity damps out the response and therefore only shows a tendency. In the second type (see Fig. 4-5a for Run 5-1) the vertical velocity does not have a phase lag between the water and mud layers.

Horizontal velocities were reduced significantly in the mud layers and also shifted 90 to 120 degrees. This implies that the velocity

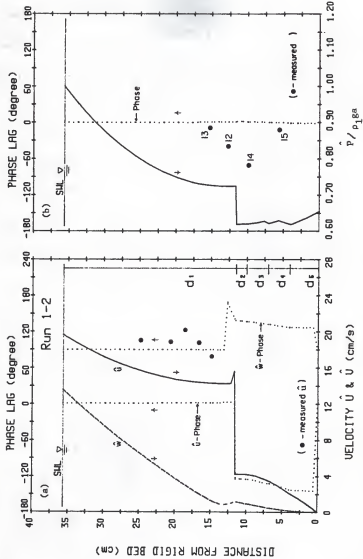


Fig. 4-4. Comparison of the Model Prediction and Measurement for Run 1-2. (a) Velocity; (b) Pressure.

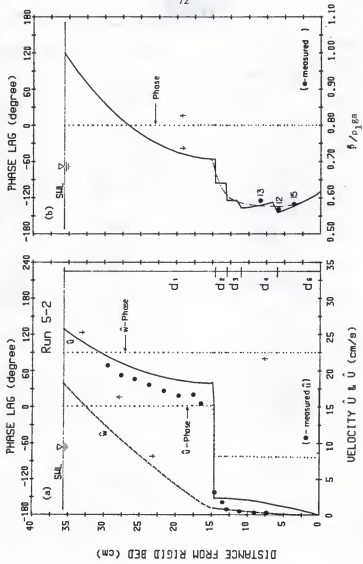


Fig. 4-5. Comparison of the Model Prediction and Measurement for Run 5-2. (a) Velocity; (b) Pressure.

gradient at the water-mud interface is larger than what meets the eye in Figs. 4-4a and 4-5a. Notice that the boundary layer thickness for the mud layers, $\sqrt{v_{ef}/2a} = 10$ cm, was greater than the thickness of each layer and resulted in the build-up of a horizontal velocity overshoot above the water-mud interface. The measured horizontal velocities (see Chapter 7 for details) in the water layer are also displayed. Measured values in these two examples show a reasonable agreement with model-simulated values.

Although the model gave information on the motion in the mud layers, experimentally measuring the motion was difficult. Here the horizontal mud displacements were measured by visual observation from the side wall for experimental runs 5 and 6. The amplitudes of movement of sediment particles near the side wall were converted to the corresponding velocity amplitudes (by using the formula $u = ac$) and compared with model results. The observed mud velocities, however, were reduced, due to the side boundary effects; therefore, they were smaller than predicted (by a factor of about 1:3.7, see Appendix B). In justifying the measurements, a relationship for the lateral distribution of the horizontal velocity, $u(y)$, where y is the lateral coordinate, must be worked out. Efforts to interpret the results by considering the side wall influence are given in Appendix B. The resulting value of the ratio of u in the center of the flume and u near the side wall ranged from about 4 to 7, which is not far from the average value of 3.7 obtained by a direct comparison of prediction and measurement.

4.5.2 Pressure

The pressure is always in phase both in the water and mud layers since it is the driving force. This phase relationship was also verified from experiments, see Section 7.2.2 in Chapter 7. The amplitude decreased in the water column, dropped at each interface between the layers, and increased within the mud layers. Figures 4-4b and 4-5b show two examples. Note that the measured pressure amplitudes (see Chapter 6 for details) were normalized by $\rho_1 g a$. At each interface, the normal stresses were matched from the two adjoining layers. Therefore, the pressure, $-p = \sigma_{nn} - 2\mu \partial w / \partial z$ dropped between layers because of a step-increase in μ and almost the same $\partial w / \partial z$. Within a mud layer, the shear stress term becomes important because of the high v_e value. The behavior in a vertical pressure profile can be depicted easily by substituting Eq. 4-6 and 4-7 into the vertical momentum equation (Eq. 4-3b). The vertical pressure gradient can be obtained as shown in Eq. 4-30. For low viscosity, e.g., water with $v = 1 \times 10^{-6} \text{ m}^2/\text{s}$, the first term of the right hand side dominates, and therefore yields a positive pressure gradient. For large v_e the second term is also important and may result in a negative pressure gradient as shown in Figs. 4-4b and 4-5b.

$$\frac{\hat{\partial p}}{\hat{\partial z}} = \rho [(j\sigma - k^2 v_e) \hat{w} + v_e \hat{w''}] \quad (4-30)$$

As already noted, the model uses layers of mud which have constant properties to simulate continuously varying properties. Therefore, the true pressure profile may be estimated by a smooth curve, e.g., the broken line in Fig. 4-5b.

Run 5 shows a reasonable agreement; however, Run 3 indicated that the measured pressure was larger (about 30%) than predicted. For other data, see Appendix B. Generally, the measured dynamic pressure was higher than that predicted by the model for kaolinite beds. The same was true for the Cedar Key mud bed, but only during the initial period of the wave loading. One possible reason is that the pressure transducer measured the total dynamic pressure, which also included the effect of time-varying mud structure and generation of pore water pressure. The model, however, does not account for these effects. After the completion of these processes, the measured dynamic pressure principally reflected the wave-induced pressure.

4.5.3 Shear Stress

The shear stress amplitude profile in this system showed a linear increase with depth characteristic of the mud bed over a rigid bottom, and negligible shear stresses in the water column except near the water-mud interface. See Fig. 4-6 for an example. The small total mud thickness, less than half of the wave length, is the likely reason for a linearly increasing shear stress profile. For an infinite mud thickness, the shear stress would eventually reach a maximum and then decrease (Mallard and Dalrymple, 1977). Shear stresses in the water layer are negligibly small because of the small velocity gradient except near the water-mud interface. Notice the nearly 90 degree shift of shear stress in the mud layers. This implies that the maximum shear stress occurred between the wave crest and trough. It may further indicate that the shear stress in the mud was induced mainly by the

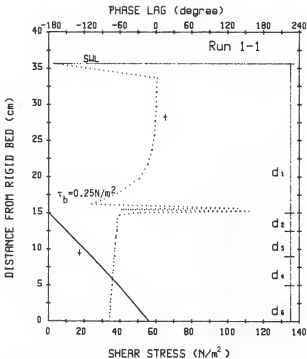


Fig. 4-6. An Example of the Model-Predicted Shear Stress Amplitude Profile.

longitudinal pressure variation at the mud surface rather than the water-mud interfacial shear stress. The maximum longitudinal pressure gradient occurs near the mean water elevation (90 degrees after wave crest), while the interfacial shear stress, being proportional to the velocity, is minimum. The figure shows oscillations of the shear stress just above mud surface. This would not be expected in reality and may be due to the calculation of phase lag by using small shear stress resulting in a numerical oscillation. Finally, it should be noted that the large shear stresses in the mud layer are due to the large viscosity, μ_e , and finite shear strain.

The model-predicted bed shear stress amplitude at $x = 0$, τ_{bo} , is

$$\tau_{bo} = \mu_e k \left(\hat{w}_1'' + k^2 \hat{w}_1 \right) \quad (4-31)$$

The values of τ_{bo} for the six runs are summarized in Table 4-2. Bed shear stress amplitudes based on the rigid mud bed assumption and Eq. 2-7 are also listed in the parentheses for comparison. It is observed that the model predicted generally larger τ_{bo} (up to 30%) than those from a rigid bed. This is because of the opposite (100 - 120 degree phase lag) motion between the mud and the water. However, for a very soft mud, e.g., Run 5, the model predicted a smaller value. It should also be noted that the longitudinal shear stress profile also exhibits an exponential decay law for $R_w < 10^4$. The bed shear stress amplitude at any location can therefore be evaluated as $\tau_b(x) = \tau_{bo} \exp(-k_{im}x)$. The spatially-averaged bed shear stress amplitude is

$$\langle \tau_b \rangle = \frac{1}{L} \int_0^L \tau_b(x) dx = \frac{\tau_{bo}}{k_{im} L} [1 - \exp(-k_{im} L)] \quad (4-32)$$

where $L = 8$ m is the length of mud bed section and k_{im} is the measured wave decay coefficient (see Chapter 6 for details). The corresponding R_w are also included in Table 4-2.

4.5.4 Water Wave Decay

A comparison of predicted and measured wave decay coefficient, k_{im} , is an easy way to check the validity of the model. A viscous damping mechanism implies that the greater the mud velocity, the higher the rate of energy dissipation. Therefore, a highly consolidated (rigid) bed can not be expected to have a high energy dissipation. Both the predicted and measured k_{im} show this behavior. See Fig. 4-7 and also Table 6-5, Chapter 6. Except for Run 6-1, the predicted and measured wave decay coefficient show satisfactory agreement.

Table 4-2. Interfacial Shear Stresses and Mud Wave Amplitudes

Run	τ_{bo} N/m ²	$\langle \tau_b \rangle$ N/m ²	R_w	b_{o1} cm
1-1	0.247 (0.187)	0.170	3600	0.24
2	0.386 (0.304)	0.242	4040	0.23
2-1	0.166 (0.163)	0.146	2360	0.05
2	0.291 (0.290)	0.245	3070	0.09
3-1	0.210 (0.178)	0.124	2830	0.23
2	0.293 (0.258)	0.158	2720	0.27
4-1	0.196 (0.192)	0.178	2510	0.06
2	0.297 (0.294)	0.251	2660	0.05
5-1	0.272 (0.274)	0.191	5130	0.14
2	0.421 (0.425)	0.314	6220	0.15
6-1	0.226 (0.200)	0.149	3450	0.07
2	0.352 (0.306)	0.248	3590	0.13
3	0.431 (0.376)	0.323	3810	0.21

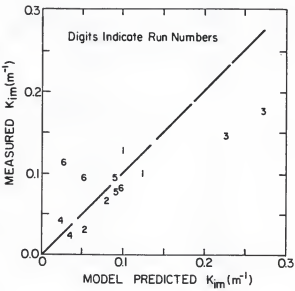


Fig. 4-7. Comparison of the Measured and Predicted Wave Decay Coefficient.

4.5.5 Interfacial Mud Wave Amplitude

The model-predicted water-mud interfacial wave amplitudes are also presented in Table 4-2. In experiments, the bed movement was difficult to visualize through the side wall (plexiglass) in Run 1 and Run 2 during the first 3 hr, but later, even with side boundary effects, the movement was observed. For other runs, the bed movement was observed at the beginning of the tests. Comparison with the measured interfacial wave amplitude for Runs 5-1 and 5-2 (0.4 and 0.45 cm, respectively) indicate that the predictions are low. This might be the case for the following reasons. (1) The model used a constant value of G and μ for each layer, but the actual values of G and μ probably varied significantly near the mud surface. This difference would cause a higher error in the computation. (2) The increase of mud bed mobility caused by continued shear deformation is difficult to characterize. This phenomenon was significant, especially near the bed surface. (3) Errors in observation were caused by the somewhat ill-defined mud bed surface.

4.6 Resonance Characteristics

The viscoelastic properties of the mud bed can cause the wave-mud system to become resonant when subjected to an oscillatory wave loading. This is because of the elastic characteristics of the spring in the Voigt model. The resonance phenomenon was noticed in the model while examining the effects of shear moduli and viscosities on the interfacial wave amplitude. When resonance occurs, the mud layer shows

a large mud wave amplitude, high velocities, and large attenuation of water waves. Hereafter the discussion is limited only to two layers, one for the water and the other for the mud. Further studies on the resonant response of depth-varied mud properties, i.e., variables s , G and μ , must await more effort.

The equation of motion for the mud layer (Eq. 4-3) can be nondimensionalized to obtain a complex Reynolds number, R (complex because the shear modulus is involved in the imaginary part of viscosity).

$$R^{-1} = \frac{v_2}{a_0 \omega d_2} + j \frac{G/\rho_2 \sigma}{a_0 \omega d_2} = R_r^{-1} + R_{im}^{-1} \quad (4-33)$$

Note that the velocity term in R has been replaced by $a_0 \omega$, wave amplitude times the wave frequency, because it is a simple and unique quantity in this system.

Figure 4-8 shows the relationship between R and the ratio of the mud wave amplitude, b_0 , and the water wave amplitude, a_0 . The selected input data are as follows: $a_0 = 0.03$ m, $\sigma = 5.236$ rad/sec, $d_1 = 0.2$ m, $d_2 = 0.15$ m, $v_1 = 1.0 \times 10^{-6}$ m²/sec, $\rho_1 = 1000$ kg/m³ and $\rho_2 = 1160$ kg/m³. In this example, when $R_{im} < 0.1$ or $R_r < 0.0023$, the mud bed has a high shear strength and behaves like a rigid bed. The system is overdamped when $R_r < 0.023$ ($\nu > 1$ m²/sec). For higher R_r , resonance occurs as indicated by the peak between $4 < R_{im} < 30$. For $R_{im} > 30$ ($G < 5$ N/m²), the mud behaves as a viscous fluid.

A similar example of this type of resonance behavior is a disc with moment of inertia I hung on an elastic shaft, with a damping

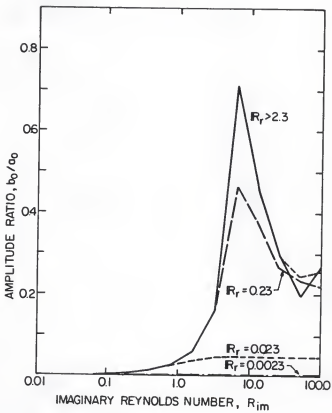


Fig. 4-8. Non-Dimensional Interfacial Wave Amplitude versus Complex Reynolds Number.

coefficient c_d , and subjected to an oscillatory torque. The resonance of this disc-shaft model has been discussed by Wylie (1966). For the water-mud system, however, the driving forces are not an external oscillatory torque but periodic pressure, which is non-uniformly distributed at the mud surface, and interfacial shear stress. The resulting periodic internal shear stresses then cause the oscillatory motion of mud bed.

To further understand the resonance behavior, two two-layered systems, with only the mud thickness and viscosity different, were excited by different wave periods. The selected input data are $a_0 = 0.018$ m, $d_1 = 0.22$ m, $\rho_1 = 1000$ kg/m³, $\rho_2 = 1265$ kg/m³ and $G = 73.5$ N/m². Figures 4-9a,b clearly demonstrate resonance at low viscosity. In this sample, the mud showed resonance when the excited wave had a period of 0.78 sec and 2.5 sec, respectively. It is noticed that the thicker the mud bed, the longer the wave period needed to result in resonance.

Another test of the frequency response with input data identical to Fig. 4-9b, but with G increasing to 245 N/m², has been displayed in Fig. 4-10a. The mud showed resonance with a 0.9 sec. excited wave. These diagrams indicate that the resonance frequency for the water-mud system is dependent on the value of shear modulus and the mud layer thickness.

Assuming the mud layer to be merely a viscous fluid will not show this type of resonance since no spring is in the system. Figure 4-10b clearly demonstrates this point by showing the response of a two-layered viscous fluid model.

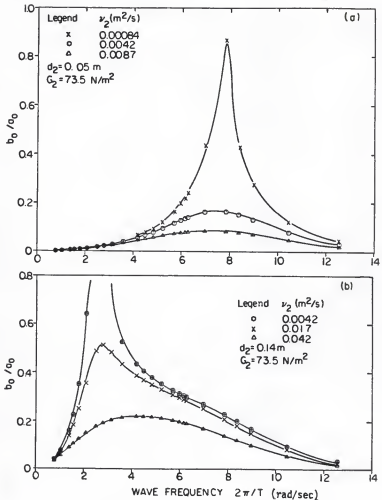


Fig. 4-9. Resonance Phenomenon of Water-Mud System.
 (a) with $d_2 = 0.05 \text{ m}$; (b) with $d_2 = 0.14 \text{ m}$.

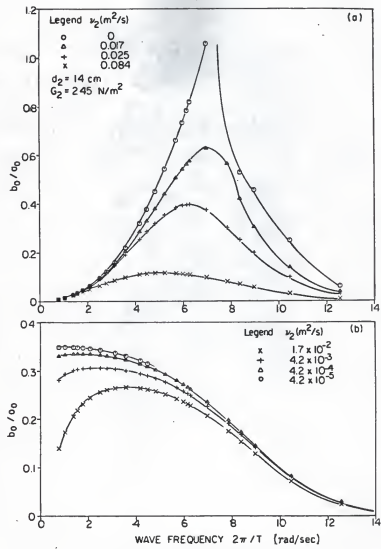


Fig. 4-10. Frequency Responses of the Water-Mud System, Mud is Assumed as (a) Viscoelastic Material; (b) Viscous Fluid.

Note that the decrease in mud bed response for a high-frequency wave is because deep water waves do not touch the bottom. However, the mud bed also shows less response for low frequency waves. This may be interpreted as follows. Longer waves have a more uniform bottom pressure in the longitudinal direction and small vertical velocity. Therefore, the momentum transferred via the interfacial pressure, $p \partial\zeta/\partial x$, diminishes. In the extreme case, i.e., $\partial\zeta/\partial x = 0$, the pressure work is zero. Momentum can be transferred only by the interfacial shear force and is comparatively low. Therefore, the response also decreases.

The significance of resonance behavior of the wave-mud system is that this feature may be utilized to identify the viscoelastic constants G and μ . A similar process, the Resonant Column Method (Richart et al., 1970), has previously been developed to measure the Young's modulus and shear modulus for clays with typically low water content. Although this issue is beyond of the scope of this study, it is an interesting topic for further investigation.

In the multi-layered model, each mud layer could have resonance by showing great movement. However, this was not observed in the modeling of the six experimental runs. Further conclusions regarding resonance phenomenon are pending a better understanding of the effects of depth-varying mud properties.

CHAPTER 5 VISCOELASTIC PROPERTY CHARACTERIZATION

5.1 Introduction

Experiments to examine whether the mud behavior follows the Voigt model or the Maxwell model for viscoelastic behavior were conducted. The creep characteristic at constant load of the Maxwell element was utilized as the criterion to check mud response. The procedure used and results are presented in this chapter. Next, the manner in which the linear response of the Voigt element (at small strain, < 0.1 rad) was used to obtain the viscoelastic constants, G and μ , is described. Finally, experiments to obtain the Bingham yield strength and the apparent viscosity needed for the Bingham model described in Chapter 3 are presented.

5.2 Relaxation Test

A Maxwell element behaves like a fluid when the load period is greater than the retarding time μ/G (Malvern, 1969). For a constant load, the Maxwell element exhibits creep. Therefore, a constant shear load on the mud and the associated (angular) displacement information can be utilized as a means to check whether the mud behavior is closer to a Voigt or a Maxwell element. Based on this concept, relaxation tests were conducted.

5.2.1 Apparatus

A Brookfield viscometer (model LVT), miniature vanes, a video camera and recorder, an angular displacement pointer attached to the vane shaft, and a 30 cm dial scale for the displacement pointer were assembled to measure the shear stress and the associated response, i.e., angular displacement, of mud. Figures 5-1a,b show this system. The video camera, which was hung above, recorded both the dial reading from the viscometer and the angular displacement indicated by the displacement pointer. Elapsed time was also recorded by a timer with an accuracy of 0.1 second.

The viscometer (see Fig. 5-2) had eight rotating speeds from 0.3 to 60 rpm in eight unequal increments, and a maximum driving torque, T_m , of 673.7 dyne-cm. The vane was driven through the calibrated spring by a synchronous motor run at a selected constant speed. The torque acting on the spring was read from the dial meter as percentage of the maximum torque. Initially the vane and the motor did not run at the same speed. However, at steady state, these two were synchronous. The vanes (see Fig. 5-3) were made of stainless steel; the dimensions are given in Table 5-1.

The mud samples were prepared to simulate the mud beds in the wave erosion tests. The details are as follows. Two pieces of 10 cm \times PVC pipe, one 15 cm (sealed at one end to provide a bottom), and the other 30 cm (both ends open), were taped together to build a sediment slurry container as shown in Fig. 5-3. The total length was 45 cm. Kaolinite and mud slurry (see section 6.3 in Chapter 6 for detail), with roughly the same sediment concentration used in the wave flume, were poured

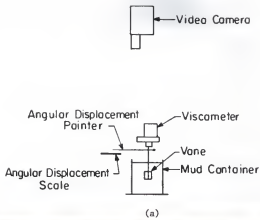


Fig. 5-1. Apparatus for Relaxation Tests and Viscoelastic Constant Measurement. (a) System Diagram;
(b) Top View.

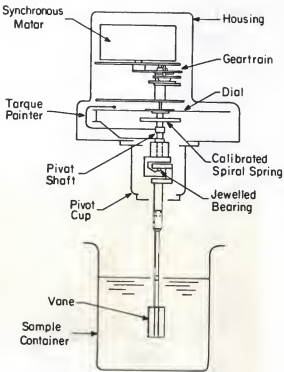


Fig. 5-2. Structure of Brookfield Viscometer.

Table 5-1. Vane Dimensions

Vane No.	Diameter D_v (cm)	Height H_v (cm)
1	1.0	2.0
2	1.5	2.0
3	2.0	2.0
4	2.0	4.0

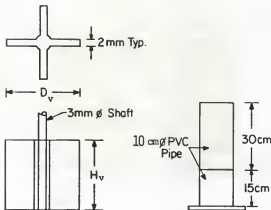


Fig. 5-3. Miniature Vane and Sample Container.

into the container and allowed to settle for the same period of consolidation as each run, i.e., two days, one week, and two weeks. The overlying water was drained out at the end of each consolidation period and the upper PVC pipe was carefully removed. Mud in the bottom PVC pipe provided a sufficiently large medium for a vane to be rotated with negligible boundary effects.

5.2.2 Procedure

An appropriate vane was selected and hooked to the viscometer such that the torque readings would not be too small to lose accuracy nor too large to exceed the maximum capacity of the driving spring. The vane was inserted in the mud at a pre-determined elevation. A motor speed was selected, e.g., 0.3 rpm.

When the motor started to turn, torque was built up in the driving spring since the vane motion was resisted by the mud. Meanwhile, the mud deformed with an angular deformation rate which was much smaller than the motor speed. Therefore, the torque kept building up in the spring until it exceeded the yield strength of the mud. This process was recorded by the video camera and analyzed later to characterize the mud behavior and to determine the shear modulus and the viscosity of the mud.

The motor was turned off once the vane and motor were running at steady state, i.e., same constant speed. The position of the angular displacement pointer and the residual torque were also recorded by the video camera for a period not less than 10 hr.

5.2.3 Results

Figures 5-4 through 5-6 show the residual torque and angular displacement versus elapsed time after the motor was turned off. Negative numbers, e.g., -1.5 cm, indicate the depth from the mud surface to the center of the vane. A sharp decrease in the torque, along with a rapid increase in the angular displacement, was observed during the first few seconds. Later the torque and angular displacement changed much less significantly. After 5 to 40 minutes, depending upon the consolidation period, the torque and the angular displacement pointer did not change any farther and an equilibrium state was attained. It is noticed that the finite residual torque indicates non-relaxation of the shear stress in the mud under a constant shear load. The initial response observed during the first few seconds was due to inertia effects of driving shaft and vane. The motor stopped immediately once it was turned off, but the vane could not stop right away. Therefore, the initial relaxation of torque in the driving spring was due to the relative angular displacement between the motor and the vane with little contribution from mud creep. It was also noticed that less time was required to reach the equilibrium state for a more consolidated mud. For example, about 10 minutes was required for the Cedar Key mud with a one-week consolidation period, but the time increased to 40 minutes for the Cedar Key mud with a two-day consolidation period. The described experiments thus provided evidence that the selected muds did not behave as a Maxwell element since they resisted a constant shear stress. Therefore, the Maxwell element was

not considered further for mud modeling. Material constants for the Voigt element, G and μ , were next obtained as follows.

5.3 Tests for Material Constants of Voigt Element

The shear resistance for a Voigt viscoelastic material is the sum of elastic resistance and viscous resistance. The constitutive equation is given below again for convenience:

$$T' = 2G E' + 2\mu \dot{E}' \quad (5-1)$$

The first part on the right hand side represents the shear response of a linear elastic solid. The second part represents the behavior borrowed from a Newtonian fluid, but the physical meaning is somewhat different. Equation 5-1 is restricted to small strain, and μ is a factor to account for the internal friction loss and should not be construed as the momentum transfer coefficient. To measure the material constants, G and μ , an apparatus which can shear the material at a constant shearing rate is required. However, the Brookfield viscometer does not provide this capability because initially the vane and the motor run at different speeds. In the small deformation range, however, the variation of the shearing rate was not too significant. Consequently the average shearing rate was selected to estimate the shear modulus and the viscosity.

As previously noted, the initial stress-strain behavior recorded by the video camera was used to obtain the material constants. The maximum shear strain for this purpose was selected to be less than 5 degrees (0.087 rad), which can be considered as small strain, also reported in laboratory tests (Schuckman and Yamamoto, 1982). The

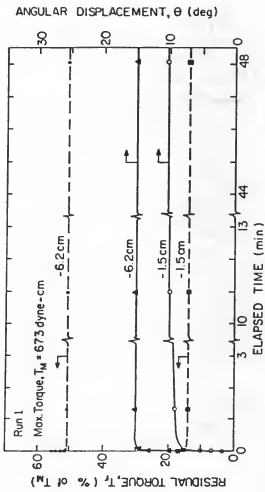


Fig. 5-4. A Plot of the Residual Torque and Angular Displacement versus Elapsed Time for Run 1, Kaolinite with One-Week Consolidation Period.

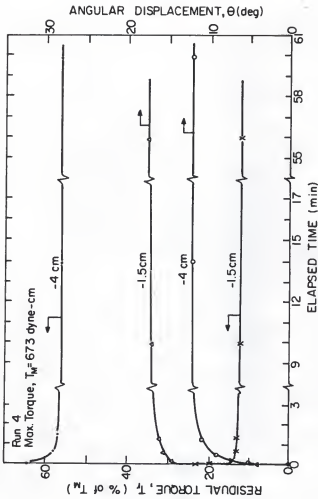


Fig. 5-5. A Plot of the Residual Torque and Angular Displacement versus Elapsed Time for Run 4, Cedar Key Mud with One-Week Consolidation Period.

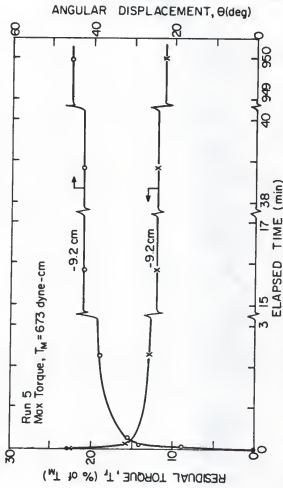


FIG. 5-6. A Plot of the Residual Torque and Angular Displacement versus Elapsed Time for Run 5, Cedar Key Mud with Two-Day Consolidation Period.

torque, shear stress, τ , vane diameter D_v , and vane height H_v are related as follows (Das, 1983):

$$\begin{aligned} \text{torque} &= \text{shear force} \times D_v/2 \\ &= \tau \pi D_v (H_v + D_v/6) D_v/2 \end{aligned} \quad (5-2)$$

Given the vane geometry and read-out torque, τ can be determined. The associated angular displacement (shear strain, θ) and time were also read out from the video tape.

Figure 5-7 shows an example of the relationship between τ , θ , and the associated time rate of shear strain, $d\theta/dt$, for Run 5. A reasonably linear response between τ and θ demonstrates that the Voigt model is applicable. The slope of the interpreted straight line gives the shear modulus. The intersection at the shear stress axis, τ_u , which is due to the viscous term $2\mu E = \mu d\theta/dt$, therefore gives the viscosity $\mu = \tau_u / (d\theta/dt)$. The rate of shear strain ranged from 0.049 to 0.15 deg/sec, with a mean, representative value of 0.085 deg/sec.

The vane was run at three elevations, 1.5, 3.9, and 6.2 cm, below the mud surface. This gave information of the vertical variation of shear modulus and viscosity data needed to run the multi-layered hydrodynamic model developed in Chapter 4. To simplify input needs as well as to smooth the data, the shear moduli and viscosities were correlated with the mud dry density, ρ_d , obtained for each experimental run. See Section 7.2.1 in Chapter 7 for details. Figures 5-8 a,b show the empirical correlations of the dry density on the linear scale with the shear modulus and viscosity on the logarithmic scale. The shear modulus appears to be well correlated with the density, except for Run 2. The data indicate that a denser mud has a higher shear modulus, as

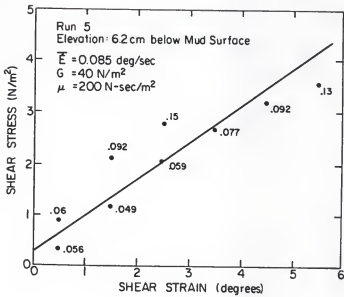


Fig. 5-7. A Plot of Shear Stress against Shear Strain for Determination of Viscoelastic Constants. The numbers are rate of shear strain. The average rate of shear strain is 0.085.

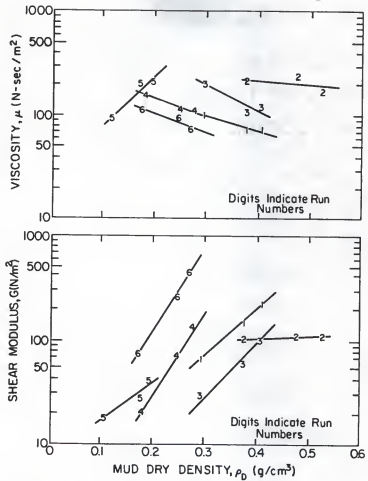


Fig. 5-8. Relationship between Viscoelastic Constants and Mud Dry Density. (a) Viscosity; (b) Shear Modulus.

would be expected. Also a longer consolidation period gave a higher shear modulus even when the dry densities were quite close. This reflects the gelling effects of cohesive sediment. The correlation for the viscosity is not as good. However, there was a strong indication that, with the exception of Run 5, which had the lowest density, the viscosity decreased as the density increased. When viewed in the light of the viscoelastic behavior characterized by Eq. 5-1, this behavior would be expected since soft muds exhibit higher shear strain and, consequently, more energy dissipation, i.e., higher damping coefficient, than denser muds. For the particular case of Run 5, the dry density was less than 0.2 g/cm³. This may imply a critical value corresponding to a different behavior, noting that the viscosity must eventually decrease to that of water as the dry density approaches zero. However, further consideration on the observed trends must await more data and better apparatus.

The correlation equations and the coefficients G_0 , μ_0 , m , and n are listed in Eqs. 5-3, 5-4, and Table 5-2.

$$G = G_0 \exp(m\rho_D) \quad (5-3)$$

$$\mu = \mu_0 \exp(n\rho_D) \quad (5-4)$$

Table 5-2. Coefficients of the Correlation Equations

Run	G_0	m	μ_0	n
1	3.0	10.63	270	-3.38
2	63.0	0.56	305	-0.89
3	0.74	12.14	1150	-5.98
4	0.78	18.23	330	-4.12
5	7.4	8.43	26	11.11
6	3.0	18.65	250	-4.34

As noted in Chapter 2, the shear modulus may be reduced when subjected to an oscillatory load. However, the rate and degree of reduction are dependent on the strain amplitude and on the number of cycles. Formulations for estimating the reduction are not currently available, although 20% to 45% reductions have been reported (Schuckman and Yamamoto, 1982). Therefore, a multiplier, $M_g = 0.8$, was selected to account for the bed stiffness reduction due to wave loading.

5.4 Tests for Rheological Parameters for Bingham Fluid Model

The Bingham yield strength and the apparent viscosity of mud bed were measured by operating the Brookfield viscometer at various rotational speeds. This information was required to run the 1-D Bingham model developed in Chapter 3. A miniature vane was used in order to minimize the disturbance of the mud sample. A standard fluid (viscosity 95 centipoises at 25 degrees centigrade) was also available for calibration purpose.

Since the elastic resistance force is overcome when the motor and the vane run at the steady state, the relationship between the tangential velocity, u , and the torque given by Gularce (1978) can be applied:

$$\begin{aligned}
 \text{torque} &= \text{drag force} \times D_v/2 \\
 &= \tau \pi D_v (H_v + D_v/6) D_v/2 \\
 &= \pi \mu \left(\frac{2u}{D_v} - \frac{du}{dr} \right)_{r=\frac{D_v}{2}} D_v (H_v + \frac{D_v}{6}) \frac{D_v}{2} \\
 &= \pi \mu \Omega D_v^2 (H_v + \frac{D_v}{6}) \quad (5-5)
 \end{aligned}$$

where D_v is the diameter swept by the vane, Ω is the angular speed of the vane and τ is the shear stress.

Given the vane geometry, the rotation speed, and a torque read at steady state, the viscosity can be determined. The vane was first tested by using the standard fluid and gave a satisfactory value — 100 centipoises at 27 degree centigrade. This result demonstrated that a vane could be used to perform the viscosity measurement.

A properly selected vane was inserted into the mud at a given elevation. The rotational speed was started at 0.3 rpm and the dial reading of the torque was taken after the dial meter reached a steady state. The speed was then step-increased and another reading was made. This procedure was repeated up to the maximum speed, or up to the point when the maximum torque had been reached. The rotation speed was then decreased one step at a time and the torque was read again until the speed was reduced to 0.3 rpm. The vane was then moved down to another elevation, and the same procedure repeated.

Figure 5-9 shows a typical result of the stress-strain rate relationship for a kaolinite bed, Run 1. The paths are different for increasing and decreasing strain rates. This type of behavior reveals that the viscosity depends on the previous stress experience (Krone, 1963). Here the mean curve was selected for simplicity (solid line). The Bingham yield strength, K , and the apparent viscosity, μ , are given in Fig. 5-9. This figure demonstrates that the mud behaves like a pseudoplastic fluid at low rates of strain. Another result for a kaolinite bed, Run 3, given in Chapter 3, shows a similar behavior.

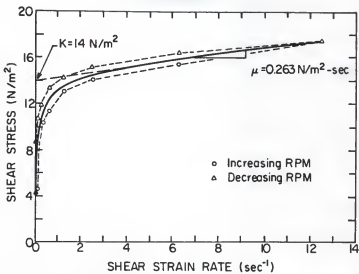


Fig. 5-9. Shear Stress versus Shear Strain Rate Obtained from Kaolinite Bed, Run 1, 6.2 cm below Mud Surface.

CHAPTER 6
EROSION TESTS: FACILITY AND PROCEDURE

6.1 Introduction

Wave erosion tests were performed to observe sediment erosion and entrainment, mud bed motion, and wave attenuation. The ultimate goal was to find an erosion rate function. Bed shear stresses obtained from the multi-layered model were combined with the data on rate of erosion to meet this objective. Dye tests to observe the wave dispersion phenomena were also conducted. Test facility, instruments and procedures are described in this chapter. Results and discussion are presented in Chapter 7.

6.2 Wave Flume

The tests were conducted in an existing flume (see Fig. 6-1) which was designed originally for other purposes. Therefore, minor modifications of this flume were made to conduct the described tests. The flume dimensions were as follows: length 20 m, width 45.8 cm, and height 45 cm. The entire flume was made of plexiglass, and therefore, provided a good means for visual observation. Although it could be adjusted for slope, it was kept horizontal for all the tests .

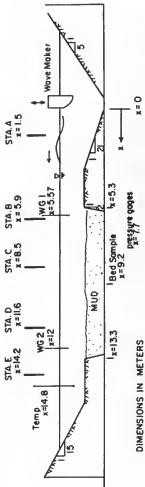


Fig. 6-1. Wave Flume for the Erosion Experiments.

A plunging-type wave maker was added at the upstream side, $x = 0$, to generate regular waves. The wave height and period could be adjusted by a DC motor controller. Although the maximum wave ($H = 9$ cm, $T = 0.85$ sec) was nearly breaking, the waves for the erosion tests were kept below that value in order to avoid strong wave breaking-induced turbulence. A false bottom, also made of plexiglass, was set up to hold the sediment in a 8 m long test section forming a trench from $x = 5.3$ to 13.3 m with side slopes of 1 in 2. An impermeable, sloped beach, 1 in 5, covered with plastic door mats (which gave adequate surface roughness for energy dissipation) was installed at the upstream end to damp out water level fluctuations caused by the wave maker and its support structures. At the downstream end, a plexiglass board was installed to provide a 1 in 15 sloped beach. Plastic door mats were also placed on top of this sloped beach for further reducing wave reflection.

Prior to placing the mud in the test section, a temporary false bottom made of wooden boards was placed over the test reach to simulate a rigid, horizontal bottom over the test section (the elevation of this wooden bottom was the same as that of the permanent false bottom). In this way, wave reflection and wave decay in the flume could be checked and horizontal velocities over a rigid bed measured for a given wave field. This temporary bottom was removed prior to mud placement.

6.2.1 Wave Reflection

In tests to check for wave reflection, two capacitance type wave gauges, separated roughly by 0.25 (or 0.75) wave lengths, were used to

obtain digitized wave profile data via a data acquisition system (described later in Section 6.5.4). A method described by Goda and Suzuki (1976) was used to obtain the wave reflection coefficients. They varied from 0.06 to 0.20, depending upon the wave conditions, with an average of about 0.13. These tests ensured that wave reflection in this flume was not too significant, and that progressive water waves could be generated.

6.2.2 Wave Horizontal Velocities

Horizontal velocity profiles above the rigid temporary false bottom were measured in the wave field to provide a basis for checking the formulation of horizontal velocities over a rigid bed. Only horizontal velocities were measured because they represent the dominant term in the evaluation of the bed shear stress. The current meter used is described later in Section 6.5.7. Horizontal velocity amplitude profiles for the rigid bed environment showed about $\pm 10\%$ deviation from that predicted by the small amplitude wave theory.

6.2.3 Wave Decay

Wave decay in the rigid bottom environment was also measured. Two wave gauges mounted at the upstream and downstream ends of the temporary false bottom were used to record wave heights. Data were fed into Eq. 4-2 to obtain the wave decay coefficient which resulted from friction at the bottom, side walls, and from leakage between the temporary false bottom and the side walls. An average value of 0.04 m^{-1} was obtained.

6.3 Sediment

The sediments used were a commerical kaolinite and an estuarial mud from Cedar Key, Florida, on the Gulf of Mexico coast. Data on shear modulus and viscosity of these sediments are presented in Chapter 5. Clay mineralogical data, mud treatment, and bed preparation were as follows.

6.3.1 Kaolinite

The kaolinite was purchased from EPK Division of Feldspar Corporation located at Edgar, Florida. Its commercial name is "Pulverized Kaolin." It is a light beige-colored powder and is available in 23 kg bags. Totally, 9 bags were gradually dumped into a stainless steel mixing tank (diameter 0.75 m, height 1 m, volume 0.44 m³) and mixed with tap water to make a slurry. Part of the slurry was pumped into another plastic tank (0.44 m³) for storage. Slurry circulation (by pumping and gravity) between the mixing tank and the storage tank was carried out two or three times per week to stir up the clay and to allow the material to be completely wetted by tap water. This procedure was maintained for a month to attain an equilibrium state between the pore water and the eroding fluid.

The slurry was then pumped into the test section of the flume. Two temporary partition walls were installed at the two ends of the test section before pumping the slurry and were removed one day before the erosion tests. The slurry started settling immediately. Spatially averaged water-mud interface elevations versus the duration of consolidation, T_{dc} , for the following seven days are shown in Fig. 6-2. A

rapid settling rate during the first 10 hr was observed. For the next 70 hr, the slurry showed a relative fast first stage (primary) consolidation. A second slower consolidation period started after 80 hours. The same elevation data plotted versus T_{dc}^{-1} clearly exhibit this behavior. Breaks in the curve may be interpreted as representing changes in consolidation behavior after 10 and 80 hours (Einstein and Krone, 1962). Small quantities of mud deposited out of the test section due to leakage from the partition walls were sucked out using a small pump.

With the flume clear of sediment everywhere except in the test section, test Run 1 was made. For Run 2 and Run 3, the kaolinite remaining in the test section was stirred up manually and mixed as uniformly as possible. The installation of the temporary partition walls and sediment clearing procedure were the same as for Run 1.

Kaolinite flocculates even in distilled water, although the nature of flocculation is different than in salt water (Parchure, 1984). The dispersed grain size distribution is given by Hayter (1983); the median diameter was 1 μm . The Cation Exchange Capacity (CEC) was given by the suppliers as 5.2-6.5 milliequivalents per 100 grams.

6.3.2 Cedar Key Mud

Cedar Key is a small town on the Gulf of Mexico coast, 95 km west of Gainesville, Florida. Mud was collected from a tidal flat (on the south side of State Road 24, 1.5 km from Cedar Key city limits) by shovel at low tide. The mud was put in an aluminum tank (0.5 m^3) and transported back to the Coastal Engineering Laboratory in Gainesville.

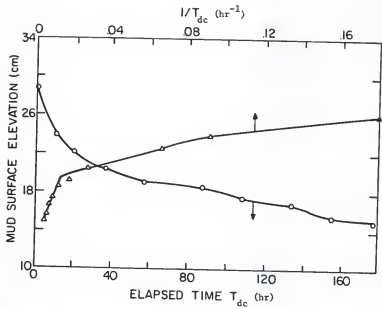


Fig. 6-2. Water-Mud Interface Elevation during Deposition and Consolidation of the Kaolinite Slurry.

Before using the mud it was treated as follows: First, 48 liters of Clorox bleach (5.25% sodium hypochlorite) were poured into the tank and mixed with the mud (about 0.3 cubic meters) to oxidize organic material present and to destroy all micro-fauna. The mixed slurry was then allowed to settle for two to three days. The overlying water was drained out and remixed with tap water to reduce the salinity. The draining and remixing process was repeated 3 times before further treatment. After a week, the mud was then washed through a US no. 50 sieve (with openings of 0.295 mm) to remove the leaves, roots, coarse sand and other debris. The washed-through material was pumped into several storage tanks and allowed to settle again. Since the mud was not enough to fill up the test section, kaolinite from the previous test was added and mixed with the mud. The ratio of kaolinite to mud was about 1:3. Three days later, the overlying water was drained out and the mud was dumped into the mixing tank and then pumped into the flume using a similar procedure as for the kaolinite. This was the mud used in Run 4. The dispersed grain size distribution, obtained by the pipette method (Black, 1965), is shown in Fig. 6-3 with a medium grain size of 2.1 μm . After Run 4, the mud in the flume was transferred back to the mixing tank. Meanwhile, more Cedar Key mud was collected, treated, and added to the material remaining after Run 4, for Run 5 and Run 6. The new ratio of kaolinite to mud was approximately 1:4. The dispersed grain size distribution is also displayed in Fig. 6-3. Although the medium diameter was still 2.1 μm , the distribution was somewhat different. The mud was in a flocculated state in all the runs.

Data of the sediment for all six runs are summarized in Table 6-1. The constitution of clay fraction (grain size less than 2 μm) of the sediment used in Run 4, Run 5 and Run 6 is presented in Table 6-2.

Table 6-1. Sediment Properties

Run	Sediment	D_{50} (μm)	CEC (meg/100g)	Organic Content (%)	Consolidation Period (day)
1	Kaolinite	1.0	5.2~6.5	nil	7
2	Kaolinite	1.0	5.2~5.6	nil	14
3	Kaolinite	1.0	5.2~6.5	nil	2
4	C. K. mud	2.1	65*	4.8	7
5	C. K. mud	2.1	80	4.8	2
6	C. K. mud	2.1	80	4.8	14

*estimated from the clay constitution

Table 6-2. The Composition of Clay Fraction

Sediment	Montmorillonite (%)	Illite (%)	Kaolinite (%)	Quartz (%)
Original C. K. mud	63	14	18	5
C. K. Mud for Run 4	16	15	62	7
C. K. Mud for Run 5 & 6	19	18	56	7

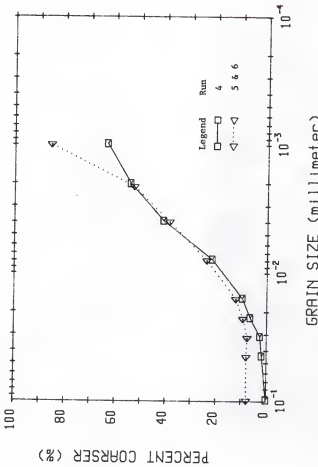


Fig. 6-3. Dispersed Grain Size Distribution for Sediment in Runs 4, 5, and 6.

6.4 Eroding Fluid

Tap water was used to soak the sediment, dilute the natural salinity, and served as the eroding fluid. The chemical composition of the water is given in Table 6-3. A water sample, about 200 cm³, was taken for each run to test for salinity and pH. The salinity was measured by using the Salinity Titration Kit (model POL-H, manufactured by Lamotte Chemical Co.). The pH value was measured by using the Beckman Digital pH meter (model 3500). The temperature of the eroding fluid was also observed. These data are presented in Table 6-4.

Table 6-3. Chemical Composition of the Eroding Fluid
(After Dixit, 1982)

Ion	Concentration (ppm)
Cl ⁻	26
NO ₃ ⁻	0.07
Fe ⁺⁺⁺	0.5
K ⁺	1.4
Ca ⁺⁺	25
Mg ⁺⁺	16
Na ⁺	10

Table 6-4. Eroding Fluid Properties

Run	pH	Salinity (ppt)	Temperature °C
1	8.2	0.6	17.6
2	9.5	0.6	17.9
3	9.9	0.6	22.7
4	9.9	1.2	25.1
5	9.5	1.2	25.4
6	9.9	0.6	25.0

6.5 Instrumentation

6.5.1 Wave Gauges

Two capacitance type wave gauges were installed in the flume to monitor the wave information. One was set up at the upstream end of the test section. The distances between these two instruments were 2.55 m for Run 1, 5 m for Run 2, and 6.45 m for the rest. The second gauge (the one on the downstream side) could be moved to obtain additional wave data from other specified locations. Calibration of the wave gauges was performed by mounting them on a plastic bucket. Water was added or drained out to provide a series of data on the gauge output voltage and water level. A linear least squares method was utilized to obtain a regression equation. Wave data were recorded by the data acquisition system presented later in this chapter.

6.5.2 Pressure Transducer

The dynamic pressure fluctuation within the mud provided data for verifying the model developed in Chapter 4. The time-averaged pressure data also reflect any change in the apparent bulk density, based on Eq. 6-1:

$$\Delta p_{m,n} = \int_{z_m}^{z_n} \rho(z) g \, dz \\ = \bar{\rho}_e (z_n - z_m) \quad (6-1)$$

where $\Delta p_{m,n}$ is pressure difference, z_m , z_n are the corresponding elevations of the pressure transducers, $\bar{\rho}_e$ is the average apparent bulk density between z_m and z_n , and g is gravity. Four pressure transducers

(model PDCR 135/A/F, manufactured by Druck Inc., see Fig. 6-4) were mounted on the side wall at $x = 7.75$ m, at four elevations for the purposes described. The transducers were nearly flush mounted, recessed about 1.5 mm into the wall. This was because of the limited length of the sensor probe. To prevent possible entrapment of air bubbles, the transducers were mounted after the flume was filled with the sediment slurry. This procedure was determined to be feasible, by first using water only and observing that no air bubbles would be trapped. The pressure transducers required +12, 0, and -12 volts DC supply. The maximum output at 2.5 psig was 2.5 volts. The overall



Fig. 6-4. The Pressure Transducer, Druck Model PDCR 135/A/F

accuracy of the unit was 0.1% of full scale. This means that the resolution was 0.0025 psi, which corresponds to a 1.76 mm variation of water level. These pressure transducers (numbered as unit 12, 13, 14, and 15) were calibrated after each test (while mounted on the side wall). Mud was dug out locally, and the water level was raised and lowered to give several pressure readings. The mount elevations were 12.9, 15.2, 10.6, and 6.0 cm from the rigid bottom. These elevations were changed after Run 3. See figures in Appendix B for details. Unit 14 malfunctioned after Run 3 and thereafter only three transducers were used. The outputs were collected via the data acquisition system.

6.5.3 Light Meter

Instantaneous sediment concentration response in the water column during erosion was detected by a photo-sensing device, i.e., a light meter, developed at the Coastal Engineering Laboratory. Figure 6-5 shows the system diagram for this device. Details are given in Appendix C. Although this device was not fully successful, it did yield some encouraging results. However, more effort towards the modification and verification of this device is necessary.

The light meter shown in Fig. 6-5 was completed after Run 4. In Run 2, the light meter, with a LED driver using a sinusoidal wave, was tested but failed because the sinusoidal wave generator was not stable and caused a severe static drift. This made the calibration meaningless. However, relative concentration data, represented by the voltage fluctuation, were still encouraging because the drift was not significant over a short time, e.g., 10 sec. Later, the sinusoidal wave

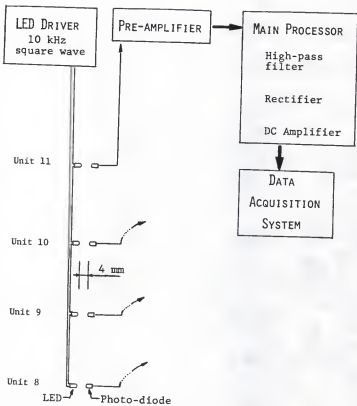


Fig. 6-5. System Diagram of the Photo-Sensing Light Meter.

generator was replaced by a square wave generator, and a stable light source was then obtained.

The light meter had four sensing units--8, 9, 10, and 11. They were used for detecting the sediment concentration at four elevations simultaneously. The meter was mounted at $x = 6.65$ m. The elevation of the meter was selected such that unit 8, the lowest one, was approximately 1 cm above the mud surface. The elevation could also be adjusted with mud surface elevation change.

6.5.4 Data Acquisition System

In the test setup, there were two channels for wave information, four for sediment concentration using the light meter, and four for the pressure transducers. All the data were collected by an IBM Personal Computer via a digitizing interface card (DASH-16) manufactured by Metrabyte Corporation.

The interface card had 16 channels (single end input) for analog to digital (A/D) conversion and 4 channels for digital to analog (D/A) conversion, but only the first feature was used. The maximum throughput rate for scanning multiple channels was 25,000 conversions per second. The A/D conversion could be triggered by software command and the basic software was also provided by the manufacturer. The user merely had to modify these programs to suit the purpose. The operational voltage of input analog signal could be chosen by setting a dip switch in the card. Since most transducers had output voltages between -2.5 to +2.5 volt, the operational voltage was set at this level. The card used a standard 12 bit to convert the data. This

means that the range of data digitized could be varied from -2047 to +2048. The resolution of this system was $5/4096 = 0.0012207$ volts. This value was then related to the accuracy of wave height, sediment concentration, current velocity and pressure measurements. For example, the pressure transducer gave 2.5 volts output at 2.5 psig. The accuracy of the recording system was $2.5/(2.5/0.0012207) = 0.00122$ psi, which was 2 times higher than the pressure transducer's resolution.

The IBM PC collected digitized data at selected times and stored the data into disk files. Each file contained 6 to 10 records. Each record stood for a measurement at a time. A record had 8 headers for title, channel number, identifier, estimated wave period, time, location, elevation, scanning rate, followed by the data points which were in the form of digitized code. The number of data points in a record was dependent on the characteristics of the physical phenomenon and storage space available. Twenty-five waves were selected for all the runs. The computer scanned at a frequency approximately 20 times faster than the wave frequency. For recording 25 waves, 500 data points were necessary. To meet the number required for Fast Fourier Transform, which requires $2^9 = 512$ data points, and another extra 20 data points for the low-pass filter, 532 data points were collected for each record. These data files were written in ASCII form originally, but were later converted to the binary form in order to save storage space.

One drawback of the A/D recording system was that it did not have inertia. Unlike the pen recorder, any noise, usually in the high frequency domain, could get mixed with the signal and then digitized.

Therefore, it was difficult to see a smooth curve even though the true process was smoothly varying. The data record always had spikes.

To remove these spikes, a numerical low-pass filter was added in the computer program, based on the formulation presented in Appendix C.

6.5.5 Suspended Sediment Sampler

For determining the entrainment rate of sediment under wave loading, it is essential to know the time-history of the total suspended sediment mass. Suspended sediment was sampled at several locations in the water column for the following reasons: 1) The applied bed shear stress decreased, sometimes quite significantly, in the longitudinal direction due to the high damping ability of the mud bed. 2) The test section was only part of the flume. Thus, sediment could be advected and/or dispersed beyond the test section.

Five stations (A,B,C,D,E) for suspended sediment concentration sampling were chosen, as shown in Fig. 6-1. At stations B, C, and D, sediment-laden water was withdrawn at four elevations because higher vertical gradients were expected. At station A, where the concentration was the most uniform vertically, one elevation at middle depth was selected to reduce the number of samples. At station E, two elevations (one 2 mm above the false bottom, the other 12 cm above) were chosen. At stations B, C, and D, the sampling elevations were adjusted when necessary, because the water-mud interface elevation changed slowly due to erosion. All samples were taken along the centerline of the flume with the samplers of the type shown in Fig. 6-6. The intake velocity was approximately 40 cm/sec. The sample volume ranged from 20 cm³ to

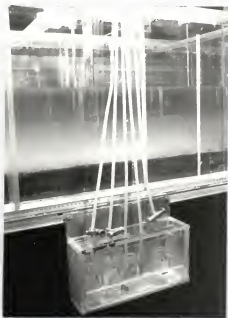
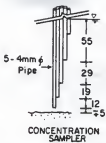


Fig. 6-6. Suspended Sediment Sampler.

70 cm³ depending on the sediment concentration. Samples were stored in bottles for later analysis.

6.5.6 Bed Sampler

In a steady-flow erosion process, Parchure and Mehta (1985) assumed that mud properties (e.g., density, shear strength) remain practically unchanged during erosion. However, it was expected that this assumption would not be valid under wave flows because the mud bed may lose its strength and become soft when subjected to oscillatory shear stress, as discussed in Chapter 2. As noted previously, the reduction of shear strength has been studied by, among others, Schuckman and Yamamoto (1982). To examine whether the density was also being altered by wave loading was a part of this study. Mud bed density profiles were determined, at $x = 9.2$ m, by using a hypodermic syringe to withdraw samples of 1 to 2 cm³ at predetermined elevations. These samples were oven-dried to obtain the dry density.

6.5.7. Current meter

A current meter (model 523, manufactured by Marsh McBirney Inc.) was used to measure the horizontal velocity in the water column. The meter was calibrated for the time constant and system coefficient for an oscillatory flow field. Details are presented in Appendix C. Because it relies on electromagnetic field for velocity measurement, this meter has two restrictions. First, the probe can not be placed close to the water-air or water-bed interface due to the drastic change of material density and conductivity of electromagnetic field, which

results in an unrealistic output. Second, the meter generates strong interference with other instruments which means that only the current meter can be used at a given time. Other data had to be collected separately. The meter has output on the order of 50 millivolts. In order to increase the resolution, an amplifier for 10-fold amplification was added between the meter output and the data acquisition system. At the time of Run 6, the meter showed erratic response and therefore, data were not taken.

6.6 Procedure

The sediment beds were prepared as described in Section 6.3. The eroding fluid was described in Section 6.4. Water samples were taken just before erosion tests to obtain background sediment concentrations. Mud surface elevations and bed samples were also taken to obtain initial conditions. The wave generator was then turned on to produce regular waves. The first wave loading was maintained for 3 to 7 hours, then the wave loading was increased and maintained for another 3 to 7 hours. For Run 6, a third wave loading was maintained for 4 hours. Suspended sediment samples were taken for each wave loading at variable time intervals, e.g., 15, 30, 30, 60, 60, ... minutes, with minor changes for each run. Wave height, period, pressure, and light meter outputs were collected on another schedule, which had smaller time intervals, e.g., 7.5, 15, 15, ... minutes. Mud surface elevations and bed sediment samples were taken several times during all six runs.

6.6.1 Processing of the Digital Codes

The treatment of digitized codes for a record, e.g., wave surface profile, is described below as an example. The codes in the record were converted back to the actual water surface elevations by using the calibration equation. The data were then scanned by the computer to find all the peaks and troughs. The vertical distance between a peak and the next trough gave a wave height. The average value of 25 measured wave heights was stored as a representative wave height over that time, i.e., 25 seconds for a 1-second wave. This procedure also gave measured wave periods since the scanned frequency and the number of data points between two successive peaks, or troughs, were known. The average value of 25 wave periods was saved as a representative period over that time. This type of analysis gave one data point for wave height and period in Fig. 6-7. The same type of procedure was used to obtain the average dynamic pressure fluctuation, sediment concentration fluctuation from light meter, and the velocities, using the electromagnetic current meter. The average of the entire time series (512 data points) gave a representative wave-averaged value, e.g., the wave-averaged pressure and the wave-averaged concentration from the light meter, over that duration (25 seconds for a 1-second wave).

Wave data for Run 3 are given in Fig. 6-7 as an example. For other runs, see figures in Appendix D. Because the wave generation system was not perfectly synchronized, the wave heights and periods were not precisely constant for each wave loading. Average values were selected as the representative wave height and wave period. Wave heights along the length of flume bed were plotted on semi-log

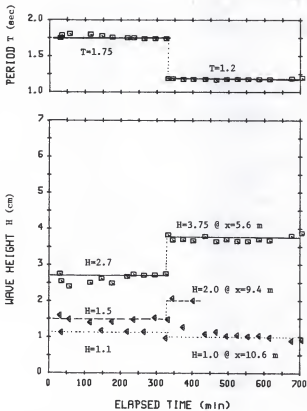


Fig. 6-7. Wave Loading for the Erosion Test, Run 3.

coordinates, based on Eq. 4-2, to obtain the wave decay coefficient k_{im} . See Fig. 6-8 for example. The decay coefficients found are presented in Table 6-5.

The average wave heights, periods, water layer thickness, spatially-averaged total mud thickness, and the duration of each wave loading are summarized in Table 6-5 and were also used in the multi-layered model developed in Chapter 4. The calculated maximum bed shear stress, τ_{bo} , the spatially averaged maximum bed shear stresses, $\langle \tau_b \rangle$, and the wave Reynolds number were presented earlier in Table 4-2, Chapter 4.

6.6.2 Suspension Samples

In all, 1516 sediment samples were collected: 391 samples for Run 1, 210 samples for each run from Run 2 through Run 5, and 285 samples for Run 6. They were analyzed gravimetrically for sediment concentration by using a filtration unit. This unit included a Millipore vacuum pump, two 300 ml beakers, one filter holder, 25 ml pipette, filter paper with a mean pore size of 0.45 micron, a balance (model H6T, manufactured by Mettler Instrument Corp.) with 0.0001 gm accuracy and an oven. Details are given by Yeh (1979).

Depth-averaged sediment concentrations for stations B, C, and D were calculated based on the measured concentration profiles. For station A, the concentration at one elevation was assumed to represent the depth-averaged concentration. At station E, concentration data collected at four elevations (Run 1 only) were used to obtain a basis

Table 6-5. Wave Conditions for Erosion Tests.

Run	Wave height (cm)	Period (sec)	Water depth (cm)	Total mud thickness (cm)	Duration of each wave (hr)	k_{im} (m^{-1})
1-1	3.3	1.9	21.7	14.0	7.0	0.10
2	5.4	1.3	24.2	11.5	7.3	0.13
2-1	2.7	1.9	19.2	11.5	5.5	0.03
2	4.4	1.2	19.7	11.0	5.5	0.04
3-1	2.7	1.8	16.2	14.5	5.0	0.15
2	3.8	1.2	18.2	12.0	6.3	0.18
4-1	3.7	1.6	26.4	9.3	4.8	0.03
2	6.2	1.1	28.7	7.0	5.0	0.04
5-1	4.4	1.7	19.7	16.0	3.8	0.10
2	6.8	1.2	21.1	14.6	5.1	0.08
6-1	3.8	1.8	24.7	11.0	3.0	0.11
2	5.6	1.4	25.2	10.5	4.0	0.09
3	7.3	1.0	25.2	10.5	4.0	0.06

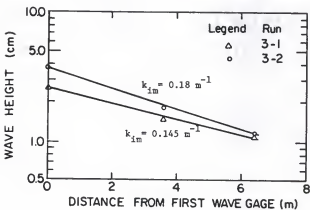


Fig. 6-8. A plot of Wave Height against Distance along the Flume.

which enabled the depth-averaged concentrations to be estimated from only two data points (Run 2 to Run 6) in the water column.

These depth-averaged sediment concentrations (obtained at different positions in the flume) were then used to obtain the corresponding total suspended sediment mass.

6.6.3 Wave-averaged Mud Surface Elevation

The water-mud interface not only oscillated with the wave but the wave-averaged mud surface elevation also varied slowly due to the dynamic features associated with the erosion process. The wave-averaged mud surface elevations were recorded at eight locations, i.e., $x = 5.57m, 6.57m, 7.57m, 8.57m, 9.57m, 10.57m, 11.57m$ and $12.57m$, by visual observation from the side wall at several times.

CHAPTER 7
EROSION TESTS: RESULTS AND DISCUSSION

7.1 Introductory Note

In this chapter, erosion test results and discussion are presented. An erosion rate expression is developed and the process of entrainment of the high density near-bed suspension into the upper water column is examined.

7.2 Results

7.2.1 Bed density

Figure 7-1 shows the density profile changes with time in Run 1 as an example. Others are presented in Appendix D. The figure clearly shows that the density generally decreased at the initial stage (less than 300 minutes in Run 1) and increased later. The initial decrease in density may have been due to a breakup of the initial soil structure. The later consolidation of the bed may have resulted from the development of a new soil structure. This phenomenon is similar to what occurs in a fine sand bed under seismic loading (Prakash, 1981). The destruction of dense sand grains results in an increase in the void

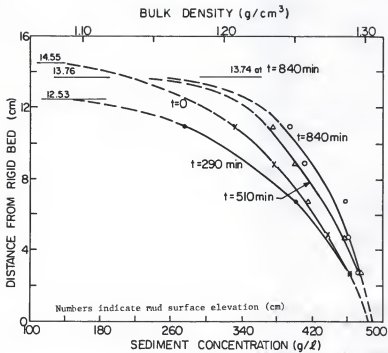


Fig. 7-1. Measured Mud Density Variation due to Wave Action, Run 1.

ratio at the beginning. At a later stage, the void ratio decreases and the pore water is squeezed out to yield a more compacted bed. The effect of breaking the inter-particle bond, however, is not involved, although this may as well be a causative agent in the present case which involves cohesive material. A volumetric swelling at the initial stage was also observed as the mud surface rose at the upstream end. See Fig. 7-2. This phenomenon indicated that the mud bed properties indeed did change measurably with time.

In order to further examine the bed density change, the depth-averaged mud dry density, $\bar{\rho}_p$, was selected as an index. It was normalized by the initial value, $\bar{\rho}_{D0}$. Figure 7-3 shows that the depth-averaged densities did, in general, increase with time, ultimately becoming 5-15% higher, although local density changes were somewhat different. Runs 4 and 6, using the more dense Cedar Key mud, showed a decrease in density during the first wave loading. This may have been the case because Cedar Key mud had a different clay composition (see section 6.3.2 in Chapter 6 for details) and, therefore, resulted in a higher volumetric swelling and density decrease than kaolinite. Run 3, the soft kaolinite bed, displayed the highest increase in density, about 15% after 5 hours.

To simplify the bed-density data as input for the multi-layered model developed in Chapter 4, time-averaged density profiles were selected. Figure 7-4 shows the dry density normalized by the

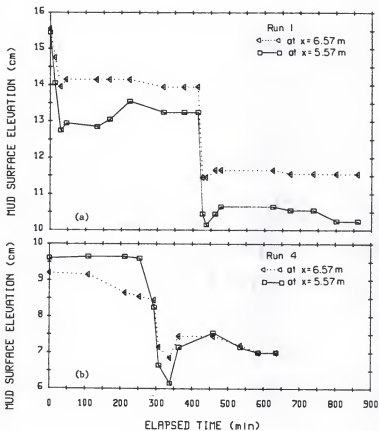


Fig. 7-2. Volumetric Swelling of Mud Bed Caused by Wave Action.
(a) Run 1; (b) Run 4.

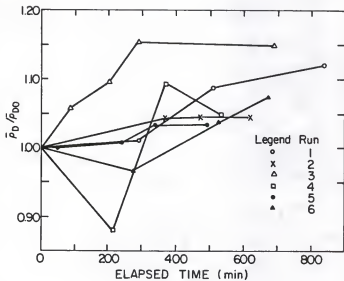


Fig. 7-3. Depth-Averaged Bed Density Variation Caused by Wave Action.

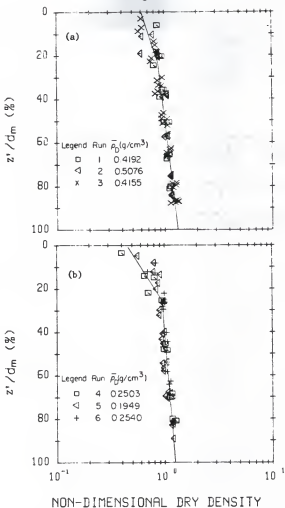


Fig. 7-4. Dimensionless Mud Dry Density Profile.
 (a) Kaolinite; (b) Cedar Key Mud.

depth-averaged dry density versus the normalized mud elevation, z'/d_m , where z' is increasing downward from the water-mud interface and d_m is the total mud bed thickness. This relationship may be considered to be applicable to the entire test section. Equation 7-1 shows the relationships for Run 1 through Run 3, while Eq. 7-2 is for Run 4 through Run 6:

$$\rho_D / \bar{\rho}_D = \begin{cases} 0.60 \exp(1.5755 z'/d_m), & z'/d_m < 0.25, \\ 0.78 \exp(0.5261 z'/d_m), & z'/d_m > 0.25, \end{cases} \quad (7-1)$$

$$\rho_D / \bar{\rho}_D = \begin{cases} 0.46 \exp(2.8307 z'/d_m), & z'/d_m < 0.25, \\ 0.84 \exp(0.4095 z'/d_m), & z'/d_m > 0.25, \end{cases} \quad (7-2)$$

The bulk density, ρ_B , required to run the multi-layered model, was obtained by using Eq. 7-3 and assuming that the grain density $\rho_g = 2.6 \text{ g/cm}^3$ and water density $\rho_w = 1 \text{ g/cm}^3$:

$$\rho_B = \rho_w \left(1 - \frac{\rho_D}{\rho_g} \right) + \rho_D \quad (7-3)$$

7.2.2 Pressure Response

Figure 7-5 gives an example (Run 1) of the instantaneous pressure response in the kaolinite bed. The surface water wave profile, η , at the same location is also included. This figure indicates that the pressure in the mud bed was periodic with no phase lag with respect to η . However, the pressure response was more irregular than the wave profile. A comparison of measured pressure amplitude with model prediction was presented in Chapter 4. Some interesting observations on the pressure response are discussed here.

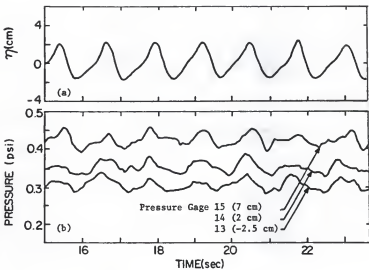


Fig. 7r-5. Instantaneous Pressure Response in the Kaolinite Bed, Run 1. (a) Wave Profile; (b) Pressure.

Figure 7-6a shows the average dynamic pressure fluctuation (twice the dynamic pressure amplitude) defined in section 6.6.1, Chapter 6, from two pressure transducers, unit 14 and unit 15, in Run 1. This figure indicates a pressure drop at the beginning. After 80 minutes, the fluctuation increases, and reaches a peak after 100 minutes despite the fact that the waves were fairly constant (see Appendix D). The associated wave-averaged pressure (see Fig. 7-6b; defined in section 6.6.1, Chapter 6) also indicates that something interesting was happening at this time. The behavior of wave-averaged pressure can be interpreted as the change of apparent density by using Eq. 6-1. This change is shown in Fig. 7-7. The ordinate is a non-dimensional apparent density $p' = \bar{p}_e / \bar{p}_{eo}$, normalized by the initial value, \bar{p}_{eo} . A decrease (8%) of p'_{14-15} (average apparent bed bulk density between transducer unit 14 and 15) and then an increase (30%) was observed. Similar behavior (decrease and increase) was observed for p'_{12-14} but the change was faster. This may have been the case because unit 12 was closer to the water surface and there was a relatively faster dissipation of the pore pressure.

A possible cause of this phenomenon may be the shear deformation of the soil skeleton and the resulting pore pressure variation, which influenced the pressure data. The initial drop, conceivably due to shear deformation, resulted in an increase of void ratio, and, therefore, a negative pore pressure and a decrease of the apparent density. Later, subsequent shear deformation reduced the void ratio, thus causing a positive pore pressure and a corresponding increase in the apparent density. After the pore pressure was dissipated, the measured

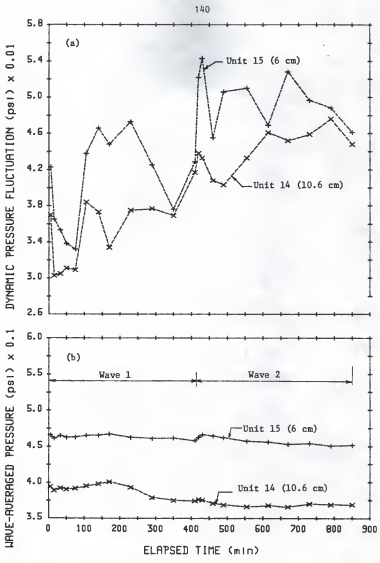


Fig. 7-6. Average Pressure Response in the Kaolinite Bed, Run 1.
 (a) Dynamic Pressure Fluctuation; (b) Wave-Averaged Pressure.

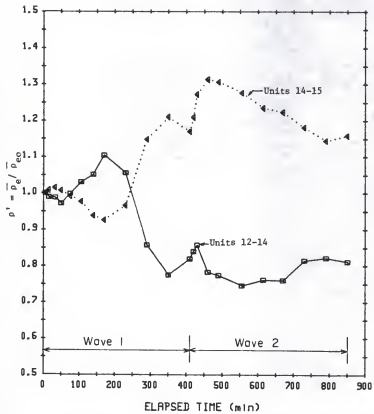


Fig. 7-7. Variation of Dimensionless Apparent Bulk Density Caused by Wave Action, Run 1, Normalized by the Initial Value.

pressure decreased again. This statement has been based on the assumption that the floc structure remained unchanged. However, the possibility that flocs may have been broken and reformed when subjected to wave-induced shear load further complicates the issue. A better understanding of this behavior requires further study.

The above observations indicate that pore pressures should be measured simultaneously with the total pressure, in order to elucidate the nature of time-dependent changes in the bed. Other possibilities, e.g., the change of water depth caused by erosion/deposition of sediment, also need further study.

7.2.3 Instantaneous Sediment Concentration

Figure 7-8a shows the output (volts) from unit 8 of the light meter for Run 3, a kaolinite bed with a wave period of 1.2 seconds. Unit 8 was placed 1 cm above the bed surface. This plot indicates that at times two peak sediment concentrations may occur in a wave period. For meters further away from the bed (not shown), the sediment concentration varied with the water wave frequency.

Figure 7-8b shows light meter outputs which correspond to the instantaneous sediment concentrations at a certain elapsed time in Run 5-2. This figure clearly demonstrates that at unit 8, about 1 cm above mud surface, the sediment concentration oscillation was strong, approximately 1.5 g/l (see calibration curves in Fig. C-8, Appendix C). The period was basically equal to the wave period although a second peak did show up in the trough. At unit 9, 6 cm above the mud surface, the oscillation was greatly reduced. At unit 10, 11 cm above mud surface,

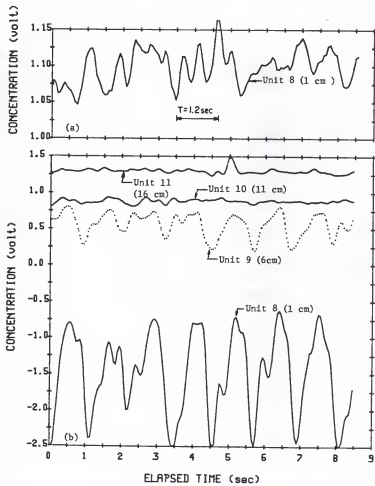


Fig. 7-8. Instantaneous Sediment Concentration Response in the Water Column. (a) Run 3; (b) Run 5.

there was almost no fluctuation. The wave-averaged concentrations (volts) at $x=6.65$ m are shown in Fig. 7-9, which indicates increasing sediment concentration corresponding to decreasing output voltage, e.g., from 2.3 V to -2.5 V. Unfortunately, the re-adjustment of the zero position and the amplification ratio of the DC amplifier in the main processor broke the linkage between this diagram and the calibration curve. Therefore, absolute sediment concentrations could not be obtained. Figure 7-10 shows the average of 25 sediment concentration fluctuations. It reflects the strength of sediment concentration at four elevations. Unit 8 shows the highest concentration fluctuation. However, when the average concentration was higher than a certain value, e.g., output less than -2 volts, the ability to detect the concentration fluctuation was restricted by the pre-selected operational range, +2.5 V to -2.5 V, in the A/D card. All output voltages less than -2.5 V were read as -2.5 V. For this reason the concentration fluctuation in unit 8 is not shown after 360 minutes.

The above drawback was due to the sole available choice of D.C. amplification ratio in the light meter. Given more options for the zero position and amplification ratio, calibrating for all options, and using a switch to choose one that would be best for a particular condition could solve this problem.

7.2.4. Wave-averaged Suspended Sediment Concentration

Figure 7-11 shows the suspended sediment concentration profiles for Run 1, the kaolinite bed, obtained from the suspended sediment sampler at selected times and locations. This figure demonstrates the

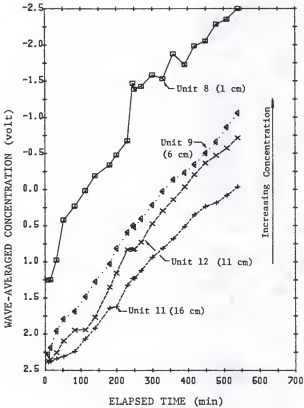


Fig. 7-9. Wave-Averaged Response from Light Meter during Wave Erosion Process.

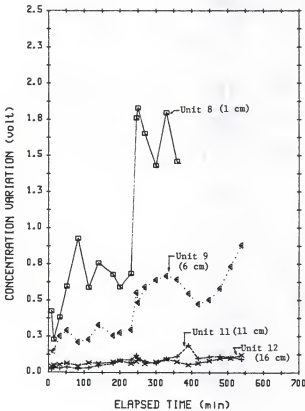


Fig. 7-10. Average Sediment Concentration Fluctuation Detected by the Light Meter during Wave Erosion Process.

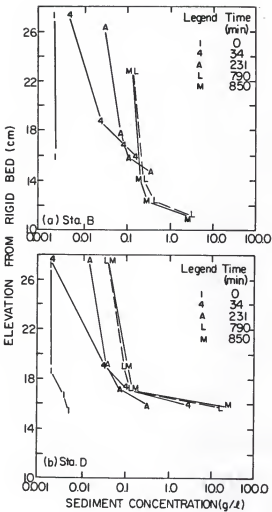


Fig. 7-11. Sample Profiles for the Suspended Sediment Concentration for Run 1. (a) at STA. B; (b) at STA. D.

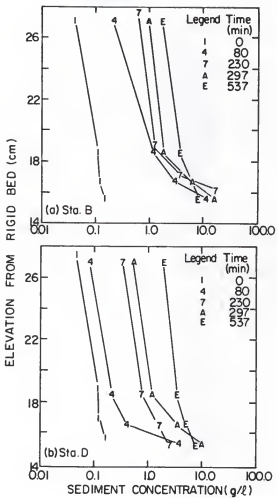


Fig. 7-12. Sample Profiles for the Suspended Sediment Concentration for Run 5. (a) at STA. B; (b) at STA. D

existence of a steep concentration gradient near the mud surface, which also implies the presence of a high concentration layer just above the mud surface. The occurrence of almost the same sediment concentration profiles at times L and M, separated by 60 min., suggests a steady state of the entrainment process. Figure 7-12 shows the same type of data for Run 5, Cedar Key mud, with a similar behavior. However, differences are as follows. 1) the near-bed concentration gradients are not as high as in Run 1, and 2) there is no evidence of a steady state. Both runs show an increasing sediment concentration due to upward entrainment. Other data are presented in Appendix D in a tabular form.

Figure 7-13 shows three (Stations B, C and D) depth-averaged concentration versus elapsed time curves for Run 4. This plot indicates that there was a measurable longitudinal gradient of sediment concentration along the test section, even though the wave-induced shear stresses were quite similar along the length of the bed due to the low wave decay (see Table 4-2, Chapter 4). The maximum depth-averaged concentration occurred at the upstream end, where the bed shear stress was also a maximum. Other runs also showed a similar behavior.

It should be noted that the total suspended sediment mass in the water column was the sum of two masses: M_n obtained by integration of concentrations measured by the samplers, and another sediment mass associated with a high density layer just above the bed but below the level of the lowest samplers. The second one was difficult to measure because of the high concentration gradient and small thickness. Therefore, the total eroded sediment mass was obtained by considering the time-variation of mud bed surface elevation (mentioned further in the

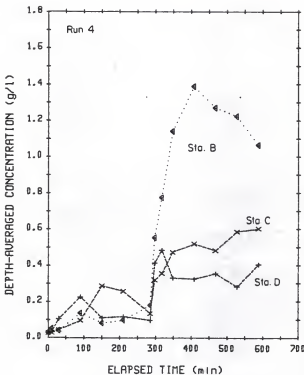


Fig. 7-13. Longitudinal Variation of the Depth-Averaged Sediment Concentration, Run 4.

next section). Data on the mass M_n are presented and discussed in Section 7.3.

7.2.5 Wave-averaged Mud Surface Elevation

Figures 7-14a,b,c show time-variations of the kaolinite bed surface from Run 1 to Run 3, as examples. All data are presented in Appendix D. For Run 1, it is evident that water waves easily eroded out a top thin layer of mud on the upstream side. The eroded mud was transported both upward into the water column and downstream to be piled up at the downstream side. This is shown by the increased mud surface elevation at the downstream side. Also a thin layer of fluid mud, defined here as sediment of concentration greater than 10 g/l (Krone, 1962), appeared at the downstream side with thickness about 2 to 5 mm. The length and the thickness of this fluid mud layer increased as the wave erosion process continued. The maximum thickness was about 1.5 cm at the downstream side. Figure 7-14a suggests that a steady state of bed level had been attained after about 480 minutes.

For a more consolidated bed, e.g., Run 2, the mud had a higher shear strength. Therefore, the bed response was relatively weak and less erosion resulted during the first wave loading. See Fig. 7-14b. However, severe erosion showed up when the wave loading was increased. A steady state was reached after about 570 minutes.

For Run 3, the mud was soft, and oscillatory motion within the mud was easily observed through the side wall. The mud surface elevation got depressed rapidly at the upstream end even with the first small

waves. A steady state was attained after about 450 minutes. See Fig. 7-14c.

Generally, it was found that the mud surface elevation response was closely related to the duration of bed consolidation prior to

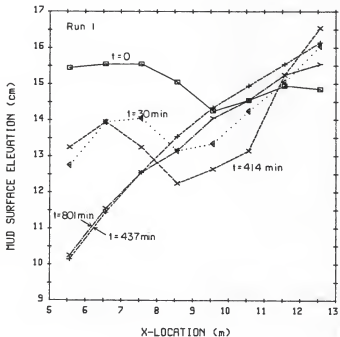


Fig. 7-14. Mud Surface Profiles at Selected Times. (a) Run 1.

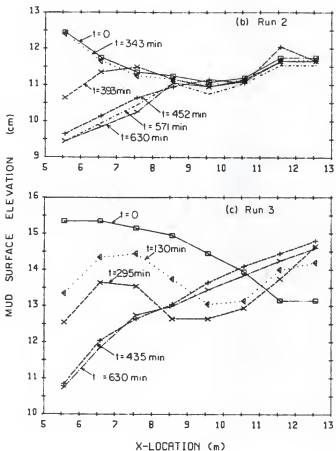


Fig. 7-14 (continued). (b) Run 2; (c) Run 3.

erosion. The longer the consolidation period, the less the response, i.e., more resistance to erosion. Furthermore, as noted earlier, a high sediment concentration layer just above the mud bed was another typical response observed in all the runs. This will be discussed later.

Spatially-averaged mud surface elevations are shown in Figs. 7-15a, b for all the six runs. For the kaolinite bed, the curves show severe erosion (corresponding to elevation lowering of about 1 cm and 0.5 cm) during the first half hour for Run 1 and Run 3 but only slight erosion (0.1 cm) for Run 2. This may have been because the build-up of erosion resistance at the surface layer required more than one week of consolidation as well as a difference in bed preparation (see Section 6.2, Chapter 6). The bed swelling phenomenon noted earlier was observed not only locally, see Fig. 7-2, but was also evident (e.g., Run 6 in Fig. 7-15) in terms of spatial average elevations, although not as significantly. The mud surface elevation in Fig. 7-15 also shows significant erosion (about 0.4 and 0.8 cm) during the second wave loading for Run 1 and Run 2, but not for Run 3.

Cedar Key mud, however, showed greater swelling, especially the more consolidated bed, Run 6. Run 4 also exhibited swelling but it occurred at the second, higher wave loading. Swelling may have been induced by shear deformation and soil structure reformation as discussed before.

The change in the spatially-averaged mud surface elevation with time relative to its original elevation, together with the mud density profile, can be used to calculate the mass of sediment eroded. For

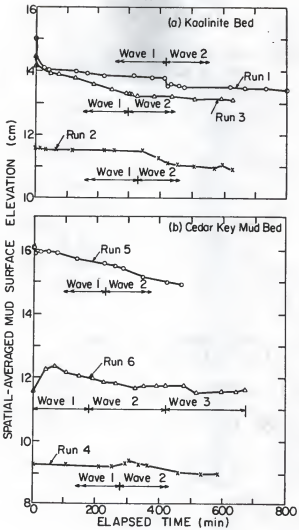


Fig. 7-15. Responses of the Spatially-Averaged Mud Surface Elevation. (a) Kaolinite Bed; (b) Cedar Key Mud Bed.

this purpose, the average value of bed density during erosion was selected, i.e., Eq. 7-1 and 7-2, and assumed to be applicable. The quantity thus obtained may be termed the wave-eroded sediment mass, M_p . During the bed swelling period, e.g., the first 70 minutes in Run 6, it was assumed that M_p from the mud surface elevation information was equal to M_n obtained from the suspended sediment sampling. The results for all six runs are presented in the next section.

7.3 Wave Erosion and Entrainment

7.3.1 Erosion

Figures 7-16a,b,c and 7-17a,b,c show the wave erosion and vertical entrainment behaviors for all six runs, in terms of the time-variation of the eroded sediment mass. All data indicate strong erosion but weak vertical entrainment. Here erosion is defined relative to the time-variation (increase) of M_p , the mass obtained by considering the lowering of the mud surface elevation. Entrainment is defined relative to M_n , the mass obtained by integration of the concentration data from the samplers. Thus M_p corresponds to the erosion of the bed while M_n corresponds to the upward entrainment of the near-bed high concentration layer of mass $M_p - M_n$. Thus, in what follows, the term erosion (or resuspension) will refer to bed scour and entrainment will imply the upward transport of the high concentration "fluid mud" layer just above the bed.

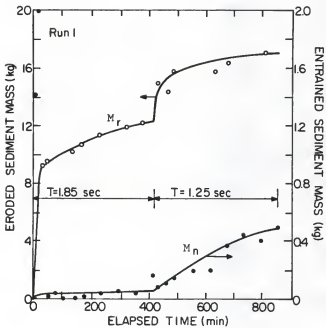


Fig. 7-16. Wave Erosion/Entrainment Behavior for Kaolinite.
 (a) Run 1.

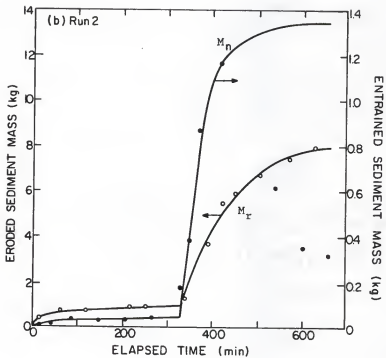


Fig. 7-16 (continued). (b) Run 2.

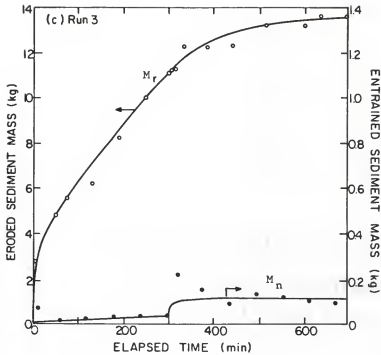


Fig. 7-16 (continued). (c) Run 3.

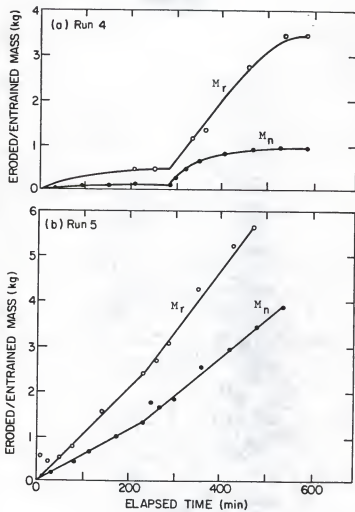


Fig. 7-17. Wave Erosion/Entrainment Behavior for Cedar Key Mud.
(a) Run 4; (b) Run 5.

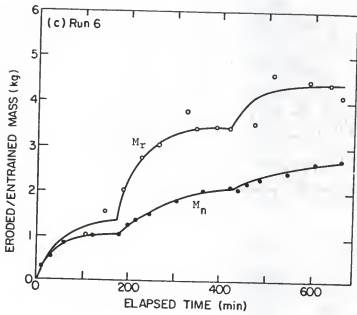


Fig. 7-17 (continued). (b) Run 6.

It is evident that in choosing these definitions a degree of arbitrariness has been introduced, or has become inherent, in the definitions of bed level, as well as the thickness of the near-bed layer. The bed level has been defined in this study in the visual sense, since the mud surface elevations were visually recorded. The upper level of the higher density layer has been identified as that above which the concentration dropped below 10 g/l. M_n is therefore not entirely coincident with the mass of sediment above this level, since the magnitude of M_n was dependent upon the elevation of the lowest sampler.

The average rates of erosion, $\bar{\epsilon}_r$, and of entrainment, $\bar{\epsilon}_n$ (M_r and M_n values, respectively, at the end of each wave loading divided by the duration of that wave loading) are given in Table 7-1. A significant difference between $\bar{\epsilon}_r$ and $\bar{\epsilon}_n$ is observed for the kaolinite bed. For Cedar Key mud, Run 4 exhibits differences from Run 5 and Run 6. This may be a result of the different composition of the mud material. See Section 6.3 in Chapter 6.

The following may be the reasons for the difference. First, as noted, it was difficult to obtain a complete profile of the suspended sediment, especially the high-concentration layer near the mud surface. Although only 5 to 10 mm in thickness, this part contributed significantly to the total suspended sediment mass. For example, 30 g/l in a 5 mm thick high concentration layer and 0.2 g/l in a 20 cm water layer above would correspond to a depth-averaged value of 0.95 g/l, which is about 5 times higher than 0.2 g/l if the lowest sampling tap did not receive a representative sample from the high concentration

layer. Therefore, a small deviation of the tap elevation could result in a significant error in the total suspended mass. Unfortunately, to obtain representative data for this layer was difficult because the appropriate tap elevation was not always easy to estimate.

Table 7-1. Average Erosion and Entrainment Rates

Run	$\bar{\epsilon}_r$ (mg/cm ² -min)	$\bar{\epsilon}_n$	$\bar{\epsilon}_r/\bar{\epsilon}_n$
1-1	0.774	0.038	20.4
2	0.312	0.029	10.9
2-1	0.078	0.003	23.6
2	0.571	0.107	5.3
3-1	1.000	0.003	303.0
2	0.175	0.006	31.3
4-1	0.046	0.012	4.0
2	0.268	0.074	3.6
5-1	0.283	0.156	1.8
2	0.366	0.219	1.7
6-1	0.227	0.152	1.5
2	0.207	0.109	1.9
3	0.105	0.074	1.4

Second, the use of Eq. 7-1, Eq. 7-2 and Fig. 7-15 to obtain M_p was a somewhat crude approach. The mud bed density changed not only with time, but also with location. The time dependence was caused by the deformation and reconstruction of sediment flocs as discussed before. The spatial (along the bed length) variation in the density profile was due to near-bed erosion, horizontal transport, settling and consolidation processes which occurred simultaneously. As noted previously, a part of the mud eroded at the upstream side was transported to the downstream side and settled there because the lower bed shear stress

there could not keep this sediment in suspension. Therefore, a spatially-averaged mud surface elevation actually represents the overall effect of the erosion, transport and settling processes. Thus, for instance, a net zero change of the mud surface elevation would not necessarily mean no local erosion. This phenomenon was further complicated by the swelling of the mud bed, especially at the upstream side. However, this crude estimation of M_r is a reasonable approach and does provide important information relative to erosion. This can be demonstrated by examining the values of M_r and M_n for Run 4 through Run 6 for Cedar Key mud. In these tests, the ratio, $M_r/M_n < 2$, because the low settling velocity (see Section 7.3.3) of the mud (composed with kaolinite) as well as the relatively higher R_w (see Section 4.5.3, Chapter 4) resulted in more efficient vertical entrainment. This observation implies that, in these cases, M_n was close to the total eroded sediment in comparison with the other cases.

Two types of erosion/entrainment behavior can be identified. The first type, in all but Run 5, showed a high erosion rate at the beginning, then decreasing with time before finally ceasing. This type of erosion process has been identified as that of a deposited bed in steady flow (Mehta *et al.*, 1982; Parchure and Mehta, 1985). The decreasing erosion rate is due to the downward increase of bed resistance against erosion, termed shear strength $\tau_s(z')$, of the mud bed, where z' is considered positive downward from the mud surface. Therefore, the excess shear stress, $\tau_e = \tau_b - \tau_s(z')$, where τ_b is the applied bed shear stress, decreases as $\tau_s(z')$ increases. Erosion ceases if $\tau_b \leq \tau_s$.

The second type of erosion/entrainment behavior is shown in Fig. 7-17b for Run 5. Here the time rates of erosion/entrainment were constants because of the linear relationships. This type of behavior has also been identified for a uniform bed under steady flow (Parchure and Mehta, 1985). Since a bed has a constant shear strength, i.e., $\tau_s(z') = \text{constant}$. Also τ_e would be close to a constant under each wave loading. Therefore, the erosion progressed at a constant rate because the erosion force was a constant. This process will not stop until all the material is eroded. The bed for Run 5 had only a 2-day consolidation period and therefore probably had a small and nearly uniform shear strength profile.

7.3.2. Erosion Rate

The erosion rate, ϵ_r , defined as the time rate of sediment erosion per unit bed area, is related to the excess shear stress, τ_e (Mehta, 1986). Parchure (1984) gave details for evaluating τ_e . Following his procedure, a relationship between τ_e and ϵ_r could be determined. Hereafter, all quantities noted are spatially-averaged except where otherwise indicated.

The shear strength profile, $\tau(z')$, of a mud bed was constructed first by knowing the time history of sediment mass eroded (shown in Fig. 7-16 and Fig. 7-17), the bed density profile (see Fig. 7-4, Eq. 7-1 and Eq. 7-2), the applied bed shear stress, τ_b , (presented in Table 4-2, Chapter 4) and a steady state of the erosion process. The given $\tau_b = \tau_{b1}$ must be equal to the mud shear strength τ_{s1} at steady state. Knowing the eroded mass at steady state and bed density profile allows

for the calculation of an elevation, z_1' , above which the sediment was eroded. Therefore, τ_{s1} was known at z_1' . For the next wave loading and the associated steady state, another τ_{s2} at the second elevation, z_2' , could be obtained. Here, for Run 1 through Run 4, two points were available for constructing the shear strength profile. See Fig. 7-18. For Run 6, three points were available.

Notice in Fig. 7-16c that the erosion process for Run 3-1 may not have reached a steady state. This was reflected by the large time-rate of the M_r curve. Therefore, the actual shear strength may have been lower than that shown in Fig. 7-18a. The shear strength exhibits a near-zero value for kaolinite in Run 1 and Run 3. It also shows a slow increase with depth in Runs 1, 3, and 6. The shape of the profile was different from that obtained under steady flow erosion tests (Parchure, 1984). An example of the latter type of profile is also given in Fig. 7-18b. A possible explanation would be that the mud oscillatory motion resulted in a reduction of erosion resistance during the process of erosion itself, especially near the mud surface, where the oscillatory motion was relatively large.

To examine the influence of the period of consolidation, T_{dc} , on erosion resistance, two strengths, τ_{so} (the erosion resistance at the mud surface) and $\bar{\tau}_s$ (the average erosion resistance for the top 5 mm of the mud bed), are shown in Fig. 7-19. For kaolinite bed, the erosion resistance at the mud surface is close to zero until $T_{dc} > 7$ days. The average strength of the top 5 mm mud is also small until $T_{dc} > 7$ days. For Cedar Key mud, because Run 4 and Run 6 had different clay composition (see section 6-3, Chapter 6), the erosion resistance can

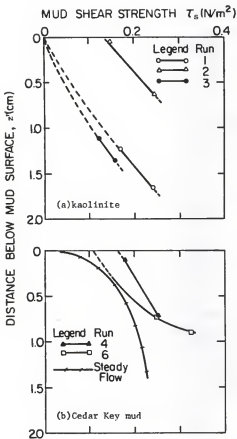


Fig. 7-18. Shear Strength Profiles for Resistance of Wave Erosion. (a) Kaolinite Bed; (b) Cedar Key Mud Bed.

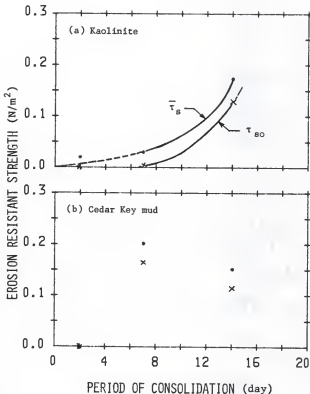


Fig. 7-19. Influence of the Period of Consolidation on Erosion Resistance. (a) Kaolinite; (b) Cedar Key Mud. Notice that the Cedar Key mud, which has 7-day consideration period, has different clay composition with the other two Cedar Key muds.

not be compared. However, a similar trend can be expected. This behavior is different from that observed with a steady flow erosion process in which the resistance increased relatively rapidly in the first day or two of consolidation and eventually approach a constant value with increasing consolidation (Parchure and Mehta, 1985). One major reason for the difference may be that the continuous oscillatory deformation reduced the erosion resistance of the top soil as discussed before.

For a given τ_b and measured eroded sediment mass at a given time, a corresponding elevation, z' , above which the sediment is eroded, can be obtained. The shear strength at z' , $\tau_s(z')$, can also be obtained from the shear strength profile through interpolation. Therefore, $\tau_e = \tau_b - \tau_s(z')$ is obtained. The corresponding erosion rate, ϵ_r , can be calculated from the M_r curve as the slope of the tangent drawn through the point on the M_r curve at the time of interest (Figs. 7-16 and 7-17), and with the given mud bed surface area of $800 \times 45.8 = 36640 \text{ cm}^2$.

Various correlations between ϵ_r and τ_e were tested, and a power law relationship between ϵ_r and non-dimensional excess shear stress, $\tau_e/\tau_s(z')$, gave the best linear relationship on a log-log plot. Figure 7-20 shows this relationship for each wave loading. Note that only Runs 1, 2, 3, 4 and 6 were evaluated in this way. Run 5 was considered separately, as noted previously. The erosion function has the form

$$\epsilon_r = \epsilon_0 \left[\frac{\tau_b}{\tau_s(z')} - 1 \right]^\alpha, \quad \tau_b > \tau_s(z') \quad (7-4)$$

with ϵ_0 and α given in Table 7-2. Notice that the values of α are

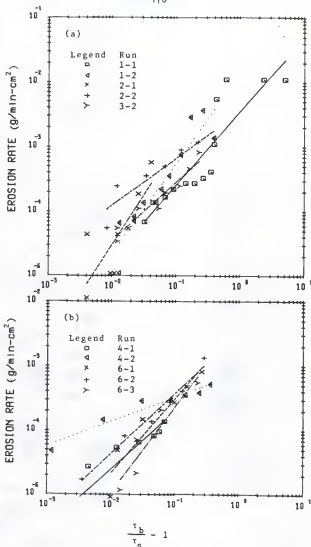


Fig. 7-20. Erosion Rate versus Dimensionless Excess Shear Stress.
 (a) Kaolinite; (b) Cedar Key Mud.

about the same, close to 1.0 except for Run 4-2 and Run 2-1. The proportionality constant, ϵ_0 , varied from 0.0008 to 0.0408. Equation 7-4 suggests a simple physical meaning: erosion can occur only when the bed shear stress is greater than the resistant shear strength, and that the erosion rate is proportional to the excess shear stress.

Table 7-2. Coefficients for the Erosion Function

Run	ϵ_0 (g/cm ² -min)	α
1-1	0.0035	1.1380
1-2	0.0139	1.4049
2-1	0.0408	1.5650
2-2	0.0035	0.7269
3-2	0.0023	0.9060
4-1	0.0016	0.9079
4-2	0.0008	0.3784
6-1	0.0044	1.1574
6-2	0.0033	0.9417
6-3	0.0050	1.3422

An effort to correlate the normalized erosion rate, ϵ_r/ϵ_0 , versus the dimensionless excess shear stress was made (not including Run 2-1 and Run 4-2), and the result is presented in Fig. 7-21. Equation 7-5 is the resulting equation obtained by using linear least squares regression through all the data points in Fig. 7-21:

$$\frac{\epsilon_r}{\epsilon_0} = 0.964 \left[\frac{\tau_b}{\tau_s(z')}^{-1} \right]^{1.08}$$

$$\approx \left[\frac{\tau_b}{\tau_s(z')}^{-1} \right], \quad \tau_b > \tau_s(z') \quad (7-5)$$

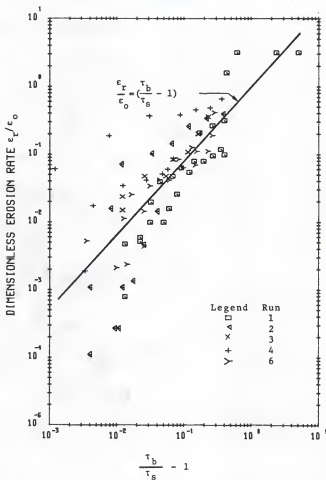


Fig. 7-21. Dimensionless Erosion Rate versus Dimensionless Excess Shear Stress.

Equation 7-5 suggests a nearly linear relationship between the normalized erosion rate and non-dimensional excess shear stress. However, this result is not applicable for all the experimental runs, and therefore, more studies are necessary to confirm this relationship.

For Run 5, the erosion rate was a constant and proportional to τ_b . Figure 7-22 shows the relationship. However, with just two data points it is not possible to evaluate the precise nature of dependence of the erosion rate on the bed shear stress.

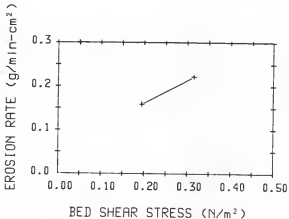


Fig. 7-22. Erosion Rate versus Bed Shear Stress, Run 5.

7.3.3 Entrainment

To further examine the vertical distribution of suspended sediment concentration, the three measured vertical concentration profiles in the test section were averaged to give the spatially-averaged concentration profile at steady state for each wave loading. The average distance from the mud surface to the lowest tap of the sediment sampler, $\langle \Delta h \rangle$, and the average of measured suspended sediment concentrations at the lowest tap, $\langle C_{T1} \rangle$, gave the lowest measured point on the concentration profile. The difference of $M_r - M_n$ together with $\langle \Delta h \rangle$, e.g., 12 mm in Run 3 at time = 680 minutes, gave the average sediment concentration between mud surface and the lowest tap. The maximum concentration of this high concentration layer was restricted to about 150 g/l. This is because a slurry has a concentration higher than this value may be considered as a bed rather than a fluid. Figure 7-23 gives the profiles from Run 1 to Run 6.

The data show steep gradients over the near-bed elevation which implies a weak upward entrainment process. The sediment could not go up efficiently. Basically two layers, a lower layer of about 2 cm thickness, and the fluid above, may be selected to examine the entrainment behavior under the experimental conditions. A 2 cm thickness was selected because most concentration profiles had a sharply decreasing sediment concentration at this elevation.

The maximum sediment concentration in the upper layer was on the order of 0.05 to 0.5 g/l. The nearly linear concentration profiles on a semi-log plot (see Fig. 7-23) suggested that a nearly constant

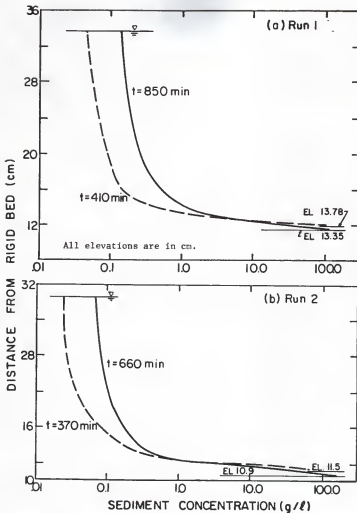


Fig. 7-23. Suspended Sediment Concentration Profiles at Steady State. (a) Run 1; (b) Run 2.

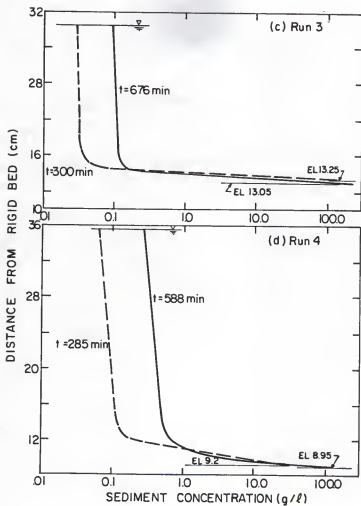


Fig. 7-23 (continued). (c) Run 3; (d) Run 4.

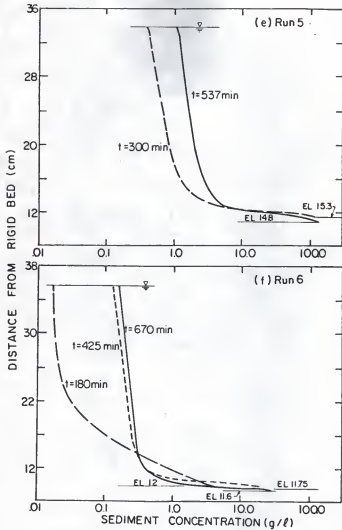


Fig. 7-23 (continued). (e) Run 5; (f) Run 6.

diffusion coefficient was quite likely. Consider the vertical 1-D sediment transport equation at equilibrium as

$$-w_s C = D_m \frac{dC}{dz} \quad (7-6)$$

where D_m is the diffusion coefficient to be estimated, C is the sediment concentration, dC/dz is the sediment concentration gradient, and w_s is the sediment settling velocity (which could also be a function of sediment concentration because of mutual interference between sediment particles). For kaolinite, the experimentally determined $w_s = C$ relationship, see Fig. 7-24, given by Lin and Lott (1986, personal communication) was used. For the Cedar Key mud, only one data point (1×10^{-5} m/sec at $C = 0.37$ g/l) was available. This value indicates that w_s for Cedar Key mud was an order of magnitude lower than that for kaolinite. Also, w_s from other estuarial mud (Mehta, 1986) showed significant low settling velocity (as much as two orders of magnitude less than that for kaolinite). Here it is assumed that w_s for Cedar Key mud follows Krone's (1962) formulation for San Francisco Bay mud (the exponent is $4/3$, but the proportionality constant is calibrated against the available value noted):

$$w_s = 0.000037 C^{4/3} \quad (7-7)$$

where C is in units of g/l and w_s is in m/sec. With these data, D_m was determined, based on Eq. 7-6 and Fig. 7-23. The results are presented in Table 7-3. The estimated diffusion coefficients have values on the order of 10^{-5} m²/sec. These values are about 10 times higher than the molecular viscosity. As noted earlier in Chapter 4, these values are

Table 7-3. Measured Diffusion Coefficient
in the Upper Layer

Run	w_s ($\times 10^{-5}$ m/sec)	D_m ($\times 10^{-6}$ m 2 /sec)
1-1	4.5	8
2	8.4	16
2-1	2.3	5
2	4.5	12
3-1*	-	-
2	5.1	39
4-1	1.0	4
2	5.0	10
5-1*	-	-
2*	-	-
6-1	0.6	2
2	3.8	9
3	4.8	15

* In these runs a steady state was not attained.

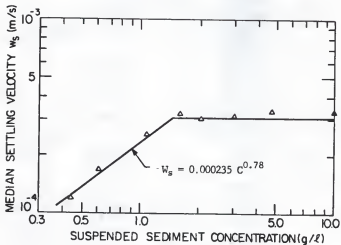


Fig. 7-24. Settling Velocity versus Sediment Concentration for Kaolinite.

important for sediment motion in the present case but have little contribution to the velocity distribution, except within the thin, near-bed wave boundary layer.

In the near-bed layer, the concentration was significantly higher, on the order of 30 g/l, compared to 0.2 g/l in the upper layer. The sediment concentration gradient was also high, on the order of 3000 g/l-m, compared to 1 g/l-m above. However, w_s (about 0.1 mm/sec) did not increase much because the high concentration hindered the upward flux of water resulting from sediment settling (Krone, 1962). This gave an estimated vertical diffusion coefficient on the order of $1 \times 10^{-6} \text{ m}^2/\text{s}$, which is about the same as the kinematic viscosity of water. This result implies that viscous effects were dominant in the high concentration layer. Dye diffusion tests discussed in the next section corroborated this observation.

Figure 7-25 shows another interesting phenomenon. The suspended sediment concentration was typically higher at the beginning of each wave loading. Note the peaks of sediment concentration in Fig. 7-25b. The concentration decreased later. This type of response can only be due to a reduction of erosion at the mud surface, because $\langle \Delta h \rangle$ was nearly invariant. See Fig. 7-25a. This phenomenon may be interpreted as follows. As a result of mass erosion (a rapid resuspension of large quantities of sediment) at the onset of wave loading, the sediment mass eroded exceeded the entraining ability of the waves. Therefore, the sediment concentration at the nearbed zone increased drastically, producing a peak. As the erosion and entrainment process continued, mass erosion was replaced by particle-by-particle erosion, which is

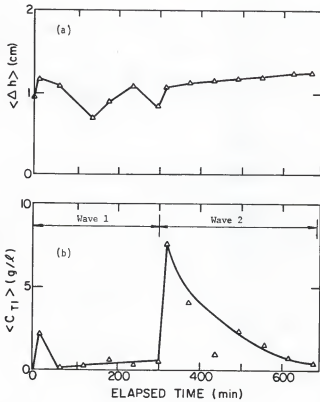


Fig. 7-25. Spatially-Averaged Variation of (a) the Distance between the Lowest Tap and Mud Surface; (b) Sediment Concentration at the Lowest Tap.

typically lower than mass erosion and is controlled by the depth-increasing shear strength, τ_s . Meanwhile, the entrainment ability remained the same because it depends on the wave characteristics only. Therefore, the near-bed concentration decreased due to the lesser supply of sediment mass.

7.4 Dye Diffusion Tests

In Chapter 2, two types of wave diffusivity profiles were mentioned but it is not clear which one was closer to reality, as far as the present experiments were concerned. Therefore, three dye studies were performed in the flume.

The first test was performed with clear water and a rigid smooth bed made of plexiglass. The water depth was 20 cm and wave period and height were 1.2 sec and 7 cm, respectively. The wave Reynolds number, $R_w = 6950$, indicated that there was a viscous sub-layer above the bed with a thickness $\delta_L = \sqrt{v/2\sigma} = 1$ mm (Dean and Dalrymple, 1984). The dye, Rhodamine, was injected into the water column by slowly moving the injecting syringe up and squeezing the dye out simultaneously to generate a vertical line source. The wave maker was then turned on and pictures were taken from the side wall. Figure 7-26 shows the trajectory and the relative size of the dye parcel at selected times after wave generation. It is noticed that the dye showed a relatively rapid longitudinal spreading near the bed. A thin layer could be seen clearly. This layer, about 3 to 5 mm in thickness, was about 5 times thicker than δ_L . Above this layer, the dye spread at almost the same slow rate, except near the water surface, where about 3 times greater

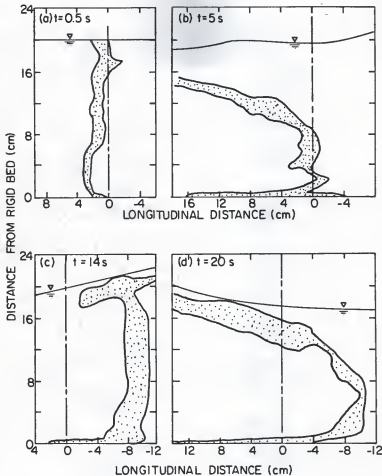


Fig. 7-26. Diffusion of a Line-Source Dye in the Wave Flow with $T = 1.2\text{ s}$, $H = 7\text{ cm}$. (a) $t = 0.5\text{ s}$; (b) $t = 5\text{ s}$; (c) $t = 14\text{ s}$; (d) $t = 20\text{ s}$.

spreading rate was observed. The rapid longitudinal spreading was because the wave velocity profile had the greatest velocity gradient near the bed, and resulted in a high longitudinal dispersion. However, because the wave Reynolds number $R_w < 10^4$, there was little turbulence within δ_L , and therefore the vertical diffusion was small, principally by molecular diffusion. The dye within this viscous sublayer was nearly uniform in concentration in the longitudinal direction, and, furthermore, vertical molecular diffusion made the dyed layer much thicker than δ_L .

Based on this observation, it can be concluded that for clear water and a rigid smooth bed, the horizontal diffusion coefficient would be highest near the bed, decrease when moving outside the near-bed layer, and then increase upward at a relatively slow rate due to a small velocity gradient. The vertical turbulent diffusion coefficient was nil in the viscous sub-layer and increased upward. However, it increased at a relative slow rate except near the water surface.

A second test was conducted with sediment-laden water during Run 2-2 with $R_w = 3060$. This had a similar wave condition as in the first test. Dye was injected just above the mud surface. It spread quickly in the longitudinal direction and moved downstream slowly, with little vertical spreading. The dye spread horizontally, above the mud bed, over a 65 cm reach but vertically only about 2 cm in 4 minutes. A wave-induced net downstream current was believed to have been the cause of the downstream net transport. The 2 cm thickness was about 20 times thicker than δ_L . A likely reason could be that the mud bed was not rigid. The vertical oscillation of the mud surface, although small,

resulted in vertical convective transport of the dye, thus resulting in a thicker layer.

The third test was also conducted with sediment-laden water during Run 5-2. In addition to injection of dye just above the mud surface, dye was also injected at the middle elevation of the upper layer as a point source. The dye just above the mud surface displayed a similar behavior to that in Run 2-2. The dye at the middle elevation showed an elliptic trajectory and gradual diffusion of the dye parcel similar to that shown in the first test.

These tests, under the condition $R_w < 10^4$, demonstrated that the apparent diffusion (result of the molecular diffusion, turbulent diffusion and dispersion) coefficient in the vertical direction had the lowest value just above the mud bed. The coefficient increased upward slowly and had a maximum value near the free surface. The slow, uniform rate of dye parcel spreading over depth indicated that a constant diffusion coefficient could be acceptable. For the transport in the longitudinal direction, the apparent diffusion coefficient was the highest near the bed, decreased rapidly above the viscous wave boundary layer to a minimum, and then increased slowly similar to the vertical apparent diffusion coefficient.

7.5 Concluding Comments

Nielsen (1978) showed that the forces in an oscillatory flow erosion process are similar to that for a steady flow erosion process. The minor difference is the existence of an inertia force, which comes

from the unsteady motion and the added mass. He demonstrated that the inertia force is less than 5% of the total force, and is, therefore, negligible. This observation provides a common basis to compare the erosion function for these two types of flow.

Parchure and Mehta (1985) gave an erosion function applicable to a range of cohesive sediments which is

$$\epsilon_r = \epsilon_f \exp[a_0(\tau_b - \tau_s)^{1/2}], \quad \tau_b > \tau_s \quad (7-8)$$

where ϵ_f and a_0 are two constants characteristic of each sediment bed. Values of a_0 and ϵ_f are given in Table 7-4.

Given $\tau_b = 0.22 \text{ N/m}^2$ and $\tau_s = 0.2 \text{ N/m}^2$, $\tau_e/\tau_s = 0.1$ and from Fig. 7-20 ϵ_r varies from $0.0008 - 0.00025 \text{ g/min}\cdot\text{cm}^2$. The same τ_b , τ_s values for a steady erosion process give ϵ_r ranging from 0.000001 to $0.00022 \text{ g/min}\cdot\text{cm}^2$ (see Table 7-4). The erosion rate from wave flow is thus about five times higher than that from steady flow. Another example with $\tau_b = 0.4 \text{ N/m}^2$, $\tau_s = 0.2 \text{ N/m}^2$, $\tau_e = 0.2 \text{ N/m}^2$, and $\tau_e/\tau_s = 1.0$ yields ϵ_r from 0.001 to $0.01 \text{ g/min}\cdot\text{cm}^2$. For steady erosion process, the same loading yields quite different results. See Table 7-4. For kaolinite, these two erosion processes have about the same rate. For natural mud, wave erosion rate is still much higher than the steady flow erosion process. This result demonstrates the great significance of wave erosion in water bodies subject to waves (and currents), especially at small excess shear stress. However sometimes, significant erosion is not easily detected because of the low upward entrainment of eroded sediment which remains near the bed.

Table 7-4. Constants for Steady Flow Erosion Function
(after Parchure and Mehta, 1985)

sediment	$c_f \times 10^5$	α_0	ϵ_r^*	ϵ_r^{**}
	g/cm ² min	m/N ^{1/2}	g/cm ² min	
Kaolinite T	0.5	18.4	0.000067	0.018
Kaolinite S	1.4	17.2	0.000160	0.030
Lake mud	3.2	13.6	0.000220	0.014
Bay mud	0.04	8.3	0.000001	0.000016
Lake mud	0.42	8.3	0.000014	0.00017
Estuarial mud	1.86	4.2	0.000033	0.00012
Kaolinite	0.6	25.6	0.000220	0.56

* for $\tau_e = 0.02 \text{ N/m}^2$

** for $\tau_e = 0.2 \text{ N/m}^2$

The ability of waves to reduce mud shear strength may explain why waves have a stronger erosion-generating ability than steady flows. However, further studies are required to confirm this conclusion.

The estimation of the eroded mass, M_r , on an approximate basis gave important information on how much sediment mass was actually eroded. Although a more precise determination of M_r would be desirable, it may require much greater experimental effort. However, the closeness of the M_r and M_n curves from Run 4 through Run 6 suggests that this crude estimation of M_r curve should be acceptable. The main difference in M_r and M_n values for kaolinite may arise from the weak entraining force and relatively high settling velocity of kaolinite. These two factors enhanced the relative importance of the near-bed high concentration layer, and resulted in a large error in estimating M_n .

The calculation of the interfacial shear stress, τ_b , was based on the assumption that the suspended sediment concentration was low, and that the viscosity of water remained unchanged. However, actual

sediment concentration in the near-bed layer can easily exceed 10 g/l. Hence, the change in kinematic properties was not always negligible. Also a significant and continuous change in mud properties near the mud surface (1 cm) may be important. Although it is not always easy to identify these properties and property changes in such a small thickness under a complicated dynamic environment, further effort in this area should be made.

Only skin friction (at the interface) was essentially considered. The originally smooth mud surface may have become somewhat roughened under erosion because of the spatial variability in the erosion process. Also, the possibility of shear failure due to pressure difference on a non-smooth mud surface was not considered.

The large eddy viscosities found in wave flows over rippled sandy beds is mainly because of the periodic generation and release of vortices. Bagnold (1946) gave a clear description of this phenomenon. Vortices are generated because the ripples are relatively fixed in the bed. However, in the present case, the up and down motion of the mud surface, whether it was in phase or out of phase with the free surface profile, was a part of the dynamic system. The interfacial wave moved with the same speed as the free surface wave. Therefore, vortices (of the size of water particle excursion distance $2a_0$) probably did not contribute significantly to the bed shear stress through form drag.

Vertical sediment entrainment near the mud surface was comparatively weak because of the existence of a viscous sub-layer since in all tests, $R_w < 10^4$. For a turbulent wave boundary, $R_w > 1.2 \times 10^4$, the vertical diffusion coefficient at the mud surface would increase

significantly. Hence, the vertical transport near the bed would be much more efficient.

On a rippled sandy bed, the release of vortices also provides an important vertical transport mechanism. Sand particles, having been swept into the vortex, tend to get trapped and move with the vortex (Nielsen 1984). Possible localized small vortices over the bed might also have contributed to vertical diffusion near the bed.

In summary, local small vortices, the vertical oscillation of the mud surface, the high longitudinal dispersion, the wave induced current, and low vertical entraining potential of waves in the near-bed layer appear to be the reasons for the occurrence of a high concentration layer above bed.

CHAPTER 8
SUMMARY, CONCLUSIONS AND RECOMMENDATIONS

8.1 Summary and Conclusions

High turbidity caused by waves and significant wave damping are the two important phenomena observed in muddy coasts. Mathematical models were developed to simulate the hydrodynamics of wave-mud systems. Laboratory experiments were conducted to verify wave-mud interaction, to investigate the wave erosion potential, and to observe sediment entrainment behavior.

In choosing a constitutive model for mathematical modeling, viscoelastic behavior was selected rather than two other possible behaviors: viscous fluid and Bingham fluid. The reasons are as follows:

1. Mud velocities predicted by using the viscous fluid model indicated that wave-induced mud movement would be about the same as that in the water. However, measured mud motion amplitudes were typically much smaller than water velocity amplitudes.
2. Measured mud movement did not show the quiescence-moving-quiescence behavior expected from a Bingham fluid. On the contrary, some movement was always present, even at very low wave loading.

A 1-D Bingham fluid model and a 2-D viscoelastic (hydrodynamic) model were developed and their response under waves was evaluated.

The 1-D Bingham fluid model was developed first. The model-predicted wave-induced bed shear stresses were typically lower than the yield strength of mud. Therefore, for such cases the model predicted no mud motion at all and also very small wave damping. However, the experimental results showed a high degree of wave decay, which indicated that the 1-D model was inadequate. Ignoring the momentum transferred across the mud surface by pressure was a major reason why this model did not succeed.

In the 2-D model it was assumed the water layer has a constant viscosity, while the mud has simple, linear viscoelastic properties characterized by the Voigt element. The turbulence in the water layer was only considered with regard to the determination of the bed shear stress. Depth-variations of mud properties were simulated by dividing the mud bed into layers. The model demonstrated that the predicted wave attenuation coefficients were in agreement with the measurements. The predicted velocities of water and mud showed acceptable agreement with the observed data, while the measured dynamic pressure generally had greater magnitudes than predicted.

Given the experimental wave conditions (wave Reynolds Number $R_w \leq 1.2 \times 10^4$), the predicted water-mud interfacial bed shear stresses were, in general, larger than the bed shear stresses calculated by assuming a rigid bed. This was due to the opposite relative motions of mud and water. The velocity gradient was increased by this opposite motion. For Run 5, the softest bed, the model predicted a smaller bed shear stress due to the high fluidity of the mud.

For $R_w > 1.2 \times 10^4$, a constant eddy viscosity, ϵ , was selected to estimate the bed shear stress for the soft mud bed. Selecting a high value of shear modulus for the mud bed, the model could simulate the wave flow over rigid bed. Matching the predicted bed shear stress with that calculated from the rigid bed wave friction factor concept (Eq. 2-7) gave a value of the total viscosity ν_{e1} ; therefore, $\epsilon = \nu_{e1} - \nu_1$, where ν_1 is the kinematic viscosity of water, could be estimated and assumed applicable for soft (movable) beds. Here ϵ served only as a parameter to obtain the bed shear stress. Eddy viscosity is not important with regard to wave mechanics outside the wave boundary layer. However, it is important for sediment entrainment.

The Voigt model was selected from two possible simple, linear viscoelastic behaviors for modeling mud bed response. Relaxation tests were performed by using a viscometer and other auxiliary equipment. The muds did not exhibit creep phenomenon characteristic of the Maxwell model, the other possible option, but instead showed the ability to resist a shear force and also showed reasonably linear response for small strain. Therefore, the Voigt model was selected. The same equipment was also used to obtain the shear modulus G and the viscosity μ for the muds (Voigt material). Although the viscometer was not designed to measure these viscoelastic constants, the data obtained (based on average response) showed satisfactory results when used in the 2-D model.

Correlations between G , μ , and dry mud density provided an easy way to obtain G and μ . The shear modulus increased with mud density. However, μ decreased with mud density except in Run 5. In the visco-

elastic model, μ serves as an index of internal friction loss. It has somewhat different physical meaning than the viscosity of an Newtonian fluid. Therefore, a dense mud has a lower viscosity because of the lesser mobility than a soft mud. In the future the resonance behavior characteristic of viscoelastic materials may provide another approach for measuring the material constants, G and μ .

Flume experiments showed a significant potential for erosion of soft muds. Kaolinite and Cedar Key (Florida) mud were the two materials selected for testing. Tap water was the eroding fluid in which the sediments were in a state of flocculation. The sediments were equilibrated in the (eroding) fluid prior to the tests. Three consolidation periods, 2 days, 1 week, and 2 weeks, were chosen.

A photo-sensing light meter developed to detect the instantaneous suspended sediment response during erosion yielded encouraging results. Sometimes two peak concentrations were found in a wave period for kaolinite bed. These two peaks did not occur regularly and might be induced by the release of local small vortices when the wave flow changed direction. Data of the instantaneous sediment concentration showed strong fluctuation near the mud bed. This fluctuation decreased rapidly with increasing elevation away from the mud bed. At 11 cm above the bed, the sediment concentration data showed almost no fluctuation but a slowly (\gg wave period) increasing time-averaged sediment concentration. Time-averaged output voltage from the light meter also gave the corresponding time-averaged sediment concentration. The meter requires further modifications to insure a wider operating range.

The total pressure response in the mud bed showed an interesting behavior. The deformation/reconstruction of floes in the bed had a strong effect on the dynamic pressure fluctuations. The maximum increment of the apparent bulk density obtained from the change of pressure difference between two elevations was as much as 30% higher than the initial value. The change of void ratio in a sandy bed caused by seismic loading can be used as an analogy to interpret this type pressure response. For cohesive sediment, the change of floc structure could also have contributed.

Bed density varied during the erosion process. Typically it decreased at the beginning and increased later. A local maximum density variation of about 60% occurred in Run 4. See Appendix D. The maximum depth-averaged variation of about 15% occurred in Run 3.

Suspended sediment concentration profiles (obtained by water sample withdrawal method) exhibited a strong gradient in a near-bed zone about 2 cm in thickness. A fluid mud layer, defined as zone of sediment concentration greater than 10 g/l, was observed in all the experimental runs. The thickness of this layer varied from about 0.2 to 1.5 cm. Sediment concentration mass in this layer was the major contributor to the total suspended sediment mass. This layer can alter the hydrodynamic behavior (e.g., reduce the turbulence, increase the kinematic viscosity) provided the sediment concentration is high enough. The depth-averaged sediment concentrations also showed a longitudinal gradient in the test section. This necessitated the calculation of the suspended mass based on samples from several sampling locations. The suspended sediment mass, M_n , obtained from these

samples was considered to be the mass resulting from the upward entrainment of the near-bed high concentration (fluid mud) layer.

The eroded sediment mass, M_r , was estimated from the time-variation of the mud surface elevation together with the bed density profile. The results obtained by this approach, although rough, well reflected the wave erosion ability. The ratio $M_r/M_n < 2$ for the Cedar Key mud indicated that the method of evaluating M_r was acceptable. The high ratio of M_r/M_n (up to 150) for kaolinite might have been due to the high settling velocity of this sediment as well as relatively weak upward wave entraining ability which made the high concentration mud layer predominantly important in calculating M_n .

Two types of sediment erosion and entrainment behavior were observed similar to those which have been identified in a steady flow erosion process: the deposited bed behavior and the placed bed behavior. The first one shows a high erosion rate at the beginning, but the rate decreases with time as the process continues. This type of behavior has been interpreted to mean that the excess shear stress, $\tau_e = \tau_b - \tau_s(z')$, decreases with depth. The erosion process stops when $\tau_e \leq 0$. A power-law relationship between the rate of erosion and the non-dimensional excess shear stress was obtained as

$$\epsilon_r(z') = \epsilon_0 \left[\frac{\tau_b}{\tau_s(z')} - 1 \right]^\alpha, \quad \tau_b > \tau_s(z') \quad (8-1)$$

with an average $\epsilon_0 = 0.008$ (range 0.0008 to 0.04) g/min-cm² and $\alpha = 1.05$ (range 0.38 to 1.57). Since α was so close to one, a simple, linear relationship may be suggested:

$$\epsilon_r(z') = \epsilon_0 \left[\frac{\tau_b}{\tau_s(z')} - 1 \right], \quad \tau_b > \tau_s(z') \quad (8-2)$$

This is an empirical equation based on the (deterministic) approach presented in Chapter 6 and Chapter 7. It has a simple physical meaning: erosion occurs only when the bed shear stress is greater than the resistant shear strength. The erosion constant, ϵ_0 , has different values for different sediments and consolidation periods. The ratio of maximum ϵ_0 to minimum ϵ_0 is about 50. This ratio is much smaller than that for the erosion process under steady flows (about 200, Parchure and Mehta, 1985).

The second type of erosion showed a constant rate. One possible reason for this behavior might be the small, uniform shear strength profile in the mud bed. Therefore, the result was a near constant τ_e at any bed elevation and constant rate of erosion. No rate expression has been proposed for this type of erosion because of limited data.

Comparison of typical erosion rates under steady flow with those due to waves suggest that waves have more power to erode the sediment, especially at small excess shear stress. In the example considered, ϵ_r for waves was found to be approximately 5 times higher, on the average, than that for a steady flow with the same τ_e .

Continued oscillatory motion in the bed caused by wave force results in a decrease of the mechanical shear strength as well as the resistance against erosion. This is believed to be an important factor contributing to the observed difference in the erosion potential between waves and steady flow.

Under the experimental conditions, $R_w < 1.2 \times 10^4$, the upward sediment entrainment rate was low. The main reason seemed to be the existence of a viscous sub-layer above the bed. Vertical diffusion in

this layer was controlled by the molecular diffusion process and the small convective transport provided by the vertical oscillatory motion of mud surface.

The large velocity gradient in the near-bed boundary layer resulted in a correspondingly large longitudinal dispersion. This high dispersion, wave induced current, and the low upward diffusion in this layer were the reason for the occurrence of the high concentration fluid mud layer.

At steady state, a linear relationship for the suspended sediment concentration versus depth plotted on semi-log coordinates suggested the existence of a constant diffusion coefficient, D_m , in the water column above the high concentration layer. An estimation procedure gave $D_m = 10^{-5}$ m²/sec under the experimental conditions. Based on the discussion presented above, a profile having two constant diffusion coefficients may be suggested in simulating the upward entrainment of sediment in a wave entrainment process under the condition $R_w \leq 1.2 \times 10^4$.

8.2 Recommendations for Further Study

Solving the 2-D equations of motion using the Bingham fluid model would provide the most direct evidence as to whether the Bingham model, or a more sophisticated model (Chen, 1985), is applicable for simulating wave-mud dynamics. However, to solve the nonlinear equations of motion analytically may prove to be quite difficult. The numerical approach, on the other hand, would face the free surface problem and unknown downstream boundary conditions. Harlow and Welch (1965)

developed a technique (Marker-and-Cell method) to solve the free surface problem. Chen et al., (1969) modified Harlow's free surface boundary conditions and solved the reflection problem of a solitary wave propagating in a 2-D wave flume, which had vertical walls at both ends. They all used a constant density and a high artificial viscosity. The use of high artificial viscosity was necessary to avoid numerical instability. However, to simulate the bed shear stress, the true viscosity value must be used. A better scheme to overcome the instability problem will require additional effort.

The linearized multi-layered hydrodynamic model developed here employs the Taylor expansion technique and selects only the first harmonic terms in the simulation of wave-mud interaction. This treatment restricts the model to consideration of small amplitude waves. However, some of the applications of this model are really not within the range of small amplitude waves. To encompass the entire study domain, consideration of wave non-linearity is quite important.

Measurement of mud motion would provide the most direct evidence to verify the model. This might be done by placing a small accelerometer in the mud bed to record the acceleration instead of velocity.

An instrument which provides torque reading (like the torque pointer in a Brookfield viscometer) and constant vane speed is suggested for the measurement of viscoelastic constants. The measurement of these constants near the mud surface is another difficult but important task which will require more effort. The correlation of G , μ and dry density of mud also needs further scrutiny.

To understand possible pore pressure effects, pore pressure measurements in the bed are suggested. Effort to include a formulation for pore pressure influence in the governing equations would be essential if the measured pore pressures are found to be significant.

The photo-sensing light meter showed encouraging results for the measurement of instantaneous as well as the time-averaged sediment concentrations. This device can also save a great deal of time currently required by the gravimetric method. Therefore, it is strongly recommended that further improvements on the performance of this device be made.

The effects of a turbulent wave boundary layer were not considered in this study. However, turbulent boundary layers commonly occur in the prototype. For this reason, experiments which cover the range of $R_w > 1.2 \times 10^4$ are suggested. The larger R_w means a larger bed shear stress and stronger turbulence. This makes it possible to study the erosion behavior at high excess shear stresses, and to provide complete laboratory data for the wave erosion process. The influences of other parameters (salinity, different compositions of clay material, organisms, temperature of the eroding fluid, etc) which have measurable influence on bed resistance should be evaluated.

APPENDIX A
BOUNDARY CONDITIONS FOR THE MULTI-LAYERED MODEL

Details of the boundary conditions and the content of each term in the coefficient matrix c are given here, although only $c_{1,1}$ through $c_{2,3}$ are given explicitly as examples.

A.1 Equations for Vertical Velocities and Pressures

The differential equations for vertical velocities and pressure amplitudes were given in Chapter 4 and are repeated here for clarity:

$$\hat{w}_1''' = (k^2 + \lambda_1^2) \hat{w}_1'' + k^2 \lambda_1^2 \hat{w}_1' = 0 \quad (A-1)$$

$$\hat{p}_1 = \left(\frac{\mu_1}{k^2} \right) [\hat{w}_1''' - \hat{w}_1'' \lambda_1^2] \quad (A-2)$$

where k is the complex wave number, $\lambda_1^2 = k^2 - j\sigma v_{el}^{-1}$ and $j = \sqrt{-1}$. The forms of solutions are chosen as

$$\hat{w}_1(z) = A_1 \sinh Z_1 + B_1 \cosh Z_1 + C_1 e^{\lambda_1 z} + D_1 e^{-\lambda_1(z+d_1)} \quad (A-3a)$$

$$\hat{w}_1(z) = A_1 \sinh Z_1 + B_1 \cosh Z_1 + C_1 \sinh N_1 + D_1 \cosh N_1 \quad (A-3b)$$

with $i = 2, 3, \dots, N$. Here, $Z_i = k(d_1 + d_2 + \dots + d_i + z)$ and $N_i = \lambda_1(d_1 + d_2 + \dots + d_i + z)$. The reason that there are two different forms of \hat{w} is that λ_1 is a large number and represents the viscosity-dominated flow in the vicinity of the boundary. Away from the boundary, the viscous

terms are negligible ($c_1 = 0$). Therefore, Eq. A-3a was chosen. Another advantage of Eq. A-3a is that it avoids numerical overflow problems in the computer program.

A.2 Zero Normal Stress at the Free Surface

The zero normal stress at the free surface, n , a priori unknown elevation, is approximated by using Taylor expansion at the mean water level, $z = 0$:

$$\begin{aligned}\sigma_1(x, n, t) &= \sigma_1(x, 0, t) + n \frac{\partial \sigma_1}{\partial z}(x, 0, t) + \dots \\ &= p_1(x, 0, t) + 2\mu_1 \frac{\partial w_1}{\partial z} \Big|_{z=0} + \\ &\quad n \left[\frac{\partial p_1}{\partial z} - p_1 g - 2\mu_1 \frac{\partial^2 w_1}{\partial z^2} \right]_{z=0} + \dots \\ &= [\hat{p}_1 - 2\mu_1 \hat{w}_1' - p_1 g a_0] e^{j(kx - \omega t)} = 0 \quad (\text{A-4})\end{aligned}$$

here only the basic harmonic term is selected. All higher harmonic terms are neglected. Substituting for \hat{p}_1 and \hat{w}_1' from Eq. A-2 and A-3 yields

$$M_1(A_1 \cosh kd_1 + B_1 \sinh kd_1) - \cancel{\frac{p_1}{k}} = p_1 g a_0 \quad (\text{A-5})$$

where $M_i = \frac{j p_1 \sigma}{k} = 2\mu_1 k$, with $i = 1, 2, \dots, N$.

A.3 Linearized Kinematic Free Surface Boundary Condition

According to this condition, $w = \partial n / \partial t$ at $z = 0$. Substituting for w and n gives

$$A_1 \sinh kd_1 + B_1 \cosh kd_1 + C_1 = -j \omega a_0 \quad (\text{A-6})$$

Equations A-5 and A-6 are combined to eliminate the a_0 term. The result is Eq. A-7 (Eq. 4-13):

$$c_{1,1} A_1 + c_{1,2} B_1 + c_{1,3} C_1 = 0 \quad (\text{A-7})$$

where $c_{1,1} = \frac{M_1}{\rho_1 g} \cosh kd_1 - \frac{j}{\sigma} \sinh kd_1$

$$c_{1,2} = \frac{M_1}{\rho_1 g} \sinh kd_1 - \frac{j}{\sigma} \cosh kd_1$$

$$c_{1,3} = -\frac{2v_{e1}\lambda_1}{\rho_1 g} - \frac{j}{\sigma}$$

A.4 Zero Shear Stress at the Free Surface

The condition of zero shear stress at the free water surface, similar to the zero normal stress, is also obtained by using Taylor series expansion about the mean water level, $z = 0$. This is given as

$$\begin{aligned} \tau_1(x, n, t) &= \tau_1(x, 0, t) + n \frac{\partial}{\partial z} \tau_1(x, 0, t) + \dots \\ &= u_1 \left(\frac{\partial u_1}{\partial z} + \frac{\partial w_1}{\partial x} \right) \Big|_{z=0} + n \frac{\partial}{\partial z} [u_1 \left(\frac{\partial u_1}{\partial z} + \frac{\partial w_1}{\partial x} \right)] \Big|_{z=0} + \dots \\ &= u_1 \left(\frac{j}{k} \hat{w}_1'' + jk \hat{w}_1' \right) \Big|_{z=0} e^{j(kx-\sigma t)} = 0 \end{aligned} \quad (\text{A-8})$$

Here as well the basic harmonic term is selected. Substituting for the velocity term (Eq. A-3), Eq. A-9 (Eq. 4-14) is obtained:

$$c_{2,1} A_1 + c_{2,2} B_1 + c_{2,3} C_1 = 0 \quad (\text{A-9})$$

with

$$c_{2,1} = 2k^2 \sinh kd_1$$

$$c_{2,2} = 2k^2 \cosh kd_1$$

$$c_{2,3} = (\lambda_1^2 + k^2)$$

A.5 Matched Horizontal Velocity Conditions

This condition implies that $u_i(x, \xi_i, t) = u_L(x, \xi_i, t)$ for $i = 1$ to $N-1$, with $L = i+1$. Taylor expansion at the mean interface elevation, $\hat{w}_i(-\sum d_i)$, is used to obtain an approximate solution. From the upper layers, the horizontal velocities are

$$\begin{aligned} u_i(x, \xi_i, t) &= u_i(x, -\sum d_i, t) + \xi_i u'_i(x, -\sum d_i, t) + \dots \\ &\approx u_i(x, -\sum d_i, t) + \hat{w}'_i(-\sum d_i) e^{j(kx - \omega t)} \\ &= \frac{j}{k} \hat{w}'_i(-\sum d_i) e^{j(kx - \omega t)} \end{aligned} \quad (A-10a)$$

From the lower layers, the horizontal velocities are

$$\begin{aligned} u_L(x, \xi_i, t) &= u_L(x, -\sum d_i, t) + \xi_i u'_L(x, -\sum d_i, t) + \dots \\ &= \frac{j}{k} \hat{w}'_L(-\sum d_i) e^{j(kx - \omega t)} \end{aligned} \quad (A-10b)$$

The matching conditions are $\hat{w}'_i(-\sum d_i) = \hat{w}'_L(-\sum d_i)$. For the first interface, i.e. between the water and the first mud layer, this condition gives

$$\begin{aligned} k A_1 - \lambda_1 D_1 - k \cosh \lambda_1 d_1 &= A_2 - k \sinh \lambda_1 d_1, \\ B_2 - \lambda_2 \cosh \lambda_2 d_1 &= C_2 - \lambda_2 \sinh \lambda_2 d_1, \\ D_2 &= 0 \end{aligned} \quad (A-10c)$$

For the other mud to mud interfaces, $i=2, n-1$, this condition gives

$$\begin{aligned} k A_i + \lambda_i C_i - k \cosh \lambda_i d_L &= A_L - k \sinh \lambda_i d_L, \\ B_L - \lambda_L \cosh \lambda_L d_L &= C_L - \lambda_L \sinh \lambda_L d_L, \\ D_L &= 0 \end{aligned} \quad (A-10d)$$

A.6 Matched Vertical Velocity Conditions

This condition implies that $w_i(x, \xi_i, t) = w_L(x, \xi_i, t)$ for $i = 1$ to $n=1$.

Taylor expansion at the mean interface elevations, $\hat{\xi}_1^i d_1$, is used again to obtain an approximate solution. From the upper layers, the vertical velocities are

$$\begin{aligned} w_i(x, \xi_i, t) &= w_i(x, -\hat{\xi}_1^i d_1, t) + \xi_i w'_i(x, -\hat{\xi}_1^i d_1, t) + \dots \\ &= w_i(x, -\hat{\xi}_1^i d_1, t) + \hat{w}'_i(-\hat{\xi}_1^i d_1) e^{j(kx-\sigma t)} \end{aligned} \quad (\text{A-11a})$$

From the lower layers, the vertical velocities are

$$w_L(x, \xi_i, t) = \hat{w}'_L(-\hat{\xi}_1^i d_1) e^{j(kx-\sigma t)} \quad (\text{A-11b})$$

The matching conditions are $\hat{w}'_i(-\hat{\xi}_1^i d_1) = \hat{w}'_L(-\hat{\xi}_1^i d_1)$. For the first interface, this condition gives

$$\begin{aligned} B_1 + C_1 - \sinh k d_1 A_2 - \cosh k d_1 B_2 - \sinh \lambda_2 d_1 C_2 - \\ \cosh \lambda_2 d_1 D_2 = 0 \end{aligned} \quad (\text{A-11c})$$

For the other interfaces, $i=2, \dots, N-1$, this condition gives

$$\begin{aligned} B_1 + D_1 - \sinh k d_L A_L - \cosh k d_L B_L - \sinh \lambda_L d_L C_L - \\ \cosh \lambda_L d_L D_L = 0 \end{aligned} \quad (\text{A-11d})$$

A.7 Linearized Kinematic Boundary Condition at Interfaces

This condition implies that $\partial \xi_i(x, t) / \partial t = w_i(x, -\hat{\xi}_1^i d_1, t)$ at the interfaces. Substituting $\xi_i = b_{10} e^{j(kx-\sigma t)}$ and Eq. A-3 in this condition yields

$$B_1 + D_1 = -j \omega b_{10} \quad (\text{A-12})$$

A.8 Matched Normal Stress Conditions

Normal stress $\sigma_i = p_i^t - 2\mu_i \frac{\partial w_i}{\partial z}$, where $p_i^t = p_i - p_1 g z - p_1^0$ is the total pressure. p_1^0 is given as

$$p_1^0 = \begin{cases} 0, & \text{if } i = 1 \\ \sum_{m=1}^{i-1} (\rho_m - \rho_{m-1}) g \left(\sum_{r=1}^m d_r \right), & \text{if } i > 1 \end{cases} \quad (A-13)$$

Where m, r are dummy indices.

At $i=1$ to $n-1$ interfaces, the normal stress, σ_i , from the upper layers are

$$\begin{aligned} \sigma_i(x, \xi_i, t) &= \sigma_i(x, -\sum d_i, t) + \xi_i \frac{\partial}{\partial z} \sigma_i(x, -\sum d_i, t) + \dots \\ &= [p_i^t - 2\mu_i \frac{\partial w_i}{\partial z}]|_{z=-\sum d_i} + \xi_i \frac{\partial}{\partial z} [p_i^t - 2\mu_i \frac{\partial w_i}{\partial z}]|_{z=-\sum d_i} + \dots \\ &= -p_1 g(-\sum d_i) - p_1^0 + [\hat{p}_i^t - 2\mu_i \frac{\partial \hat{w}_i}{\partial z} - b_{10} p_1 g]|_{z=-\sum d_i} e^{j(kx-\omega t)} \end{aligned} \quad (A-14a)$$

From the lower layers, the normal stresses, $\sigma_L(x, -\sum d_i, t)$, is

$$\sigma_L = -p_L g(-\sum d_i) - p_L^0 + [\hat{p}_L^t - 2\mu_L \frac{\partial \hat{w}_L}{\partial z} - b_{10} p_L g]|_{z=-\sum d_i} e^{j(kx-\omega t)} \quad (A-14b)$$

The matching condition, $\sigma_i(x, -\sum d_i, t) = \sigma_L(x, -\sum d_i, t)$ gives

$$\begin{aligned} (p_L - p_i)g(-\sum d_i) + (p_L^0 - p_i^0) &= \\ -[\hat{p}_i^t - 2\mu_i \frac{\partial \hat{w}_i}{\partial z} - b_{10} p_1 g - \hat{p}_L^t + 2\mu_L \frac{\partial \hat{w}_L}{\partial z} + b_{10} p_L g] e^{j(kx-\omega t)} & \end{aligned} \quad (A-14c)$$

Because $p_L^0 - p_i^0 = (p_L - p_i)g(\sum d_i)$, the bracket on the right hand side of

Eq. A-14 must be equal to zero. Substituting in Eq. A-2 and A-3 gives the normal stress matching conditions. For the first interface, it is

$$\begin{aligned} M_1 A_1 + 2\mu_1 \lambda_1 D_1 - M_2 \cosh k d_2 A_2 - M_2 \sinh k d_2 B_2 + \\ 2\mu_2 \lambda_2 \cosh \lambda_2 d_2 C_2 + 2\mu_2 \lambda_2 \sinh \lambda_2 d_2 D_2 + \\ (\rho_1 - \rho_2) g b_{1o} = 0 \quad \rho_2 - \rho_1 \end{aligned} \quad (A-15a)$$

For the other interfaces, this condition gives

$$\begin{aligned} M_1 A_1 + 2\mu_1 \lambda_1 C_1 - M_L \cosh k d_L A_L - M_L \sinh k d_L B_L + \\ 2\mu_L \lambda_L \cosh \lambda_L d_L C_L + 2\mu_L \lambda_L \sinh \lambda_L d_L D_L + \\ (\rho_1 - \rho_L) g b_{1o} = 0 \end{aligned} \quad (A-15b)$$

A.9 Matched Shear Stress Conditions

At $i=1$ to $n-1$ interfaces, the shear stresses, τ_i , from the upper layers are

$$\begin{aligned} \tau_i(x, \xi_i, t) &= \tau_i(x, -\sum d_i, t) + \xi_i \frac{\partial}{\partial z} \tau_i(x, -\sum d_i, t) + \dots \\ &= \mu_i \left(\frac{\partial u_i}{\partial z} + \frac{\partial w_i}{\partial x} \right) \Big|_{z=-\sum d_i} + \dots \\ &= \mu_i \left(\frac{j}{k} \hat{w}_i'' + jk \hat{w}_i' \right) \Big|_{z=-\sum d_i} e^{j(kx-\omega t)} \end{aligned} \quad (A-16a)$$

From the lower layers, the shear stress, τ_L , at the i^{th} interface is

$$\begin{aligned} \tau_L(x, \xi_i, t) &= \tau_L(x, -\sum d_i, t) + \xi_i \frac{\partial}{\partial z} \tau_L(x, -\sum d_i, t) + \dots \\ &= \mu_L \left(\frac{j}{k} \hat{w}_L'' + jk \hat{w}_L' \right) \Big|_{z=-\sum d_i} e^{j(kx-\omega t)} \end{aligned} \quad (A-16b)$$

The matched condition gives

$$\mu_1 [\hat{w}_1''(-\bar{z}d_1) + k^2 \hat{w}(-\bar{z}d_1)] = \mu_L [\hat{w}_L''(-\bar{z}d_1) + k^2 \hat{w}(-\bar{z}d_1)] \quad (A-16c)$$

Substituting for \hat{w} from Eq. A-3 into Eq. A-16c gives the required boundary conditions.

$$2\mu_1 k^2 B_1 + \mu_1 (k^2 + \lambda_1^2) D_1 = 2\mu_L k^2 \sinh kd_L A_L + 2\mu_L k^2 \cosh kd_L B_L \quad$$

$$\mu_L (k^2 + \lambda_L^2) \sinh \lambda_L d_L C_L - \mu_L (k^2 + \lambda_L^2) \cosh \lambda_L d_L D_L = 0 \quad (A-16d)$$

A.10 No-slip Conditions

The no-slip conditions at the rigid bottom are $u=w=0$. The horizontal zero velocity condition, i.e. $u=0$, gives

$$u_N(x, -\bar{z}d_N, t) = \hat{u}_N(-\bar{z}d_N) e^{j(kx-\omega t)} \\ - \frac{j}{k} \hat{w}'(-\bar{z}d_N) e^{j(kx-\omega t)} = 0$$

$$\text{or} \quad k A_N + \lambda_N C_N = 0 \quad (A-17)$$

The zero vertical velocity condition, i.e. $w=0$, gives

$$w_N(x, -\bar{z}d_N, t) = \hat{w}_N(-\bar{z}d_N) e^{j(kx-\omega t)} = 0$$

$$\text{or} \quad B_N + D_N = 0 \quad (A-18)$$

APPENDIX B
COMPARISON BETWEEN PREDICTION AND MEASUREMENT:
DYNAMIC PRESSURE AND HORIZONTAL VELOCITY

Comparison between the model predicted dynamic pressure amplitude profiles and measured dynamic pressure amplitudes in the mud bed for all 6 runs are presented. Model predicted velocity amplitude (\hat{u} and \hat{w}) profiles and measured horizontal velocities in the water column for the first 5 runs are also displayed. In Run 5 and Run 6, the amplitudes of horizontal movement of sediment particles near the side wall were recorded and converted to corresponding velocities. These data are also shown.

As discussed in Chapter 4, the observed horizontal velocity amplitudes in the mud bed, which include the boundary effects, were small. However, the velocity amplitude predicted by the 2-D model is free from the influence of side boundary. Figure B-1 shows the ratio of predicted to measured velocity amplitudes with an average value of 3.7. An effort to evaluate this ratio theoretically was made. Results are presented here.

First, an approach based on the assumption that the lateral velocity profile in the mud bed is similar to that of a 2-D Poiseuille flow was made. However, the flow field in a steady flow is different from that in an oscillatory flow. In an oscillatory flow, the velocity

profile across the flume is not parabolically distributed because the pressure force is mostly balanced by the inertia force. Furthermore, the large thickness of the bottom boundary layer (about 10 cm in thickness) restricted the assumption of a simple 2-D flow. Therefore, this approach did not work.

In the second approach, it was assumed that near the side wall, the lateral distribution of the horizontal velocity, $u(y)$, where y is the lateral coordinate, would have a profile similar to the vertical distribution of the horizontal velocity, $u(z)$, in the vertical coordinate. Since the side wall and the bottom of the flume were all made of plexiglass, it could be further assumed that these two profiles are in fact the same. Another assumption relative to the measured velocities was that they stand for the velocity at about $y = 0.5$ cm from the side wall. The selection of $y = 0.5$ cm, however, is rather arbitrary and needs more study about the representability. At an elevation 5 cm above the bottom, the velocity $u(z = 5 \text{ cm})$ can be treated as the velocity in the center of the flume. The profile of $u(z)$ was calculated from the 2-D model, as plotted in Fig. B-2 through B-11. A ratio of $u(z=5 \text{ cm})/u(z=0.5 \text{ cm})$ can be evaluated. This evaluation indicated the values of the predicted ratio varied from 4 to 7, which is not too far from the result shown in Fig. B-1.

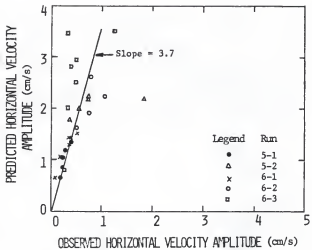


Fig. B-1. Comparison between Observed and Predicted Horizontal Velocity Amplitudes in the Bed.

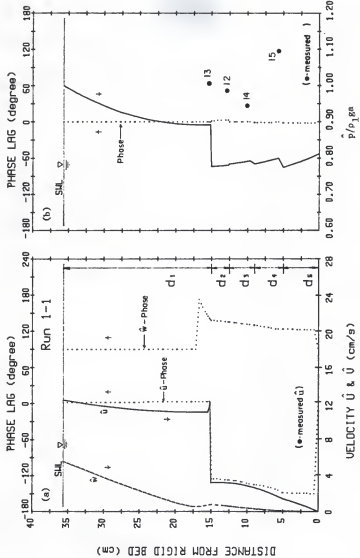


FIG. Br-2. Comparison of Model Prediction and Measurement for Run 1-1. (a) Velocity; (b) Pressure.

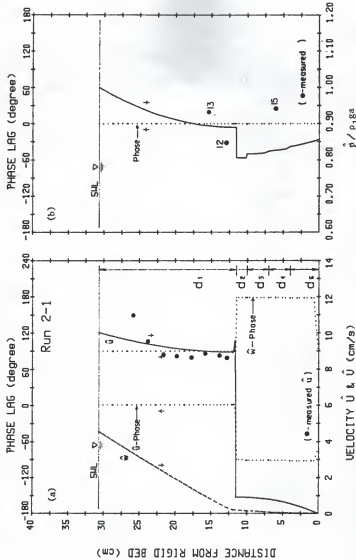


Fig. B-3. Comparison of Model Prediction and Measurement for Run 2-1. (a) Velocity: (b) Pressure.

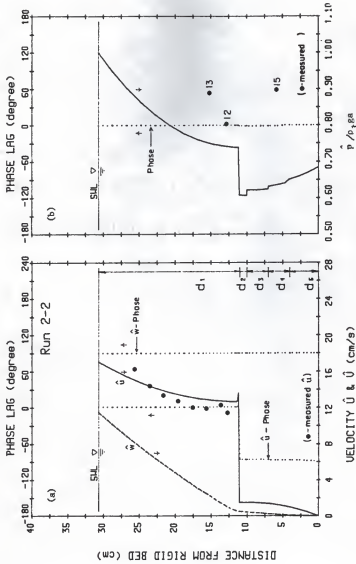


FIG. B-4. Comparison of Model Prediction and Measurement for Run 2-2. (a) Velocity; (b) Pressure.

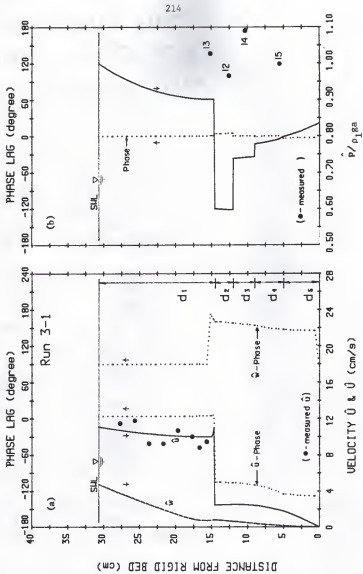


Fig. B-5. Comparison of Model Prediction and Measurement for Run 3-1. (a) Velocity; (b) Pressure.

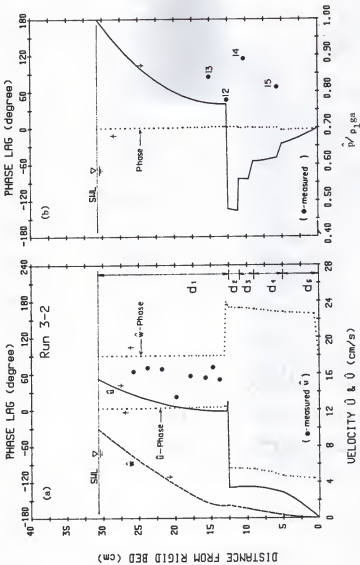


Fig. B-6. Comparison of Model Prediction and Measurement for Run 3-2. (a) Velocity; (b) Pressure.

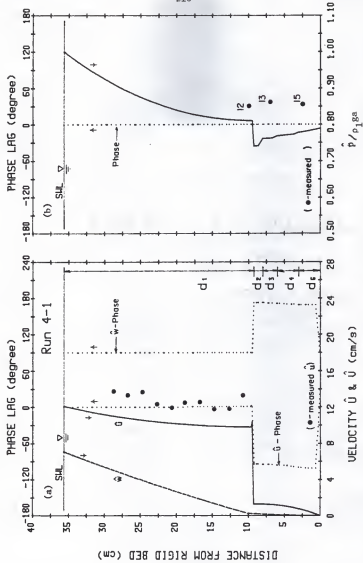


Fig. B-7. Comparison of Model Prediction and Measurement for Run 4-1. (a) Velocity; (b) Pressure.

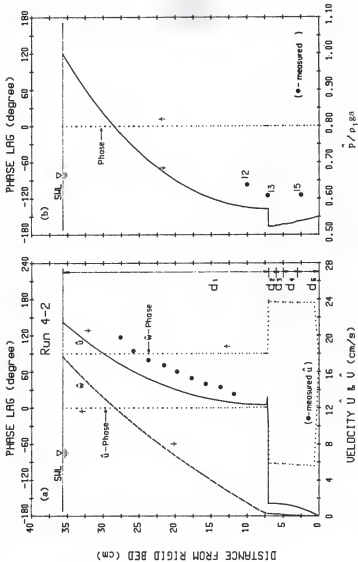


Fig. B-8. Comparison of Model Prediction and Measurement for Run 4-2. (a) Velocity; (b) Pressure.

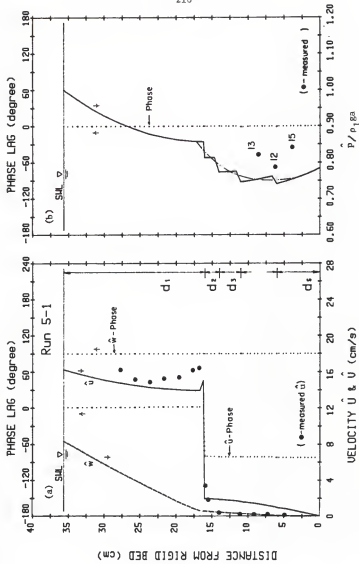


Fig. B-9. Comparison of Model Prediction and Measurement for Run 5-1. (a) Velocity; (b) Pressure.

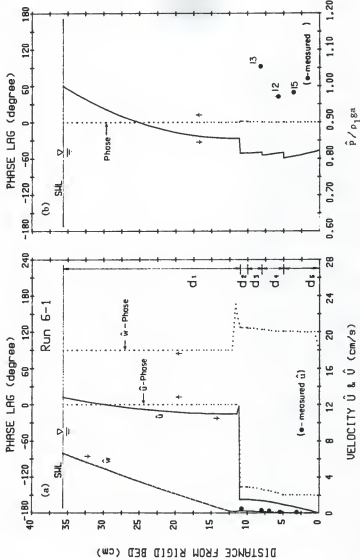


Fig. B-10. Comparison of Model Prediction and Measurement for Run 6-1. (a) Velocity; (b) Pressure.

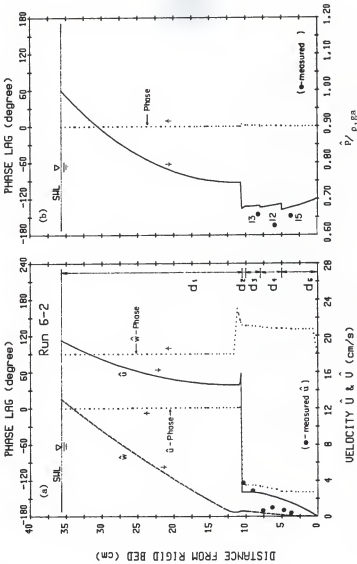


FIG. B-11. Comparison of Model Prediction and Measurement for Run 6-2. (a) Velocity; (b) Pressure.

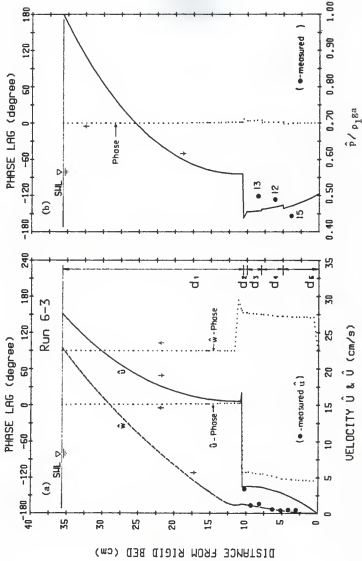


Fig. B-12. Comparison of Model Prediction and Measurement for Run 6-3. (a) Velocity; (b) Pressure.

APPENDIX C
MISCELLANEOUS CONSIDERATIONS FOR
THE EROSION EXPERIMENTS

The methodology for calibrating the current meter in a transient flow is presented first. Next, the design, calibration, and improvement needed for the light meter are discussed. Finally, a numerical low-pass filter used in data processing is described.

C.1 Calibration of the Current Meter under Oscillatory Flow

The response of a current meter in a transient flow is delayed by the inertia of the moving propeller or the electronic resistance. Therefore, the output is frequency-dependent. The impulse response function of the current meter is assumed as

$$h(t) = \begin{cases} \frac{c}{T_c} \exp(-t/T_c), & \text{for } t \geq 0 \\ 0, & \text{for } t < 0 \end{cases} \quad (C-1)$$

where t is the elapsed time, c and T_c are a proportionality constant and the time constant, respectively. Fourier transform gives the frequency response function as

$$F(\sigma) = \int_{-\infty}^{\infty} h(t) e^{-j\sigma t} dt = \frac{c}{1+j\sigma T_c} \quad (C-2)$$

where $j = \sqrt{-1}$. The modulus of the response function, $|F(\sigma)|$, is

$$|F(\sigma)| = \frac{c}{[1 + (\sigma T_c)^2]^{1/2}} \quad (C-3)$$

However, $|F(\sigma)|$ can not be determined from Eq.C-3 because c and T_c are unknown. Therefore, calibration is required to obtain these two constants.

The calibration was performed in a wave flume. The meter (model 523, manufactured by Marsh McBirney Inc.) was mounted at the tip of a piston rod which was originally used to move the paddle of a piston-type wave maker. The paddle was removed before the calibration tests were performed. The meter could only move back-and-forth in the longitudinal x-direction. Water depth was selected at about 30 cm to provide a still basin. The displacement of the current meter, $x(t)$, can be written as

$$x = a \exp(j\omega_0 t), \quad t \geq 0 \quad (C-4)$$

where a is half of the stroke distance which can be measured and $\omega_0 = 2\pi/T$ is the frequency of oscillation which could also be measured. The current meter moved at a velocity, $u(t)$, which can be obtained as

$$u = \partial x / \partial t = j\omega_0 a \exp(j\omega_0 t) \quad (C-5)$$

Assuming the output signal, $y(t)$, has the form

$$y(t) = b \exp(j\omega_0 t), \quad \text{for } t \geq 0 \quad (C-6)$$

where b is the output amplitude, usually in millivolts. The Fourier transform of $y(t)$ is

$$Y(\sigma) = 2\pi b \delta(\sigma - \omega_0) \quad (C-7)$$

The Fourier transform of $u(t)$ is similar to that for $y(t)$:

$$U(\sigma) = 2\pi a \omega_0 \delta(\sigma - \omega_0) \quad (C-8)$$

Therefore, the modulus of the frequency response function can also be obtained as

$$|F(\sigma_0)| = \frac{|Y(\sigma)|}{|U(\sigma)|} = \frac{b}{a\sigma_0} = \frac{c}{[1 + (\sigma_0 T_c)^2]^{1/2}} \quad (C-9)$$

where b and $a\sigma_0$ are known from the calibration test. Therefore, for selected values of σ_0 , a , and measured values of b , a plot of the corresponding $|F(\sigma)|$ can be made. Fig. C-1 gives an example. The extrapolation of the data to the intersection $\sigma = 0$ gives the c value. By trial and error, the time constant T_c can be obtained. For this example, the solid line shown in Fig. C-1 has values of $c = 4.85$ millivolt-sec/cm and $T_c = 0.8$ sec.

When the velocity time series is the objective, a relationship between $y(t)$ and $u(t)$ is necessary. This can be obtained as

$$\begin{aligned} y(t) &= \int_{-\infty}^{\infty} h(\tau) u(t-\tau) d\tau \\ &= \frac{ca\sigma_0}{T_c} \exp(j\sigma_0 t) \int_0^{\infty} \exp(-1/T_c - j\sigma_0)\tau d\tau \\ &= \frac{c}{1 + j\sigma_0 T_c} u(t) \end{aligned} \quad (C-10)$$

This equation is used to convert the digitized velocity output to the true velocity. Equation C-10 can be rewritten as

$$\begin{aligned} u(t) &= \frac{1}{c} [y(t) + j\sigma_0 T_c y(t)] \\ &= \frac{1}{c} [y(t) + T_c \frac{y(t+\Delta t) - y(t-\Delta t)}{2\Delta t}] \end{aligned} \quad (C-11)$$

Therefore a numerical procedure can be used to estimate the true time series of velocity, $u(t)$.

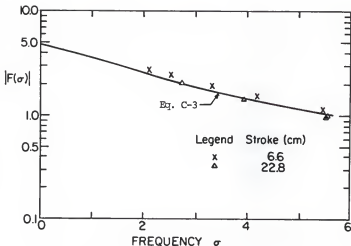


Fig. C-1. Normalized Frequency Response of the Current Meter.

C.2 Light Meter

The light meter was designed to detect instantaneous sediment concentration variation in the water column during wave erosion. The operating principle is that suspended sediment in water reduces light transmission, thus resulting in a higher attenuation of light than that for clear water. Inasmuch as a proportionality relationship holds between the sediment concentration and the degree of light decay, a device to sense the instantaneous light intensity from a constant light source can be used to measure the instantaneous concentration.

C.2.1 Design

The light meter was composed of three parts. The first part was a probe and a Light Emitting Diode (LED) driver. The LED driver provided a 10 kHz square wave, which is the most stable wave form and the frequency is far removed from electrical noises. Figure C-2 shows the circuit diagram of the LED driver. The probe had four units to observe the sediment concentration at four elevations simultaneously. They were numbered as unit 8, 9, 10, and 11 with unit 8 closest to the bottom. Each unit had a LED and a photo-diode. The four LEDs mounted on a semi-circular aluminum rod and separated vertically by 5 cm provided the light source. See Fig. C-3. The four photo-diodes, mounted on an adjacent semi-circular rod at the same elevations as LEDs, were used to detect the light intensity variation. The probe was immersed into the sediment-laden water to perform the designated function. The output from the photo-diodes (also 10 kHz AC signal but possibly inclusive of other low frequency background noise) depends on the sediment concentration, color, and particle size. The signal is then fed into the second part.

The second part was a pre-amplifier. See Fig. C-4. The purpose was to magnify the small signals detected by the photo-diodes and to allow for longer distance transmission. The signal levels were adjusted such that all four channels had approximately equal output voltages for the same sediment concentration. This part was placed as close as possible to the probe in order to minimize the effects of background noise. The amplified signals were then sent to the third part.

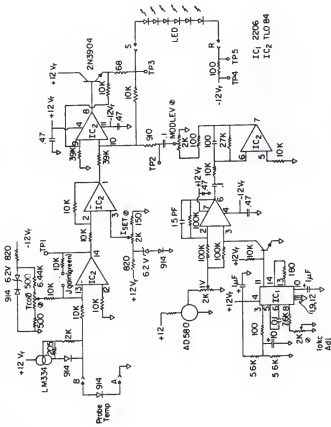


Fig. C-2. Circuit Diagram for the LED Driver of Light Meter.

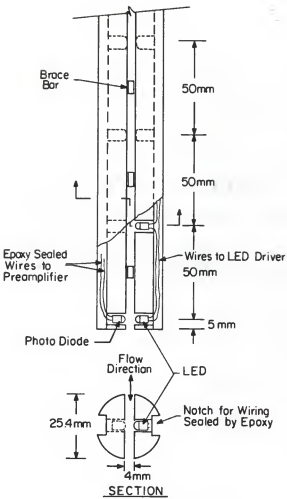


Fig. C-3. Light Meter Probe.

The third part was the main processor which contained a high-pass filter, a rectifier and a DC amplifier. Fig C-5 shows the circuit diagram. The filter was designed to eliminate all low frequency noise, e.g., 60 Hz AC. The purified 10 kHz AC signal was then rectified and fed into the DC amplifier. The zero and amplification ratio were adjusted at this stage for different sediment concentration ranges. For these experiments, the output DC signal had a voltage of +2.5 volts for clear water or initial concentration, down to -2.5 volts for the possible maximum sediment concentration, which had to be estimated a priori. These DC signals were then sent to the data acquisition system for recording.

C.2.2 Light Meter Calibration

Calibration of the light meter required a constant suspension sediment concentration in the water column. This was accomplished as shown in Fig. C-6. Sediment-laden water in a 5 cm ϕ PVC pipe, sealed at one end, with an inlet at the bottom and an outlet at the top, was circulated by a small pump (made by Precision Scientific Company). The pump provided a discharge rate of about 40 cm³/sec. This was equivalent to a 2 cm/sec upward velocity in the PVC pipe. This upward velocity was much greater than the settling velocity of fine sediment, e.g. 0.3 cm/sec for most fine sediments (Hayter, 1983). Therefore, constant and uniform sediment concentrations could be achieved in the pipe after a few minutes of circulation. The probe was inserted in the pipe and the output voltage was recorded by the data acquisition system and analyzed later. A water sample (about 20 cm³) was also taken to obtain

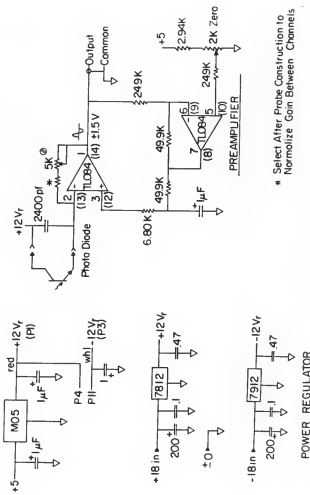


Fig. C-4. Circuit Diagram for the Pre-Amplifier of Light Meter.

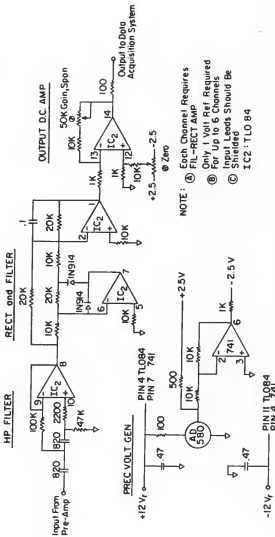


Fig. C-5. Circuit Diagram for the Main Processor of Light Meter.

the sediment concentration using the Millipore filtering apparatus and the procedure given by Yeh (1979). By adding clear water or sediment slurry, the concentration could be altered. The calibration curves were obtained by increasing the sediment concentration to a maximum and then decreasing back to a low concentration. Figure C-7 shows the calibration curve for kaolinite. Figure C-8 is for the mud used in Runs 5 and 6. The unique relationship shown by the two calibration figures attests to the utility of the light meter. The non-linear response curves, however, indicate that the light transmission is a non-linear function of sediment concentration.

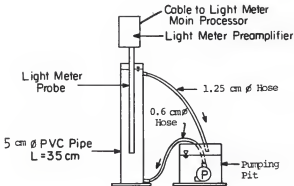


Fig. C-6. Light Meter Calibration Device.

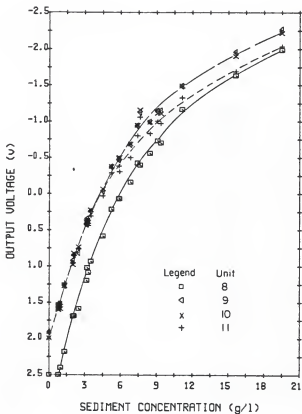


Fig. C-7. Light Meter Calibration Curves for Kaolinite.

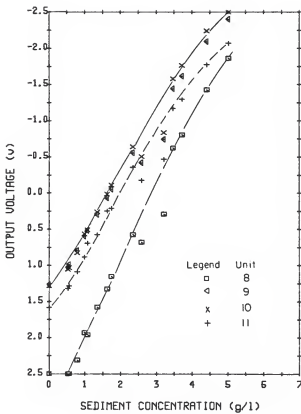


FIG. C-8. Light Meter Calibration Curves for Cedar Key Mud.

C.3 Numerical Low-Pass Filter

An ideal low-pass filter has a frequency response function $H(\omega)$ shown in Fig. C-9a (dashed line). This function is equal to unity whenever the frequency is less than the cut-off frequency, ω_c , and equals zero when the frequency is higher. Based on the knowledge that the noise is mainly in the high frequency range and the wave frequency σ (a known value) is quite low compared to noise frequency, $\omega_c = 3\sigma$ was chosen.

In the frequency domain $H(\omega)$ and the Fourier transform of the time series are multiplied to filter out the high frequency noise. In the time domain, a convolution integral is involved:

$$R(t) = r(t) * h(t) \\ = \int_{-\infty}^{\infty} r(t-\tau) h(\tau) d\tau \quad (c-12a)$$

$$= \sum_{n=1}^{N} r(t-n\Delta t) h(n\Delta t) \Delta t \quad (c-12b)$$

with $h(\tau) = \sin(\omega_c \tau) / \pi \tau$ or $h(n\Delta t) = \sin(\omega_c n\Delta t) / n\Delta t$. Here $r(t)$ is the original record, $h(t)$ is the Fourier inverse transform of $H(\omega)$ as shown in Fig. C-9b, and $R(t)$ is the data after filtering. Numerically, only finite terms can be selected in the integration as shown by Eq. c-12b. This indicates a truncation of $h(\tau)$, and therefore, the actual $H(\omega)$ is deviated from the ideal $H(\omega)$. Here $n = 30$ was chosen and the actual $H(\omega)$ was also displayed as the solid line in Fig. C-9a. This figure indicates a 2% deviation at the wave frequency after the filtering which revealed that $n = 30$ was acceptable. An example comparing raw and filtered data (wave record) is displayed in Fig. C-10 and shows that most of the spikes were smoothed out.

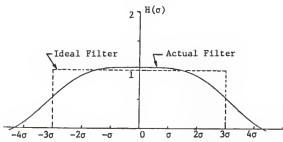
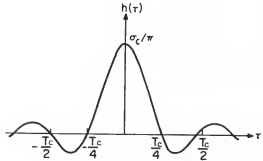
(a) Frequency Response Function $H(\sigma)$ (b) Fourier Inverse Transform of $H(\sigma)$

Fig. C-9. Response Function of the Low-Pass Filter.

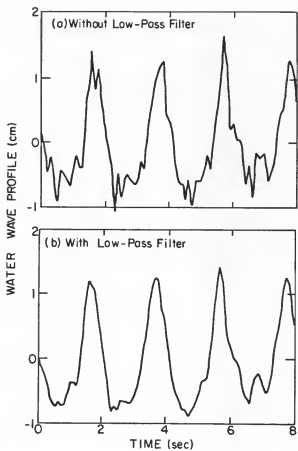


Fig. C-10. Comparison of Data Record with/without the Low-Pass Filter.

APPENDIX D
DATA ON EROSION TESTS

The measured suspended sediment concentrations and the corresponding intake elevations are tabulated here. Wave loading, mud bed density profiles, and pressure response for each run are displayed next. Instantaneous sediment concentration measurement for Run 6 are plotted at last.

D.1 Suspended Sediment Concentration and Mud Surface Elevation

D.1.1 Run 1, Kaolinite, SWL = 0.356 m

Concentration measurement at station A, $x = 1.47$ m, with 22 records
Conc. probe elevation (cm) = 22.0
Suspended sediment concentration (g/l) at each time step (same as station B, not shown) are listed below.

0.0 0.0 0.0 0.0 0.0 0.0 0.0 0.0 0.0 0.0 0.009
0.008 0.012 0.012 0.016 0.026 0.026 0.026 0.030 0.048 0.058
0.050 0.062

Concentration measurement at station B, $x = 5.93$ m, with 22 records

no	time (min)	elev (cm)	C (g/l)	elev (cm)	C (g/l)	elev (cm)	C (g/l)	elev (cm)	C (g/l)
1	0	(16.1	0.002)	(17.2	0.002)	(19.0	0.002)	(27.4	0.002)
2	6	(16.1	0.222)	(17.2	0.114)	(19.0	0.037)	(27.4	0.008)
3	18	(16.1	0.072)	(17.2	0.034)	(19.0	0.015)	(21.8	0.012)
4	34	(16.1	0.149)	(17.2	0.076)	(19.0	0.022)	(27.4	0.004)
5	52	(16.1	0.112)	(17.2	0.086)	(19.0	0.044)	(27.4	0.002)
6	75	(16.1	0.140)	(17.2	0.054)	(19.0	0.046)	(27.4	0.042)
7	106	(15.6	0.044)	(16.7	0.030)	(18.5	0.008)	(26.9	0.006)
8	141	(15.1	0.048)	(16.2	0.016)	(18.0	0.002)	(26.4	0.002)
9	173	(15.1	0.114)	(16.2	0.022)	(18.0	0.038)	(20.8	0.028)
10	231	(15.1	0.302)	(16.2	0.100)	(18.0	0.064)	(26.4	0.028)

11	291	(15.1	0.216)	(16.2	0.072)	(18.0	0.046)	(26.4	0.024)
12	351	(15.1	0.084)	(16.2	0.030)	(18.0	0.030)	(20.8	0.018)
13	411	(13.6	11.225)	(14.7	0.050)	(16.5	0.032)	(24.9	0.026)
14	429	(13.6	0.154)	(14.7	0.118)	(16.5	0.106)	(24.9	0.064)
15	459	(13.1	0.310)	(14.2	0.232)	(16.0	0.178)	(24.4	0.120)
16	489	(11.6	3.120)	(12.7	0.330)	(14.5	0.214)	(22.9	0.144)
17	555	(11.6	8.140)	(12.7	0.314)	(14.5	0.208)	(22.9	0.152)
18	615	(11.6	4.184)	(12.7	0.284)	(14.5	0.212)	(22.9	0.128)
19	669	(11.6	3.180)	(12.7	0.292)	(14.5	0.206)	(22.9	0.142)
20	730	(11.6	5.305)	(12.7	0.360)	(14.5	0.220)	(22.9	0.138)
21	790	(11.6	2.472)	(12.7	0.406)	(14.5	0.224)	(22.9	0.130)
22	850	(11.6	2.340)	(12.7	0.276)	(14.5	0.192)	(22.9	0.130)

Concentration measurement at station C, x = 8.50 m, with 22 records

no	time	elev	C	elev	C	elev	C	elev	C
	(min)	(cm)	(g/l)	(cm)	(g/l)	(cm)	(g/l)	(cm)	(g/l)
1	0	(15.9	0.005)	(17.1	0.002)	(19.0	0.002)	(27.3	0.001)
2	6	(15.9	0.052)	(17.1	0.003)	(19.0	0.002)	(27.3	0.001)
3	18	(15.9	0.120)	(17.1	0.062)	(19.0	0.034)	(21.8	0.012)
4	34	(15.9	0.070)	(17.1	0.030)	(19.0	0.016)	(27.3	0.004)
5	52	(15.9	0.103)	(17.1	0.035)	(19.0	0.017)	(27.3	0.002)
6	75	(15.9	0.136)	(17.1	0.040)	(19.0	0.018)	(27.3	0.012)
7	106	(14.4	0.168)	(15.6	0.025)	(17.5	0.030)	(25.8	0.004)
8	141	(14.4	0.094)	(15.6	0.018)	(17.5	0.016)	(25.8	0.002)
9	173	(13.9	7.378)	(15.1	0.036)	(17.0	0.040)	(19.8	0.030)
10	231	(13.4	9.692)	(14.6	0.046)	(16.5	0.018)	(24.8	0.002)
11	291	(13.4	0.264)	(14.6	0.006)	(16.5	0.003)	(24.8	0.002)
12	351	(13.4	0.092)	(14.6	0.036)	(16.5	0.003)	(24.8	0.002)
13	411	(12.9	0.350)	(14.1	0.084)	(16.0	0.006)	(24.3	0.002)
14	429	(12.9	100.00)	(14.1	51.580)	(16.0	0.198)	(24.3	0.028)
15	459	(12.9	100.00)	(14.1	51.700)	(16.0	0.204)	(18.8	0.014)
16	489	(13.9	4.350)	(15.1	0.284)	(17.0	0.154)	(25.3	0.038)
17	555	(13.9	5.452)	(15.1	0.258)	(17.0	0.186)	(25.3	0.038)
18	615	(13.9	5.000)	(15.1	0.226)	(17.0	0.152)	(25.3	0.042)
19	669	(13.9	3.276)	(15.1	0.204)	(17.0	0.140)	(25.3	0.042)
20	730	(13.9	3.660)	(15.1	0.212)	(17.0	0.144)	(25.3	0.046)
21	790	(13.9	10.090)	(15.1	0.240)	(17.0	0.174)	(25.3	0.054)
22	850	(13.9	2.904)	(15.1	0.218)	(17.0	0.150)	(25.3	0.044)

Concentration measurement at station D, x = 12.30 m, with 22 records

no	time	elev	C	elev	C	elev	C	elev	C
	(min)	(cm)	(g/l)	(cm)	(g/l)	(cm)	(g/l)	(cm)	(g/l)
1	0	(15.8	0.005)	(17.0	0.004)	(18.9	0.002)	(27.3	0.002)
2	6	(15.8	111.70)	(17.0	0.052)	(18.9	0.002)	(21.8	0.002)
3	18	(15.8	111.70)	(17.0	17.530)	(18.9	0.176)	(27.3	0.011)
4	34	(16.3	3.100)	(17.5	0.114)	(19.4	0.036)	(27.8	0.002)
5	52	(16.3	0.148)	(17.5	0.054)	(19.4	0.032)	(27.8	0.002)
6	75	(16.3	0.228)	(17.5	0.050)	(19.4	0.024)	(27.8	0.004)

7	106	(16.3 0.220)	(17.5 0.020)	(19.4 0.020)	(27.8 0.004)
8	141	(16.3 0.265)	(17.5 0.067)	(19.4 0.016)	(27.8 0.011)
9	173	(16.3 0.256)	(17.5 0.084)	(19.4 0.012)	(22.3 0.014)
10	231	(16.3 0.356)	(17.5 0.082)	(19.4 0.034)	(27.8 0.015)
11	291	(16.3 1.636)	(17.5 0.110)	(19.4 0.034)	(27.8 0.018)
12	351	(16.3 0.472)	(17.5 0.174)	(19.4 0.050)	(27.8 0.020)
13	411	(16.3 0.752)	(17.5 0.134)	(19.4 0.052)	(27.8 0.014)
14	429	(16.3 1.860)	(17.5 0.158)	(19.4 0.054)	(27.8 0.026)
15	459	(16.3 0.906)	(17.5 0.148)	(19.4 0.085)	(27.8 0.030)
16	489	(16.3 0.588)	(17.5 0.124)	(19.4 0.084)	(27.8 0.022)
17	555	(16.3 0.336)	(17.5 0.134)	(19.4 0.104)	(27.8 0.036)
18	615	(16.3 3.144)	(17.5 0.146)	(19.4 0.120)	(27.8 0.032)
19	669	(16.3 15.495)	(17.5 0.154)	(19.4 0.112)	(27.8 0.036)
20	730	(16.3 17.850)	(17.5 0.150)	(19.4 0.130)	(27.8 0.044)
21	790	(16.3 17.953)	(17.5 0.134)	(19.4 0.100)	(27.8 0.046)
22	850	(16.3 24.684)	(17.5 0.152)	(19.4 0.118)	(27.8 0.042)

Concentration measurement at station E, x = 14.20 m, with 22 records

no	time	elev	C	elev	C	elev	C	elev	C
	(min)	(cm)	(g/l)	(cm)	(g/l)	(cm)	(g/l)	(cm)	(g/l)
1	0	(15.2 0.002)	(16.4 0.002)	(18.5 0.002)	(26.9 0.002)				
2	6	(15.2 0.022)	(16.4 0.018)	(18.5 0.002)	(26.9 0.004)				
3	18	(15.2 0.037)	(16.4 0.015)	(18.5 0.002)	(26.9 0.002)				
4	34	(15.2 22.650)	(16.4 0.006)	(18.5 0.002)	(26.9 0.002)				
5	52	(15.2 0.358)	(16.4 0.042)	(18.5 0.020)	(26.9 0.010)				
6	75	(15.2 1.584)	(16.4 0.028)	(18.5 0.018)	(26.9 0.010)				
7	106	(15.2 0.106)	(16.4 0.002)	(18.5 0.002)	(26.9 0.002)				
8	141	(15.2 0.106)	(16.4 0.002)	(18.5 0.002)	(26.9 0.002)				
9	173	(15.2 0.080)	(16.4 0.014)	(18.5 0.012)	(26.9 0.004)				
10	231	(15.2 0.186)	(16.4 0.020)	(18.5 0.008)	(26.9 0.006)				
11	291	(15.2 0.772)	(16.4 0.024)	(18.5 0.008)	(26.9 0.002)				
12	351	(15.2 0.250)	(16.4 0.012)	(18.5 0.006)	(26.9 0.002)				
13	411	(15.2 2.556)	(16.4 0.002)	(18.5 0.002)	(26.9 0.002)				
14	429	(15.2 0.354)	(16.4 0.002)	(18.5 0.002)	(26.9 0.002)				
15	459	(15.2 0.134)	(16.4 0.014)	(18.5 0.002)	(26.9 0.002)				
16	489	(15.2 0.132)	(16.4 0.046)	(18.5 0.026)	(26.9 0.002)				
17	555	(15.2 0.196)	(16.4 0.074)	(18.5 0.050)	(26.9 0.002)				
18	615	(15.2 0.416)	(16.4 0.112)	(18.5 0.060)	(26.9 0.016)				
19	669	(15.2 0.422)	(16.4 0.108)	(18.5 0.066)	(26.9 0.018)				
20	730	(15.2 0.360)	(16.4 0.138)	(18.5 0.102)	(26.9 0.050)				
21	790	(15.2 0.366)	(16.4 0.078)	(18.5 0.062)	(26.9 0.046)				
22	850	(15.2 0.324)	(16.4 0.078)	(18.5 0.072)	(26.9 0.050)				

Bed elevation information

Elapsed Time x(m) = ...
 min 5.57 6.57 7.57 8.57 9.57 10.57 11.57 12.57

0	15.45	15.55	15.55	15.05	14.25	14.55	14.95	14.85
30	12.75	13.95	14.05	13.15	13.35	14.25	15.05	16.05

46	12.95	14.15	13.95	12.75	12.75	14.25	15.25	16.25
132	12.85	14.15	14.05	12.65	13.05	13.95	14.85	16.25
167	13.05	14.15	14.15	12.65	12.55	13.75	14.95	16.15
223	13.55	14.15	13.45	12.85	12.45	13.05	15.05	16.35
318	13.25	13.95	13.25	12.25	12.65	13.45	15.25	16.45
375	13.25	13.95	13.25	12.25	12.65	13.15	15.25	16.55
414	13.25	13.95	13.25	12.25	12.65	13.15	15.25	16.55
427	10.45	11.45	12.85	13.35	14.45	14.75	15.45	15.45
437	10.15	11.45	12.55	13.55	14.35	14.95	15.55	16.15
462	10.45	11.65	12.55	13.35	14.15	14.85	15.45	15.85
478	10.65	11.65	12.55	13.05	14.15	14.55	15.45	15.65
624	10.65	11.65	12.65	13.05	14.25	14.55	15.45	15.55
672	10.55	11.55	12.65	13.05	14.15	14.55	15.35	15.55
737	10.55	11.55	12.55	13.15	14.15	14.55	15.25	15.65
801	10.25	11.55	12.55	13.15	14.05	14.55	15.25	15.55
861	10.25	11.55	12.55	13.15	14.05	14.55	15.25	15.55

D.1.2 Run 2, Kaolinite, SWL = 0.306 m

Concentration measurement at station A, $x = 1.47$ m, with 15 records
 Conc. probe elevation (cm) = 22 cm

Suspended sediment concentration (g/l) at each time step (same as station B, not shown) are listed below.

0.000 0.000 0.000 0.000 0.000 0.000 0.005 0.006 0.009 0.014
 0.029 0.028 0.031 0.029 0.038

Concentration measurement at station B, $x = 5.93$ m, with 15 records

no	time (min)	elev (cm)	C (g/l)	elev (cm)	C (g/l)	elev (cm)	C (g/l)	elev (cm)	C (g/l)
1	0	(12.8	0.000)	(13.9	0.000)	(15.7	0.000)	(24.1	0.000)
2	20	(12.8	0.058)	(13.9	0.012)	(15.7	0.012)	(24.1	0.017)
3	45	(12.3	0.049)	(13.4	0.012)	(15.2	0.011)	(23.6	0.008)
4	90	(12.3	0.038)	(13.4	0.012)	(15.2	0.014)	(23.6	0.011)
5	150	(12.3	0.031)	(13.4	0.015)	(15.2	0.014)	(23.6	0.009)
6	210	(12.3	0.040)	(13.4	0.014)	(15.2	0.017)	(23.6	0.014)
7	270	(12.3	0.048)	(13.4	0.015)	(15.2	0.014)	(23.6	0.011)
8	330	(12.3	1.835)	(13.4	0.338)	(15.2	0.140)	(23.6	0.046)
9	351	(12.3	1.955)	(13.4	0.946)	(15.2	0.286)	(23.6	0.074)
10	371	(11.8	1.020)	(12.9	0.552)	(14.7	0.312)	(23.1	0.189)
11	421	(10.7	0.449)	(11.8	0.305)	(13.6	0.248)	(22.0	0.183)
12	481	(10.7	0.195)	(11.8	0.177)	(13.6	0.182)	(22.0	0.154)
13	541	(10.1	0.332)	(11.2	0.209)	(13.0	0.178)	(21.4	0.142)
14	601	(10.1	0.288)	(11.2	0.177)	(13.0	0.163)	(21.4	0.122)
15	661	(10.1	0.242)	(11.2	0.142)	(13.0	0.126)	(21.4	0.109)

Concentration measurement at station C, x = 8.50 m, with 15 records

no	time (min)	elev (cm)	C (g/l)	elev (cm)	C (g/l)	elev (cm)	C (g/l)	elev (cm)	C (g/l)
1	0	(11.5	0.000)	(12.6	0.000)	(14.5	0.000)	(22.8	0.000)
2	20	(11.5	0.050)	(12.6	0.020)	(14.5	0.005)	(22.8	0.002)
3	45	(11.5	0.900)	(12.6	0.029)	(14.5	0.006)	(22.8	0.008)
4	90	(11.5	2.174)	(12.6	0.018)	(14.5	0.009)	(22.8	0.008)
5	150	(11.5	1.202)	(12.6	0.023)	(14.5	0.012)	(22.8	0.009)
6	210	(11.5	1.540)	(12.6	0.028)	(14.5	0.009)	(22.8	0.009)
7	270	(11.5	1.806)	(12.6	0.029)	(14.5	0.014)	(22.8	0.006)
8	330	(11.5	2.722)	(12.6	0.115)	(14.5	0.040)	(22.8	0.029)
9	351	(11.5	9.840)	(12.6	0.696)	(14.5	0.220)	(22.8	0.085)
10	371	(11.0	45.352)	(12.1	1.394)	(14.0	0.295)	(22.3	0.092)
11	421	(11.5	9.172)	(12.6	2.182)	(14.5	0.466)	(22.8	0.134)
12	481	(11.5	4.054)	(12.6	0.782)	(14.5	0.438)	(22.8	0.140)
13	541	(11.5	2.572)	(12.6	1.506)	(14.5	0.700)	(22.8	0.102)
14	601	(11.5	2.562)	(12.6	1.730)	(14.5	0.618)	(22.8	0.106)
15	661	(11.5	1.686)	(12.6	0.697)	(14.5	0.423)	(22.8	0.095)

Concentration measurement at station D, x = 12.30 m, with 15 records

no	time (min)	elev (cm)	C (g/l)	elev (cm)	C (g/l)	elev (cm)	C (g/l)
1	0	(12.3	0.000)	(13.5	0.000)	(15.4	0.000)
2	20	(12.3	0.037)	(13.5	0.000)	(15.4	0.000)
3	45	(13.3	0.317)	(14.5	0.062)	(16.4	0.037)
4	90	(13.3	0.244)	(14.5	0.133)	(16.4	0.077)
5	150	(13.3	0.217)	(14.5	0.123)	(16.4	0.098)
6	210	(13.3	0.222)	(14.5	0.123)	(16.4	0.089)
7	270	(13.3	0.285)	(14.5	0.140)	(16.4	0.120)
8	330	(13.3	6.664)	(14.5	0.984)	(16.4	0.392)
9	351	(13.3	18.388)	(14.5	0.828)	(16.4	0.248)
10	371	(13.3	38.200)	(14.5	0.515)	(16.4	0.263)
11	421	(13.3	98.626)	(14.5	4.728)	(16.4	0.192)
12	481	(13.3	168.203)	(14.5	21.666)	(16.4	0.174)
13	541	(13.8	45.000)	(15.0	0.138)	(16.9	0.080)
14	601	(13.8	14.250)	(15.0	0.545)	(16.9	0.066)
15	661	(13.8	16.246)	(15.0	0.163)	(16.9	0.103)

Concentration measurement at station E, x = 14.20 m, with 15 records

no.	time (min)	elev (cm)	C (g/l)	elev (cm)	C (g/l)
1	0.00	(15.2,	0.000)	(22.3,	0.000)
2	20.00	(15.2,	0.000)	(26.9,	0.000)
3	45.00	(15.2,	0.023)	(26.9,	0.005)
4	90.00	(15.2,	0.015)	(26.9,	0.009)
5	150.00	(15.2,	0.023)	(26.9,	0.020)

6	210.00	(15.2, 0.045)	(26.9, 0.015)
7	270.00	(15.2, 0.032)	(26.9, 0.026)
8	330.00	(15.2, 0.118)	(26.9, 0.042)
9	351.00	(15.2, 0.151)	(26.9, 0.106)
10	371.00	(15.2, 0.143)	(26.9, 0.120)
11	421.00	(15.2, 0.150)	(26.9, 0.106)
12	481.00	(15.2, 0.148)	(26.9, 0.100)
13	541.00	(15.2, 0.134)	(26.9, 0.072)
14	601.00	(15.2, 0.240)	(26.9, 0.108)
15	661.00	(15.2, 0.288)	(26.9, 0.100)

Bed elevation information

Elapsed Time	x(m)...								
min	5.57	6.57	7.57	8.57	9.57	10.57	11.57	12.57	

0	12.45	11.75	11.35	11.25	11.07	11.20	11.75	11.75	
18	12.45	11.75	11.25	11.15	11.05	11.15	11.75	11.75	
66	12.45	11.75	11.25	11.15	11.00	11.15	11.65	11.65	
120	12.35	11.70	11.25	11.15	11.05	11.15	11.65	11.75	
222	12.40	11.65	11.25	11.15	11.00	11.15	11.65	11.70	
255	12.40	11.65	11.25	11.15	11.00	11.15	11.65	11.70	
343	12.35	11.65	11.20	11.10	11.00	11.10	11.65	11.65	
393	10.65	11.35	11.50	11.15	10.95	11.10	11.65	11.65	
423	9.75	10.45	11.05	10.95	11.15	11.05	11.85	11.65	
452	9.65	10.15	10.65	10.95	11.15	11.05	12.05	11.65	
508	9.45	9.85	10.30	11.35	10.95	11.35	11.55	11.65	
571	9.45	9.85	10.25	11.05	10.95	11.15	11.65	11.65	
598	9.45	9.95	10.55	11.05	11.25	11.05	12.05	11.65	
630	9.45	9.95	10.45	11.05	10.75	11.05	11.55	11.55	
732	9.45	9.95	10.35	11.05	10.85	11.05	11.55	11.55	

D.1.3 Run 3, Kaolinite, SWL = 0.306 m

Concentration measurement at station A, $x = 1.47$ m, with 14 records
 Cono. probe elevation (cm) = 22 cm
 Suspended sediment concentration (g/l) at each time step (same as station B, not shown) are listed below.

0.000	0.005	0.009	0.006	0.006	0.009	0.008	0.009	0.017	0.020
0.025	0.029	0.035	0.042						

Concentration measurement at station B, $x = 5.93$ m, with 14 records

no	time	elev	C	elev	C	elev	C	elev	C
		(min)	(cm)	(g/l)	(cm)	(g/l)	(cm)	(g/l)	(g/l)
1	0	(16.0	0.000)	(17.1	0.000)	(18.9	0.000)	(27.3	0.000)

2	10	(16.0 0.029)	(17.1 0.023)	(18.9 0.015)	(27.3 0.014)
3	60	(15.0 0.029)	(16.1 0.029)	(17.9 0.025)	(26.3 0.025)
4	120	(14.5 0.088)	(15.6 0.031)	(17.4 0.028)	(25.8 0.023)
5	180	(14.5 0.045)	(15.6 0.034)	(17.4 0.037)	(25.8 0.031)
6	240	(14.5 0.075)	(15.6 0.055)	(17.4 0.042)	(25.8 0.032)
7	300	(14.0 0.274)	(15.1 0.078)	(16.9 0.068)	(25.3 0.046)
8	320	(14.0 0.126)	(15.1 0.122)	(16.9 0.118)	(25.3 0.122)
9	376	(14.0 0.128)	(15.1 0.135)	(16.9 0.122)	(25.3 0.115)
10	436	(14.0 0.132)	(15.1 0.145)	(16.9 0.140)	(25.3 0.132)
11	496	(14.0 0.171)	(15.1 0.160)	(16.9 0.154)	(25.3 0.138)
12	556	(14.0 0.189)	(15.1 0.175)	(16.9 0.149)	(25.3 0.154)
13	616	(14.0 0.168)	(15.1 0.155)	(16.9 0.152)	(25.3 0.137)
14	676	(14.0 0.171)	(15.1 0.162)	(16.9 0.165)	(25.3 0.143)

Concentration measurement at station C, x = 8.50 m, with 14 records

no	time	elev	C	elev	C	elev	C	elev	C
	(min)	(cm)	(g/l)	(cm)	(g/l)	(cm)	(g/l)	(cm)	(g/l)
1	0	(15.5 0.000)	(16.6 0.000)	(18.5 0.000)	(26.8 0.000)				
2	10	(15.5 0.015)	(16.6 0.009)	(18.5 0.008)	(26.8 0.008)				
3	60	(15.5 0.034)	(16.6 0.014)	(18.5 0.014)	(26.8 0.011)				
4	120	(14.5 0.308)	(15.6 0.017)	(17.5 0.015)	(25.8 0.015)				
5	180	(14.5 0.048)	(15.6 0.012)	(17.5 0.012)	(25.8 0.011)				
6	240	(14.5 0.088)	(15.6 0.012)	(17.5 0.012)	(25.8 0.014)				
7	300	(13.5 0.272)	(14.6 0.026)	(16.5 0.025)	(24.8 0.026)				
8	320	(13.5 0.900)	(14.6 0.060)	(16.5 0.051)	(24.8 0.031)				
9	376	(13.5 0.208)	(14.6 0.085)	(16.5 0.095)	(24.8 0.069)				
10	436	(13.5 0.235)	(14.6 0.102)	(16.5 0.112)	(24.8 0.085)				
11	496	(13.5 0.251)	(14.6 0.098)	(16.5 0.115)	(24.8 0.095)				
12	556	(13.5 0.271)	(14.6 0.102)	(16.5 0.122)	(24.8 0.092)				
13	616	(13.5 0.252)	(14.6 0.108)	(16.5 0.132)	(24.8 0.106)				
14	676	(13.5 0.320)	(14.6 0.111)	(16.5 0.120)	(24.8 0.109)				

Concentration measurement at station D, x = 12.30 m, with 14 records

no	time	elev	C	elev	C	elev	C	elev	C
	(min)	(cm)	(g/l)	(cm)	(g/l)	(cm)	(g/l)	(cm)	(g/l)
1	0	(14.8 0.000)	(16.0 0.000)	(17.9 0.000)	(26.3 0.000)				
2	10	(14.8 6.899)	(16.0 0.034)	(17.9 0.009)	(26.3 0.006)				
3	60	(14.8 0.106)	(16.0 0.011)	(17.9 0.008)	(26.3 0.009)				
4	120	(14.8 0.380)	(16.0 0.011)	(17.9 0.006)	(26.3 0.008)				
5	180	(14.8 1.946)	(16.0 0.014)	(17.9 0.009)	(26.3 0.011)				
6	240	(14.8 1.012)	(16.0 0.023)	(17.9 0.014)	(26.3 0.022)				
7	300	(14.8 1.184)	(16.0 0.015)	(17.9 0.011)	(26.3 0.018)				
8	320	(14.8 21.516)	(16.0 0.018)	(17.9 0.015)	(26.3 0.018)				
9	376	(14.8 11.952)	(16.0 0.029)	(17.9 0.020)	(26.3 0.018)				
10	436	(14.8 2.396)	(16.0 0.037)	(17.9 0.026)	(26.3 0.038)				
11	496	(14.8 6.760)	(16.0 0.034)	(17.9 0.031)	(26.3 0.051)				
12	556	(14.8 4.120)	(16.0 0.043)	(17.9 0.033)	(26.3 0.053)				
13	616	(14.8 1.836)	(16.0 0.045)	(17.9 0.034)	(26.3 0.042)				

14 676 (14.8 0.708) (16.0 0.036) (17.9 0.034) (26.3 0.040)

Concentration measurement at station E, x = 14.20 m, with 14 records

no.	time (min)	elev (cm)	C (g/l)	elev (cm)	C (g/l)
1	0.00	(15.2, 0.000)	(26.9, 0.000)		
2	10.00	(15.2, 0.004)	(26.9, 0.004)		
3	60.00	(15.2, 0.009)	(26.9, 0.008)		
4	120.00	(15.2, 0.009)	(26.9, 0.008)		
5	180.00	(15.2, 0.010)	(26.9, 0.006)		
6	240.00	(15.2, 0.011)	(26.9, 0.007)		
7	300.00	(15.2, 0.010)	(26.9, 0.009)		
8	320.00	(15.2, 0.011)	(26.9, 0.006)		
9	376.00	(15.2, 0.014)	(26.9, 0.011)		
10	436.00	(15.2, 0.012)	(26.9, 0.008)		
11	496.00	(15.2, 0.022)	(26.9, 0.012)		
12	556.00	(15.2, 0.015)	(26.9, 0.009)		
13	616.00	(15.2, 0.020)	(26.9, 0.015)		
14	676.00	(15.2, 0.018)	(26.9, 0.012)		

Bed elevation (cm) information

Elapsed Time, x (m)=..

min 5.57 6.57 7.57 8.57 9.57 10.57 11.57 12.57

0	15.35	15.35	15.15	14.95	14.45	13.95	13.15	13.15
5	14.05	14.75	14.65	14.05	13.55	13.45	14.05	14.65
48	13.65	14.25	14.65	14.35	13.85	13.50	13.45	14.05
75	13.55	14.15	14.65	14.25	13.65	13.55	13.40	14.00
130	13.35	14.35	14.45	13.75	13.05	13.15	14.00	14.20
188	13.15	14.15	14.15	13.35	12.80	13.00	13.65	14.40
247	12.85	13.85	13.75	12.85	12.65	13.00	13.75	14.60
295	12.55	13.65	13.55	12.65	12.65	12.95	13.75	14.65
306	11.65	12.65	13.15	13.25	13.55	13.75	13.95	14.35
310	11.15	12.35	12.85	13.25	13.65	13.85	14.15	14.55
330	10.85	12.05	12.75	13.05	13.65	13.95	14.45	14.80
383	10.85	12.05	12.65	13.05	13.65	14.10	14.45	14.80
435	10.85	12.15	12.75	12.95	13.65	14.05	14.35	14.75
511	10.85	12.15	12.75	12.95	13.15	13.95	14.35	14.65
596	10.75	12.05	12.75	13.00	13.45	13.85	14.30	14.65
629	10.75	11.85	12.75	13.00	13.45	13.85	14.25	14.60
679	10.75	11.85	12.75	13.00	13.45	13.85	14.25	14.60

D.1.4 Run 4, Cedar Key Mud, SWL = 0.356 mConcentration measurement at station A, $x = 1.47$ m, with 14 records

Conc. probe elevation (cm) = 22 cm

Suspended sediment concentration (g/l) at each time step (same as station B, not shown) are listed below.

0.011	0.018	0.031	0.035	0.038	0.046	0.051	0.032	0.057	0.102
0.203	0.289	0.345	0.402						

Concentration measurement at station B, $x = 5.93$ m, with 14 records

no	time (min)	elev (cm)	C (g/l)	elev (cm)	C (g/l)	elev (cm)	C (g/l)	elev (cm)	C (g/l)
----	---------------	--------------	------------	--------------	------------	--------------	------------	--------------	------------

1	0	(12.0	0.086)	(13.1	0.075)	(14.9	0.028)	(23.3	0.015)
2	10	(12.0	0.080)	(13.1	0.067)	(14.9	0.060)	(23.3	0.044)
3	30	(12.0	0.060)	(13.1	0.048)	(14.9	0.044)	(23.3	0.035)
4	90	(12.0	0.465)	(13.1	0.225)	(14.9	0.123)	(23.3	0.071)
5	150	(12.0	0.118)	(13.1	0.094)	(14.9	0.080)	(23.3	0.075)
6	210	(11.0	0.334)	(12.1	0.107)	(13.9	0.085)	(22.3	0.073)
7	285	(11.0	0.560)	(12.1	0.205)	(13.9	0.158)	(22.3	0.118)
8	298	(11.0	1.378)	(12.1	1.137)	(13.9	0.766)	(22.3	0.266)
9	318	(9.0	2.189)	(10.1	1.394)	(11.9	0.854)	(20.3	0.491)
10	348	(7.0	8.568)	(8.1	3.072)	(9.9	1.306)	(18.3	0.650)
11	408	(7.5	29.580)	(8.6	1.305)	(10.4	0.745)	(18.8	0.560)
12	468	(7.5	28.310)	(8.6	1.596)	(10.4	0.974)	(18.8	0.524)
13	528	(7.5	21.589)	(8.6	1.004)	(10.4	0.577)	(18.8	0.515)
14	588	(7.5	11.640)	(8.6	0.980)	(10.4	0.738)	(18.8	0.592)

Concentration measurement at station C, $x = 8.50$ m, with 14 records

no	time (min)	elev (cm)	C (g/l)	elev (cm)	C (g/l)	elev (cm)	C (g/l)
----	---------------	--------------	------------	--------------	------------	--------------	------------

1	0	(11.4	0.086)	(12.5	0.075)	(14.4	0.028)	(22.7	0.015)
2	10	(11.4	0.066)	(12.5	0.066)	(14.4	0.037)	(22.7	0.017)
3	30	(11.4	0.123)	(12.5	0.098)	(14.4	0.052)	(22.7	0.028)
4	90	(11.4	0.342)	(12.5	0.320)	(14.4	0.117)	(22.7	0.037)
5	150	(11.4	2.196)	(12.5	0.375)	(14.4	0.126)	(22.7	0.054)
6	210	(11.4	2.056)	(12.5	0.122)	(14.4	0.083)	(22.7	0.062)
7	285	(11.4	0.745)	(12.5	0.154)	(14.4	0.103)	(22.7	0.077)
8	298	(11.4	2.840)	(12.5	0.285)	(14.4	0.208)	(22.7	0.097)
9	318	(9.4	1.888)	(10.5	1.086)	(12.4	0.754)	(20.7	0.190)
10	348	(9.4	2.908)	(10.5	1.050)	(12.4	0.510)	(20.7	0.392)
11	408	(9.4	5.740)	(10.5	0.774)	(12.4	0.732)	(20.7	0.380)
12	468	(9.4	8.040)	(10.5	0.550)	(12.4	0.452)	(20.7	0.384)
13	528	(9.4	15.973)	(10.5	0.546)	(12.4	0.448)	(20.7	0.408)
14	588	(9.4	12.250)	(10.5	0.726)	(12.4	0.622)	(20.7	0.458)

Concentration measurement at station D, $x = 12.30$ m, with 14 records

	no	time	elev	C	elev	C	elev	C	elev	C
	(min)	(cm)	(g/l)	(cm)	(g/l)	(cm)	(g/l)	(cm)	(g/l)	-
1	0	(12.0	0.086)	(13.2	0.075)	(15.1	0.028)	(23.5	0.015)	
2	10	(12.0	0.085)	(13.2	0.088)	(15.1	0.040)	(23.5	0.018)	
3	30	(12.0	0.692)	(13.2	0.300)	(15.1	0.084)	(23.5	0.020)	
4	90	(12.0	1.624)	(13.2	0.450)	(15.1	0.165)	(23.5	0.046)	
5	150	(12.0	0.422)	(13.2	0.147)	(15.1	0.117)	(23.5	0.064)	
6	210	(12.0	0.378)	(13.2	0.153)	(15.1	0.105)	(23.5	0.085)	
7	285	(12.0	0.212)	(13.2	0.100)	(15.1	0.092)	(23.5	0.083)	
8	298	(12.0	6.480)	(13.2	0.360)	(15.1	0.117)	(23.5	0.097)	
9	318	(13.5	5.720)	(14.7	0.488)	(16.6	0.244)	(25.0	0.094)	
10	348	(13.5	1.035)	(14.7	0.779)	(16.6	0.662)	(25.0	0.103)	
11	408	(13.5	0.729)	(14.7	0.578)	(16.6	0.402)	(25.0	0.212)	
12	468	(11.5	2.896)	(12.7	0.468)	(14.6	0.268)	(23.0	0.268)	
13	528	(11.5	1.044)	(12.7	0.300)	(14.6	0.272)	(23.0	0.248)	
14	588	(11.0	6.756)	(12.2	0.782)	(14.1	0.317)	(22.5	0.255)	

Concentration measurement at station E, $x = 14.20$ m, with 14 records

	no.	time	elev	C	elev	C
	(min)	(cm)	(g/l)	(cm)	(g/l)	
1	0.00	(15.2,	0.011)	(26.9,	0.005)	
2	10.00	(15.2,	0.018)	(26.9,	0.010)	
3	30.00	(15.2,	0.011)	(26.9,	0.006)	
4	90.00	(15.2,	0.022)	(26.9,	0.022)	
5	150.00	(15.2,	0.040)	(26.9,	0.032)	
6	210.00	(15.2,	0.049)	(26.9,	0.051)	
7	285.00	(15.2,	0.066)	(26.9,	0.057)	
8	298.00	(15.2,	0.089)	(26.9,	0.069)	
9	318.00	(15.2,	0.075)	(26.9,	0.063)	
10	348.00	(15.2,	0.282)	(26.9,	0.123)	
11	408.00	(15.2,	0.229)	(26.9,	0.211)	
12	468.00	(15.2,	0.249)	(26.9,	0.235)	
13	528.00	(15.2,	0.240)	(26.9,	0.235)	
14	588.00	(15.2,	0.254)	(26.9,	0.082)	

Bed elevation (cm) information

Elapsed Time, x (m)= ...	min	5.57	6.57	7.57	8.57	9.57	10.57	11.57	12.57
0	9.61	9.20	9.30	8.85	8.65	8.85	9.45	10.10	
109	9.65	9.15	9.25	8.85	8.65	8.85	9.45	10.15	
212	9.65	8.65	9.25	8.85	8.65	8.80	9.40	10.15	
253	9.60	8.55	9.30	8.85	8.60	8.80	9.45	10.20	
294	8.25	8.45	8.75	9.98	9.05	9.05	10.15	10.50	
307	6.65	7.15	7.45	8.75	9.95	10.95	11.75	12.30	
338	6.15	6.85	7.10	8.60	9.70	11.20	11.85	12.55	

363	7.15	7.45	7.50	8.70	9.55	10.35	11.30	11.75
459	7.55	7.45	7.45	8.95	9.15	9.70	10.55	11.05
535	7.15	7.20	7.55	8.85	9.25	9.70	10.30	10.95
585	7.00	7.00	7.85	8.95	9.25	9.75	10.30	10.85
635	7.00	7.00	7.85	8.95	9.25	9.75	10.30	10.85

D.1.5 Run 5, Cedar Key Mud, SWL = 0.356Concentration measurement at station A, $x = 1.47$ m, with 14 records

Conc. probe elevation (cm) = 22 cm

Suspended sediment concentration (g/l) at each time step (same as station B, not shown) are listed below.

0.126	0.097	0.085	0.282	0.446	0.704	0.836	0.898	0.964	1.095
1.435	1.796	1.944	2.136						

Concentration measurement at station B, $x = 5.93$ m, with 14 records

no	time (min)	elev (cm)	C (g/l)	elev (cm)	C (g/l)	elev (cm)	C (g/l)	elev (cm)	C (g/l)
----	---------------	--------------	------------	--------------	------------	--------------	------------	--------------	------------

1	0	(15.6 0.146)	(16.7 0.115)	(18.5 0.111)	(26.9 0.042)				
2	10	(15.6 3.410)	(16.7 1.110)	(18.5 0.698)	(26.9 0.110)				
3	30	(15.6 6.290)	(16.7 1.350)	(18.5 0.904)	(26.9 0.170)				
4	80	(15.6 11.725)	(16.7 2.873)	(18.5 1.152)	(26.9 0.218)				
5	110	(16.1 18.260)	(17.2 3.912)	(19.0 1.302)	(27.4 0.260)				
6	170	(16.1 15.287)	(17.2 3.540)	(19.0 1.116)	(27.4 0.430)				
7	230	(16.1 16.013)	(17.2 3.528)	(19.0 1.166)	(27.4 0.612)				
8	247	(15.6 28.040)	(16.7 8.036)	(18.5 4.304)	(26.9 1.448)				
9	267	(15.6 12.520)	(16.7 5.635)	(18.5 1.605)	(26.9 0.836)				
10	297	(15.6 15.333)	(16.7 5.873)	(18.5 1.748)	(26.9 0.945)				
11	357	(15.6 15.320)	(16.7 6.207)	(18.5 2.580)	(26.9 1.148)				
12	417	(15.6 12.307)	(16.7 6.033)	(18.5 2.512)	(26.9 1.208)				
13	477	(15.6 10.760)	(16.7 6.433)	(18.5 3.036)	(26.9 1.585)				
14	537	(15.6 7.787)	(16.7 5.833)	(18.5 3.612)	(26.9 1.753)				

Concentration measurement at station C, $x = 8.50$ m, with 14 records

no	time (min)	elev (cm)	C (g/l)	elev (cm)	C (g/l)	elev (cm)	C (g/l)	elev (cm)	C (g/l)
----	---------------	--------------	------------	--------------	------------	--------------	------------	--------------	------------

1	0	(16.6 0.146)	(17.7 0.115)	(19.6 0.111)	(27.9 0.042)				
2	10	(16.6 1.280)	(17.7 0.530)	(19.6 0.352)	(27.9 0.090)				
3	30	(16.6 1.488)	(17.7 0.545)	(19.6 0.370)	(27.9 0.077)				
4	80	(16.6 2.580)	(17.7 0.522)	(19.6 0.353)	(27.9 0.148)				
5	110	(16.6 2.224)	(17.7 0.660)	(19.6 0.328)	(27.9 0.196)				
6	170	(16.6 3.452)	(17.7 1.268)	(19.6 0.618)	(27.9 0.364)				
7	230	(16.6 3.308)	(17.7 1.310)	(19.6 0.840)	(27.9 0.536)				
8	247	(16.6 4.680)	(17.7 2.164)	(19.6 0.944)	(27.9 0.660)				
9	267	(16.6 5.084)	(17.7 2.736)	(19.6 1.012)	(27.9 0.600)				
10	297	(16.3 5.245)	(17.4 3.340)	(19.3 1.328)	(27.6 0.688)				

11	357	(16.3	6.667)	(17.4	4.387)	(19.3	1.776)	(27.6	0.944)
12	417	(16.3	7.186)	(17.4	4.967)	(19.3	2.360)	(27.6	1.165)
13	477	(16.3	8.146)	(17.4	5.586)	(19.3	2.847)	(27.6	1.340)
14	537	(16.3	7.880)	(17.4	5.627)	(19.3	3.187)	(27.6	1.555)

Concentration measurement at station D, $x = 12.30$ m, with 14 records

no	time (min)	elev (cm)	C (g/l)	elev (cm)	C (g/l)	elev (cm)	C (g/l)	elev (cm)	C (g/l)
1	0	(16.8	0.146)	(18.7	0.115)	(20.6	0.111)	(28.3	0.042)
2	10	(16.8	1.752)	(18.7	0.178)	(20.6	0.104)	(28.3	0.029)
3	30	(16.8	2.788)	(18.7	0.275)	(20.6	0.242)	(28.3	0.020)
4	80	(16.4	3.332)	(18.3	0.376)	(20.2	0.195)	(27.9	0.072)
5	110	(16.4	2.068)	(18.3	0.673)	(20.2	0.345)	(27.9	0.074)
6	170	(16.4	2.564)	(18.3	1.340)	(20.2	0.540)	(27.9	0.185)
7	230	(16.4	2.384)	(18.3	1.460)	(20.2	0.724)	(27.9	0.297)
8	247	(16.4	7.633)	(18.3	1.800)	(20.2	0.745)	(27.9	0.270)
9	267	(16.4	14.380)	(18.3	2.256)	(20.2	1.088)	(27.9	0.412)
10	297	(16.4	8.973)	(18.3	3.268)	(20.2	1.072)	(27.9	0.458)
11	357	(16.4	14.193)	(18.3	4.793)	(20.2	1.892)	(27.9	0.678)
12	417	(16.4	8.667)	(18.3	4.027)	(20.2	2.136)	(27.9	0.835)
13	477	(16.4	8.752)	(18.3	4.215)	(20.2	2.930)	(27.9	1.116)
14	537	(16.4	7.533)	(18.3	4.727)	(20.2	3.160)	(27.9	1.692)

Concentration measurement at station E, $x = 14.20$ m, with 14 records

no.	time (min)	elev (cm)	C (g/l)	elev (cm)	C (g/l)
1	0.00	(15.2,	0.226)	(26.9,	0.011)
2	10.00	(15.2,	2.492)	(26.9,	0.030)
3	30.00	(15.2,	1.964)	(26.9,	0.034)
4	80.00	(15.2,	4.304)	(26.9,	0.127)
5	110.00	(15.2,	4.147)	(26.9,	0.147)
6	170.00	(15.2,	4.527)	(26.9,	0.235)
7	230.00	(15.2,	5.747)	(26.9,	0.306)
8	247.00	(15.2,	6.873)	(26.9,	0.320)
9	267.00	(15.2,	7.793)	(26.9,	0.375)
10	297.00	(15.2,	9.112)	(26.9,	0.420)
11	357.00	(15.2,	12.450)	(26.9,	0.648)
12	417.00	(15.2,	8.220)	(26.9,	0.744)
13	477.00	(15.2,	8.387)	(26.9,	1.028)
14	537.00	(15.2,	8.410)	(26.9,	1.185)

Bed elevation (cm) information

Elapsed Time	x (m)= ...	5.57	6.57	7.57	8.57	9.57	10.57	11.57	12.57
min									

0	15.75	16.55	16.85	16.60	16.65	16.15	14.85	15.10
5	14.45	15.45	15.55	16.05	16.25	16.55	16.55	16.45
23	14.55	15.45	15.85	16.25	16.25	16.35	16.55	16.45

49	14.95	15.55	15.75	16.15	16.15	16.25	16.35	16.45
75	15.15	15.45	15.85	15.95	16.05	16.15	16.25	16.35
139	15.35	15.35	15.55	15.75	15.65	15.85	16.15	16.15
228	15.35	15.35	15.35	15.55	15.25	15.55	15.95	16.05
260	15.25	15.35	15.15	15.45	15.45	15.55	15.75	15.95
285	15.25	15.25	15.25	15.35	15.15	15.35	15.95	15.75
348	15.35	14.85	14.85	14.85	14.95	15.15	15.65	15.65
423	15.15	14.65	14.85	14.55	14.65	15.05	15.45	15.45
470	15.05	14.55	14.75	14.55	14.85	14.95	15.25	15.25
538	15.05	14.55	14.75	14.55	14.85	14.95	15.25	15.25

D.1.6 Run 6, Cedar Key Mud, SWL = 0.356 mConcentration measurement at station A, $x = 1.47$ m, with 18 records

Conc. probe elevation (cm) = 22 cm

Suspended sediment concentration (g/l) at each time step (same as station B, not shown) are listed below.

0.018	0.043	0.037	0.045	0.148	0.238	0.252	0.360	0.490	0.628
0.732	0.884	0.948	1.020	1.156	1.275	1.395	1.305		

Concentration measurement at station B, $x = 5.93$ m, with 18 records

no	time (min)	elev (cm)	C (g/l)	elev (cm)	C (g/l)	elev (cm)	C (g/l)	elev (cm)	C (g/l)
1	0	(11.7	0.058)	(12.8	0.024)	(15.1	0.006)	(23.0	0.008)
2	10	(11.7	0.017)	(12.8	0.012)	(15.1	0.010)	(23.0	0.002)
3	30	(11.7	23.333)	(12.8	4.446)	(15.1	0.576)	(23.0	0.044)
4	60	(12.7	15.540)	(13.8	6.900)	(16.1	1.586)	(24.0	0.078)
5	120	(12.2	12.970)	(13.3	6.190)	(15.6	3.460)	(23.5	0.112)
6	180	(12.2	10.580)	(13.3	3.893)	(15.6	3.140)	(23.5	0.172)
7	195	(10.7	17.610)	(11.8	4.847)	(14.1	3.567)	(22.0	0.377)
8	215	(11.2	24.400)	(12.3	3.800)	(14.6	2.927)	(22.5	0.580)
9	245	(11.3	13.490)	(12.4	2.893)	(14.7	2.253)	(22.6	0.849)
10	305	(11.3	13.360)	(12.4	3.660)	(14.7	2.360)	(22.6	0.832)
11	365	(11.3	13.637)	(12.4	2.953)	(14.7	2.080)	(22.6	0.995)
12	425	(11.3	11.020)	(12.4	2.320)	(14.7	1.710)	(22.6	1.125)
13	440	(12.2	8.070)	(13.3	1.620)	(15.6	1.630)	(23.5	1.370)
14	460	(12.2	8.790)	(13.3	1.495)	(15.6	1.475)	(23.5	1.410)
15	490	(12.2	6.140)	(13.3	1.735)	(15.6	1.475)	(23.5	1.415)
16	550	(11.7	4.000)	(12.8	1.872)	(15.1	1.565)	(23.0	1.490)
17	610	(11.4	6.690)	(12.5	1.865)	(14.8	1.680)	(22.7	1.540)
18	670	(11.4	5.690)	(12.5	1.915)	(14.8	1.780)	(22.7	1.615)

Concentration measurement at station C, $x = 8.50$ m, with 11 records

no	time (min)	elev (cm)	C (g/l)	elev (cm)	C (g/l)	elev (cm)	C (g/l)	elev (cm)	C (g/l)
1	0	(11.5	0.058)	(12.6	0.024)	(14.5	0.006)	(22.8	0.008)
2	10	(11.5	16.940)	(12.6	1.507)	(14.5	0.249)	(22.8	0.006)
3	30	(12.0	14.010)	(13.1	1.927)	(15.0	0.406)	(23.3	0.024)

4	60	(11.5 21.030)	(12.6 5.080)	(14.5 1.884)	(22.8 0.074)
5	120	(11.5 10.980)	(12.6 5.430)	(14.5 3.413)	(22.8 0.075)
6	180	(11.9 12.290)	(13.0 4.010)	(14.9 2.800)	(23.2 0.120)
7	195	(12.0 13.440)	(13.1 3.400)	(15.0 2.633)	(23.3 0.374)
8	215	(11.6 9.680)	(12.7 3.600)	(14.6 2.113)	(22.9 0.558)
9	245	(11.6 9.660)	(12.7 3.385)	(14.6 2.065)	(22.9 0.756)
10	305	(11.6 9.350)	(12.7 3.133)	(14.6 2.090)	(22.9 0.972)
11	365	(11.6 8.640)	(12.7 3.200)	(14.6 1.868)	(22.9 1.095)

Concentration measurement at station D, $x = 12.30$ m, with 18 records

no.	time (min)	elev (cm)	C (g/l)	elev (cm)	C (g/l)	elev (cm)	C (g/l)
1	0	(13.0 0.058)	(14.2 0.024)	(16.2 0.006)	(24.5 0.008)		
2	10	(13.0 8.800)	(14.2 0.412)	(16.2 0.066)	(24.5 0.008)		
3	30	(13.7 9.750)	(15.0 0.566)	(16.9 0.046)	(25.2 0.016)		
4	60	(15.0 14.860)	(16.3 0.320)	(18.2 0.084)	(26.5 0.028)		
5	120	(15.3 5.610)	(16.6 0.468)	(18.5 0.144)	(26.8 0.032)		
6	180	(15.3 10.130)	(16.6 0.804)	(18.5 0.174)	(26.8 0.074)		
7	195	(15.3 10.740)	(16.6 1.587)	(18.5 0.756)	(26.8 0.082)		
8	215	(15.0 4.253)	(16.3 1.580)	(18.2 1.356)	(26.5 0.106)		
9	245	(14.9 7.207)	(16.2 1.660)	(18.1 1.340)	(26.4 0.238)		
10	305	(14.9 4.393)	(16.2 1.452)	(18.1 1.340)	(26.4 0.520)		
11	365	(14.9 8.106)	(16.2 1.368)	(18.1 1.360)	(26.4 0.724)		
12	425	(14.5 6.600)	(15.7 1.415)	(17.7 1.264)	(26.0 0.780)		
13	440	(14.0 5.210)	(15.2 1.750)	(17.2 1.048)	(25.5 0.660)		
14	460	(14.0 6.340)	(15.2 1.368)	(17.2 1.055)	(25.5 0.760)		
15	490	(14.0 6.810)	(15.2 1.285)	(17.2 1.060)	(25.5 0.816)		
16	550	(14.0 5.313)	(15.2 1.130)	(17.2 0.992)	(25.5 0.884)		
17	610	(14.0 5.513)	(15.2 1.180)	(17.2 1.008)	(25.5 0.936)		
18	670	(14.0 15.310)	(15.2 1.275)	(17.2 1.112)	(25.5 0.952)		

Concentration measurement at station E, $x = 14.2$ m, with 18 records

no.	time (min)	elev (cm)	C (g/l)	elev (cm)	C (g/l)
1	0.00	(15.2, 0.018)	(26.9, 0.015)		
2	10.00	(15.2, 0.115)	(26.9, 0.018)		
3	30.00	(15.2, 0.166)	(26.9, 0.032)		
4	60.00	(15.2, 0.456)	(26.9, 0.034)		
5	120.00	(15.2, 0.520)	(26.9, 0.040)		
6	180.00	(15.2, 0.852)	(26.9, 0.054)		
7	195.00	(15.2, 2.325)	(26.9, 0.050)		
8	215.00	(15.2, 4.027)	(26.9, 0.106)		
9	245.00	(15.2, 6.533)	(26.9, 0.123)		
10	305.00	(15.2, 7.050)	(26.9, 0.432)		
11	365.00	(15.2, 5.910)	(26.9, 0.640)		
12	425.00	(15.2, 5.160)	(26.9, 0.856)		
13	440.00	(15.2, 4.750)	(26.9, 0.570)		
14	460.00	(15.2, 4.590)	(26.9, 0.770)		
15	490.00	(15.2, 3.940)	(26.9, 0.672)		
16	550.00	(15.2, 2.490)	(26.9, 0.836)		

17 610.00 (15.2, 1.787) (26.9, 0.944)
 18 670.00 (15.2, 1.245) (26.9, 1.005)

Bed elevation (cm) information

Elapsed Time	x (m)...	5.57	6.57	7.57	8.57	9.57	10.57	11.57	12.57
0	11.00	11.15	11.30	11.25	11.65	12.05	11.95	12.15	
40	11.80	11.75	11.15	11.45	11.35	12.85	14.05	13.75	
69	12.15	11.35	11.25	11.30	11.20	12.45	14.00	15.05	
107	11.25	11.15	11.00	11.35	11.40	12.35	13.95	14.85	
148	11.15	11.15	10.95	11.15	11.40	12.15	13.70	14.80	
190	9.85	10.45	11.45	12.05	12.00	12.30	12.45	15.25	
228	10.55	10.55	11.05	11.05	10.95	12.45	12.95	15.20	
264	10.75	10.55	10.90	10.75	11.15	12.35	13.05	14.85	
326	10.75	10.10	10.75	10.65	11.05	12.35	13.15	14.50	
350	10.95	10.15	10.70	10.55	11.25	12.40	13.40	14.45	
394	10.95	10.25	10.55	10.55	11.30	12.50	13.45	14.25	
421	10.95	10.45	10.55	10.55	11.35	12.50	13.45	14.05	
477	11.45	10.30	10.80	10.55	11.35	12.25	13.15	13.90	
518	11.25	10.45	10.45	10.25	10.35	12.35	13.05	14.05	
597	10.95	10.65	10.55	10.15	11.15	12.15	12.95	13.90	
646	10.85	10.65	10.55	10.15	11.15	12.15	13.05	14.00	
672	10.55	10.45	10.75	10.95	11.00	12.15	13.05	14.05	
675	10.55	10.45	10.75	10.95	11.00	12.15	13.05	14.05	

D.2 Plots of Wave Loading, pp. 253-255.

D.3 Plots of Wave-averaged Pressure, pp. 256-258.

D.4 Plots of Average Dynamic Pressure, pp. 258-260.

D.5 Plots of Apparent Density Variation due to Wave Action, PP. 261-263.

D.6 Plots of Variation of Density Profile, pp. 264-268.

D.7 Plots of Light Meter Responses for Run 6, p. 269.

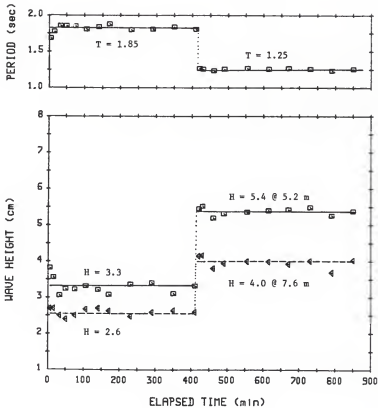


Fig. D-1. Wave Loading for the Wave Erosion Test, Run 1.

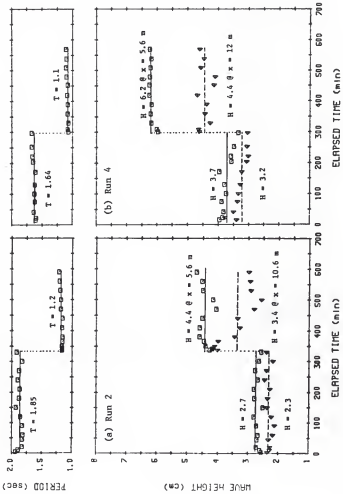


Fig. D-2. Wave Loading for the Wave Erosion Test. (a) Run 2; (b) Run 4.

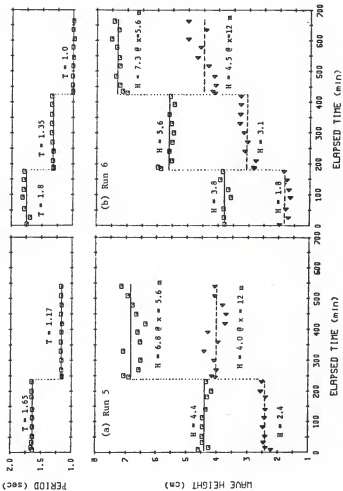


Fig. D-3. Wave Loading for the Wave Erosion Test. (a) Run 5; (b) Run 6.

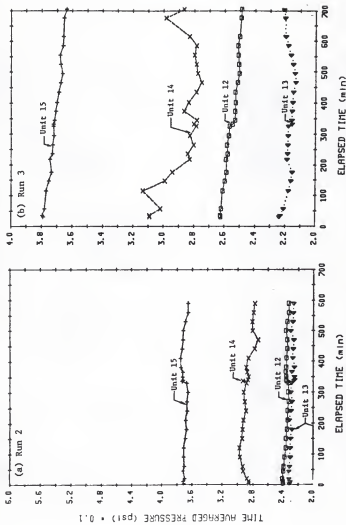


FIG. D-4. Wave-Averaged Pressure Response in the Mud Bed. (a) Run 2; (b) Run 3.

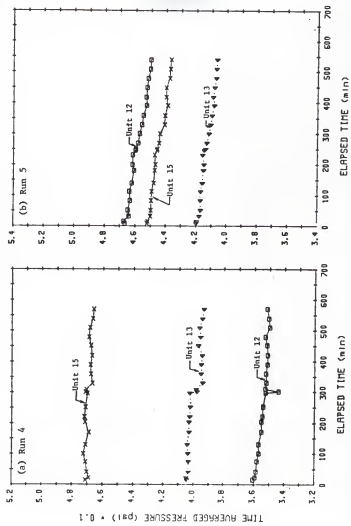


FIG. D-5. Wave-Averaged Pressure Response in the Mud Bed. (a) Run 4; (b) Run 5.

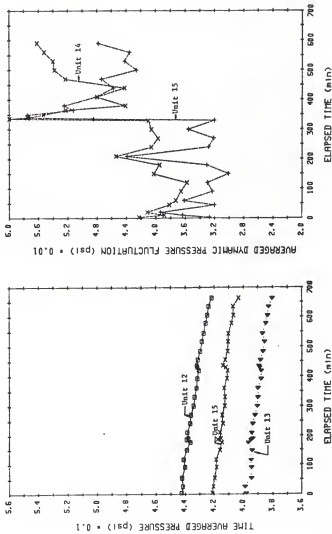


Fig. D-6. Time-Averaged Pressure Response
in the Mud Bed, Run 6.

Fig. D-7. Average Dynamic Pressure Fluctuation
in the Mud Bed, Run 2.

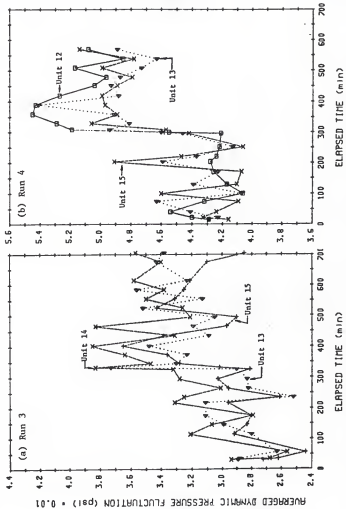


Fig. D-8. Average Dynamic Pressure Fluctuation in the Mud Bed. (a) Run 3; (b) Run 4.

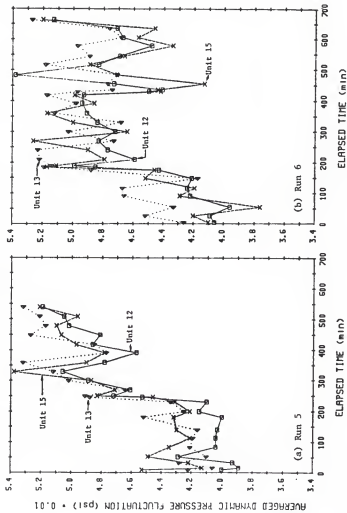


Fig. D-9. Average Dynamic Pressure Fluctuation in the Mud Bed. (a) Run 5; (b) Run 6.

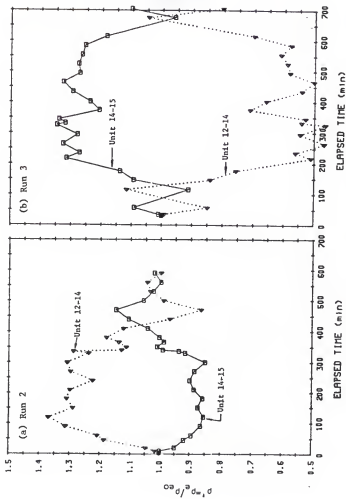


Fig. D-10. Average Apparent Bulk Density Variation due to Wave Action. (a) Run 2; (b) Run 3.

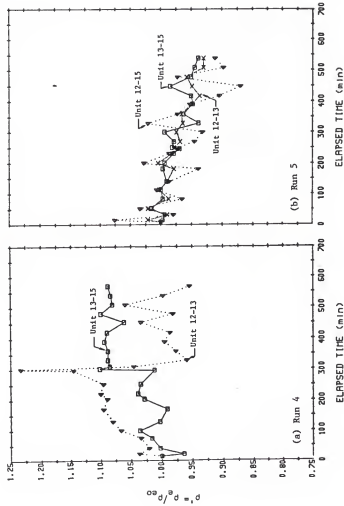


Fig. D-11. Average Apparent Bulk Density Variation due to Wave Action. (a) Run 4; (b) Run 5.

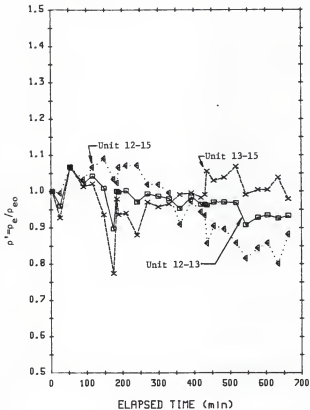


Fig. D-12. Average Apparent Bulk Density Variation due to Wave Action, Run 6.

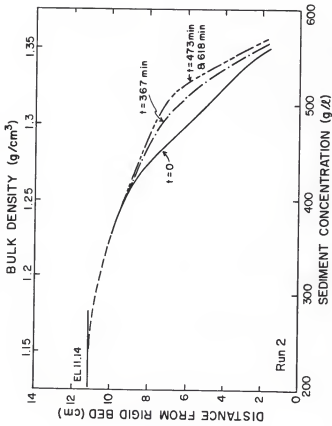
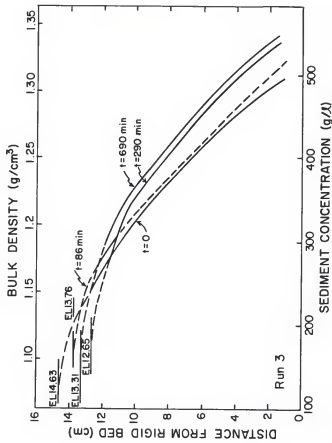


Fig. D-13. Variation of kaolinite bed density profile due to wave action, Run 2.



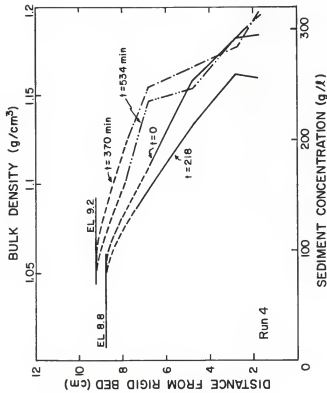


Fig. D-15. Variation of Cedar Key Mud Bed Density Profile Due to Wave Action, Run 4.

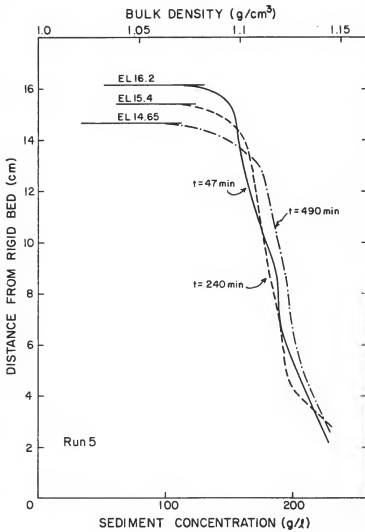


Fig. D-16. Variation of Cedar Key Mud Bed Density Profile due to Wave Action, Run 5.

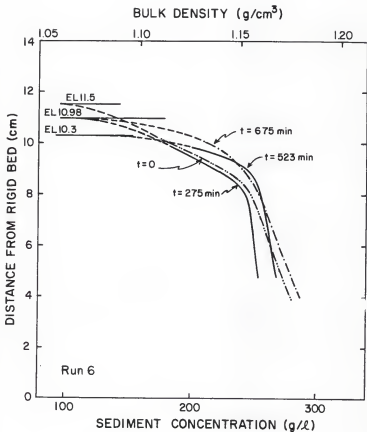


Fig. D-17. Variation of Cedar Key Mud Bed Density Profile due to Wave Action, Run 6.

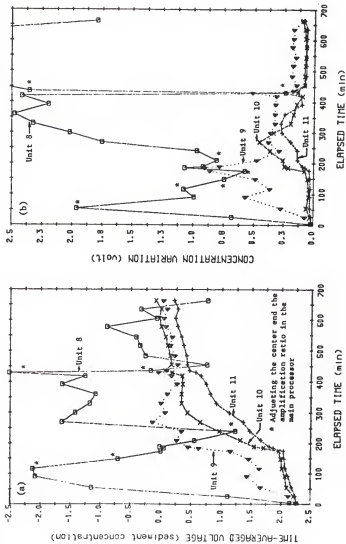


FIG. D-18. Wave-Averaged Response from Light Meter, Run 6. (a) Sediment Concentration; (b) Sediment Concentration Fluctuation.

REFERENCES

- Abbott, M. B., Computational Hydraulics, Pitman Advanced Publishing Program, Boston, 1980.
- Alishahi, M. R., and Krone, R. B., Suspension of Cohesive Sediment by Wind-generated Waves, Technical Report Hel-2-9, Hydraulic Engineering Laboratory, University of California, Berkeley, California, 1964.
- Anderson, F., "Resuspension of Estuarine Sediments by Small Amplitude Waves," Journal of Sedimentary Petrology, Vol. 42, No. 3, 1972, pp. 602-607.
- Ariathurai, C. R., A Finite Element Model of Cohesive Sediment Transportation, Ph.D. Dissertation, University of California, Davis, California, 1974.
- Awaya, Y., "Turbulent Dispersion in Periodic Flow," Proceedings of the 13th Congress of the IAHR, Sponsored by Science Council of Japan, Kyoto, Japan, 1969, pp. c 3.1-8.
- Bagnold, R. A., "Motions of Waves in Shallow Water: Interaction between Waves and Sand Bottoms," Proceedings of the Royal Society of London, Series A, Vol. 187, 1946, pp. 1-15.
- Black, C. A., Editor, Methods of Soil Analysis, Part 1, American Society of Agronomy, Inc., Madison, Wisconsin, 1965.
- Carpenter S. H., Thompson, L. J., and Bryant, W. R., "Viscoelastic Properties of Marine Sediments," Proceedings of the 5th Offshore Technology Conference, Vol. 2, OTC, Richardson, Texas, 1973, pp. 777-788.
- Chen, C.-L., "Present Status of Research in Debris Flow Modeling," Proceedings of the Special Conference, Hydraulics and Hydrology in the Small Computer Age, Sponsored by the Hydraulics Division, ASCE, Held at Lake Buena Vista, Florida, Aug. 12-17, 1985, Vol. 2, pp. 113-118.
- Chen, R. K.-C., Street, R. L., and Strelkoff, T., Computer Studies of Finite-amplitude Water Waves, Technical Report No. 104, Department of Civil Engineering, Stanford University, Stanford, California, 1969.
- Dalrymple, R. A., and Liu, P. L.-F., "Waves over Soft Muds: A Two-Layer Fluid Model," Journal of Physical Oceanography, Vol. 8, 1978, pp. 1121-1131.
- Das, M., Mechanics of Sediment Suspension Due to Oscillatory Water Waves, Technical Report Hel-2-32, University of California, Berkeley, California, 1971.

Das, B. M., Advanced Soil Mechanics, McGraw-Hill Book Co., New York, 1983.

Dawson, T. H., "Wave Propagation over a Deformable Sea Floor," Ocean Engineering, Vol. 5, 1978, pp. 227-234.

Dean, R. G., and Dalrymple, R. A., Water Wave Mechanics for Engineers and Scientists, Prentice-Hall, Inc., Englewood Cliffs, New Jersey, 1984.

Einstein, H. A., and Krone, R. B., "Experiments to Determine Modes of Cohesive Sediment Transport in Salt Water," Journal of Geophysical Research, Vol. 67, No. 4, 1962, pp. 1451-1461.

Engelund, F., and Wan, Z., "Instability of Hyperconcentrated Flow," Journal of Hydraulic Engineering, ASCE, Vol. 110, No. 3, 1984, pp. 219-232.

Fisher, H. B., "Dispersion Predictions in Natural Streams," Journal of the Sanitary Engineering Division, ASCE, Vol. 94, No. SA5, 1968, pp. 927-943.

Gade, H. G., "Effects of a Nonrigid Impermeable Bottom on Plane Surface Waves in Shallow Water," Journal of Marine Research, Vol. 16, No. 2, 1958, pp. 61-82.

Glover, J. R., Bhattacharya, P. K., and Kennedy, J. F., An Electro-optical System for Measurement of Mean and Statistical Properties of Sediment Suspensions, IIHR Report No.120, Iowa Institute of Hydraulic Research, The University of Iowa, Iowa City, Iowa, 1969.

Godaa, Y., and Suzuki, Y., "Estimation of Incident and Reflected Waves in Random Wave Experiments," Proceeding of the 15th Coastal Engineering Conference, ASCE, Vol. 1, 1976, pp. 828-845.

Goden, S. P., Godwin, J. W., and Olal, A. D., "The Dependence of the Elastic Properties of Clay Dispersions on the Mode of Interaction between Particles," Transactions and Journal, British Ceramic Society, Vol 81, No. 3, 1982, pp. 84-87.

Gularate, R. G., Erosion of Cohesive Sediment as a Rate Process, Ph.D. Dissertation, University of Rhode Island, Kingston, Rhode Island, 1978.

Hardin, B. O., and Drnevich, V. P., "Shear Modulus and Damping in Soils: Measurement and Parameter Effects," Journal of the Soil Mechanics and Foundations Division, ASCE, Vol. 98, No. SM6, 1972, pp. 603-624.

Harlow, F. H., and Welch, J. E., "Numerical Calculation of Time Dependent Viscous Incompressible Flow of Fluid with Free Surface," The Physics of Fluids, Vol. 8, No. 13, 1965, pp. 2182-2189.

Hattori, M., "The Mechanics of Suspended Sediment Due to Standing Waves," Coastal Engineering in Japan, Vol. 12, Tokyo, Japan, 1969, pp. 69-82.

Hayter, E., Prediction of Cohesive Sediment Movement in Estuarial Waters, Ph.D. Dissertation, University of Florida, Gainesville, Florida, 1983.

Hom-ma, M., and Horikawa, K., "A Laboratory Study on Suspended Sediment Due to Wave Action," Proceedings of Xth Congress of the IAHR, London, 1963.

Horikawa, K., and Watanabe, A., "Turbulence and Sediment Concentration Due to Waves," Coastal Engineering in Japan, Vol. 13, Tokyo, Japan, 1970, pp. 15-24.

Hsiao, S. Y., and Shemdin, O. H., "Interaction of Ocean Waves with a Soft Bottom," Journal of Physical Oceanography, Vol. 10, No. 4, 1980, pp. 605-610.

Hwang, P. A., and Wang, H., Wave Kinematics and Sediment Suspension at Wave Breaking Point, Technical Report No. 13, Department of Civil Engineering, University of Delaware, Newark, Delaware, 1982.

Jackson, J. R., A Model Study of the Effects of Small Amplitude Waves on the Resuspension of Fine-grain Cohesive Sediments, M.S. Thesis, University of New Hampshire, Durham, New Hampshire, 1973.

Jobson, H. E., and Sayre, W. W., "Vertical Transfer in Open Channel Flow," Journal of the Hydraulics Division, ASCE, Vol. 96, No. HY3, 1970, pp. 703-724.

Jonsson, I. G., "Wave Boundary Layer and Friction Factors," Proceedings of the 10th Coastal Engineering Conference, ASCE, Vol. 1, 1966, pp. 127-148.

Jonsson, I. G., "The Wave Friction Factor Revisited," in Progress Report No. 37, Institute of Hydrodynamics and Hydraulic Engineering, Technical University of Denmark, Lyngby, Denmark, 1975, pp. 3-8.

Jonsson, I. G., "A New Approach to Oscillatory Rough Turbulent Boundary Layers," Ocean Engineering, Vol. 7, 1980, pp. 109-152.

Jonsson, I. G., and Carlsen, N. A., "Experimental and Theoretical Investigations in An Oscillatory Turbulent Boundary Layer," Journal of Hydraulic Research, Vol. 14, No. 1, 1976, pp. 45-58.

Kamphuis, J. W., "Friction Factor under Oscillatory Waves," Journal of the Waterways, Harbors and Coastal Engineering Division, ASCE, Vol. 101, No. WW2, 1975, pp. 135-144.

- Kennedy, J. F., and Locher F. A., "Sediment Suspension by Water Waves," in Waves on Beaches and Resulting Sediment Transport, R. E. Meyer, Editor, Academic Press, New York, 1972.
- Kolsky, H., Stress Waves in Solids, Dover Publications, Inc., New York, 1963.
- Kovacs, A. M., Seed, H. B., and Chan, C. K., "Dynamic Moduli and Damping Ratios for a Soft Clay," Journal of the Soil Mechanics and Foundations Division, ASCE, Vol. 97, No. SM1, 1971, pp. 59-75.
- Krone, R. B., Flume Studies of the Transport of Sediment in the Estuarial Shoaling Process, University of California Hydraulic Engineering Laboratory and Sanitation Research Laboratory, Berkeley, California, 1962.
- Krone, R. B., A Study of Rheologic Properties of Estuarial Sediments, Technical Bulletin No. 7, Committee on Tidal Hydraulics, U.S. Army Corps of Engineers, Waterways Experiment Station, Vicksburg, Mississippi, 1965.
- Lofquist, K. E. B., "Measurements of Oscillatory Drag on Sand Ripples," Proceedings of the 17th Coastal Engineering Conference, ASCE, Sydney, Australia, 1980, pp. 3087-3106.
- Macpherson, H., "The Attenuation of Water Waves over a Non-rigid Bed," Journal of Fluid Mechanics, Vol. 97, Part 4, 1980, pp. 721-742.
- Mallard, W. W., and Dalrymple, R. A., "Water Waves Propagating over a Deformable Bottom," Proceedings of the 9th Offshore Technology Conference, Vol. 3, OTC, Richardson, Texas, 1977, pp. 141-146.
- Malvern, L. E., Introduction to the Mechanics of a Continuous Medium, Prentice-Hall Inc., Englewood Cliffs, New Jersey, 1969.
- McClave, J. T., and Benson, P. G., A First Course in Business Statistics, Dellen Publishing Co., San Francisco, California, 1981.
- Mehta, A. J., "Characterization Tests for Cohesive Sediments," Proceedings of Frontiers of Hydraulic Engineering Conference, ASCE, Cambridge, Massachusetts, 1983, pp. 79-84.
- Mehta, A. J., "Characterization of Cohesive Sediment Properties and Transport Processes in Estuaries," in Estuarine Cohesive Sediment Dynamics, A. J. Mehta, Editor, Lecture Notes on Coastal and Estuarine Studies, No. 14, Springer-Verlag, New York, 1986.
- Mehta, A. J., Parchure, T. M., Dixit, J. G., and Ariathurai, R., "Resuspension Potential of Deposited Cohesive Sediment Beds," in Estuarine Comparisons, V. S. Kennedy, Editor, Academic Press, New York, 1982, pp. 591-609.

Migniot, C., "A Study of the Physical Properties of Various Forms of Very Fine Sediment and their Behavior under Hydrodynamic Action," Houille Blanche, No. 7, 1968, pp. 591-620 (in French, with English abstract).

Morgan, J. P., VanLopik, J. R., and Nichols, L.G., Occurrence and Development of Mudflats along the Western Louisiana Coast, Technical Report No. 2, Coastal Studies Institute, Louisiana State University, 1953.

Nagai, T., Figueroa, J. L., and Yamamoto, T., Nonlinear Mechanics of Sea-bed Interactions, Part III—Wave Tank Experiments on Soil Mass Transport in Clay Beds Associated with Wave Damping, Rosenstiel School of Marine and Atmospheric Science, University of Miami, Miami, Florida, 1982.

Nielsen, P., Some Basic Concepts of Wave Sediment Transport, Series Paper No. 20, Institute of Hydrodynamics and Hydraulic Engineering, Technical University of Denmark, Lyngby, Denmark, 1979.

Nielsen, P., "On the Motion of Suspended Sand Particles," Journal of Geophysical Research, Vol. 89, No. c1, 1984, pp. 616-626.

Odd, N. V. W., and Owen, M. W., "A Two-layer Model of Mud Transport in the Thames Estuary," Proceedings of the Institution of Civil Engineers, London, Supplement No. 9, 1972, pp. 175-205.

Owen, M. W., "Problems in the Modeling of Transport, Erosion, and Deposition of Cohesive Sediments," in The Sea IV, Marine Modeling, E. D. Goldberg, I. N. McCave, J. J. O'Brien, and J. H. Steel, Editors, Wiley-Interscience, New York, 1977.

Pamukcu, S., Poplin, J. K., Suhayda J. N., and Tumay, M. T., "Dynamic Sediment Properties, Mississippi Delta," in Geotechnical Practice in Offshore Engineering, S. G. Wright, Editor, ASCE, 1983, pp. 111-132.

Parchure, T. M., Erosion Behavior of Deposited Cohesive Sediments, Ph.D. Dissertation, University of Florida, Gainesville, Florida, 1984.

Parchure, T. M., and Mehta, A. J., "Erosion of Soft Cohesive Sediment Deposits," Journal of Hydraulic Engineering, ASCE, Vol. 111, No. 10, 1985, pp. 1308-1326.

Parker, W. R., and Kirby, R., "Time Dependent Properties of Cohesive Sediment Relevant to Sedimentation Management—European Experience," in Estuarine Comparisons, Academic Press, New York, 1982.

Partheniades, E., "Erosion and Deposition of Cohesive Soils," Journal of the Hydraulics Division, ASCE, Vol. 91, No. HY1, 1965, pp. 105-139.

Pazwash, H., and Robertson, J. M., "Fluid-dynamic Consideration of Bottom Materials," Journal of the Hydraulic Division, ASCE, Vol. 97, No. HY9, 1971, pp. 1317-1329.

Prakash, S., Soil Dynamics, McGraw-Hill Book Co., New York, 1981.

Richart, F. E., Hall, J. R., and Woods, R. D., Vibrations of Soils and Foundations, Prentice-Hall, Inc., Englewood Cliffs, New Jersey, 1970.

Schapery, R. A., and Dunlap, W. A., "Prediction of Storm Induced Sea Bottom Movement and Platform Forces," Proceedings of the 10th Offshore Technology Conference, Vol. 3, OTC, Richardson, Texas, 1978, pp. 1789-1796.

Schuckman, B., and Yamamoto, T., Nonlinear Mechanics of Sea-bed Interactions, Part II: Wave Tank Experiments on Water Wave Damping by Motion of Clay Beds, Technical Report TR 82-1, Rosenstiel School of Marine and Atmospheric Science, University of Miami, Miami, Florida, 1982.

Sleath, J. F. A., "Velocity Measurements Close to the Bed in a Wave Tank," Journal of Fluid Mechanics, Vol. 42, Part 1, 1970, pp. 111-123.

Shinohara, K., Taubaki, Y., Yoshitaka, Y., and Agemori, C., Coastal Engineering in Japan, Vol. 1, Tokyo, Japan, 1958, pp. 111-130.

Stevenson, H. S., Vane Shear Determination of the Viscoelastic Shear Modulus of Submarine Sediments, M.S. Thesis, Texas A&M University, College Station, Texas, 1973.

Taylor, G. I., "The Dispersion of Matter in Turbulent Flow through a Pipe," Proceedings of the Royal Society of London, Series A, Vol. 223, 1954, pp. 446-468.

Thiers, G. R., and Seed, H. B., "Cyclic Stress-Strain Characteristics of Clays," Journal of the Soil Mechanics and Foundations Division, ASCE, Vol. 94, No. SM2, 1968, pp. 555-569.

Thimakorn, P., "An Experiment of Clay Suspension under Water Waves," Proceedings of the 17th Coastal Engineering Conference, ASCE, Vol. 3, 1980, pp. 2894-2906.

Thimakorn, P., "Resuspension of Clays under Waves," in Seabed Mechanics, B. Denness, Editor, Graham & Trotman Ltd., London, 1984, pp. 191-196.

Tubman, M. W., and Suhayda, J. N., "Wave Action and Bottom Movements in Fine Sediments," Proceedings of the 15th Coastal Engineering Conference, ASCE, Vol. 2, 1976, pp. 1168-1183.

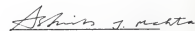
- Turcotte, B. R., Liu, P. L.-F., and Kulhawy, F. H., Laboratory Evaluation of Wave Tank Parameters for Wave-Sediment Interaction, Joseph H. DeFrees Hydraulics Laboratory Report 84-1 and Geotechnical Engineering Report 84-6, School of Civil and Environmental Engineering, Cornell University, Ithaca, New York, 1984.
- Vallejo, L. E., "Analysis of Wave-induced Erosion of Cohesive Soils Forming Coastal Bluffs," Proceedings of Canadian Coastal Conference, Burlington, Ontario, 1980, pp. 220-228.
- Vallejo, L. E., "An Explanation for Mud Flows," Geotechnique, Vol. 29, No. 3, 1979, pp. 351-354.
- Yamamoto, T., "On the Response of a Coulomb-damped Poroelastic Bed to Water Waves," Marine Geotechnology, Vol. 5, No. 2, 1982, pp. 93-130.
- Yamamoto, T., and Takahashi, S., "Wave Damping by Soil Motion," Journal of Waterway, Port, Coastal and Ocean Engineering, ASCE, Vol. 111, No. 1, 1985, pp. 62-77.
- Yeh, H.-Y., Resuspension Properties of Flow Deposited Cohesive Sediment Beds, M.S. Thesis, University of Florida, Gainesville, Florida, 1979.
- Wells, J. T., "Dynamics of Coastal Fluid Muds in Low-, Moderate-, and High-tide-range Environments," Canadian Journal of Fisheries and Aquatic Sciences, Vol. 40, Supplement No. 1, 1983, pp. 130-142.
- Wells, J. T., Coleman, J. M., and Wiseman, W. J., "Suspension and Transportation of Fluid Mud by Solitary Waves," Proceedings of the 16th Coastal Engineering Conference, ASCE, Vol. 2, 1978, pp. 1932-1952.
- Williams, D. J. A., and James, A. E., Rheology of Brisbane and Rotterdam Mud, Report, Commissioned by Hydraulics Research Station, University College, Swansea, Wales, United Kingdom, 1978.
- Wylie, C. R., Advanced Engineering Mathematics, 3rd ed. McGraw-Hill Book Co., New York, 1966.

BIOGRAPHICAL SKETCH

Peng-Yea Maa was born on December 7, 1948, in Peking, China. In 1949, his family moved to Taiwan. In 1970 he completed his college education with a bachelor's degree in hydraulic engineering. He then attended the graduate school at Chung-Kung University and graduated in 1972 with a master's degree in civil engineering. After a year of service in the military, he worked as a hydraulic engineer from July 1973 to December 1981. On March 8, 1976, he married Tai-Fang Fan. Nine years of practice inspired him to go abroad for further education.

He joined the University of Florida in January 1982 to work toward the Ph.D. degree in civil engineering. He was a graduate research assistant in the Coastal and Oceanographic Engineering Department throughout his doctoral study program.

I certify that I have read this study and that in my opinion it conforms to acceptable standards of scholarly presentation and is fully adequate, in scope and quality, as a dissertation for the degree of Doctor of Philosophy.



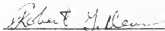
Ashish J. Mehta
Associate Professor of
Civil Engineering

I certify that I have read this study and that in my opinion it conforms to acceptable standards of scholarly presentation and is fully adequate, in scope and quality, as a dissertation for the degree of Doctor of Philosophy.



Bent A. Christensen, Cochairman
Professor of Civil Engineering

I certify that I have read this study and that in my opinion it conforms to acceptable standards of scholarly presentation and is fully adequate, in scope and quality, as a dissertation for the degree of Doctor of Philosophy.



Robert G. Dean
Graduate Research Professor of
Coastal and Oceanographic
Engineering

I certify that I have read this study and that in my opinion it conforms to acceptable standards of scholarly presentation and is fully adequate, in scope and quality, as a dissertation for the degree of Doctor of Philosophy.

Barry A. Benedict

Barry A. Benedict
Professor of Civil Engineering

I certify that I have read this study and that in my opinion it conforms to acceptable standards of scholarly presentation and is fully adequate, in scope and quality, as a dissertation for the degree of Doctor of Philosophy.

Arun K. Varma

Arun K. Varma
Professor of Mathematics

This dissertation was submitted to the Graduate Faculty of the College of Engineering and to the Graduate School and was accepted as partial fulfillment of the requirements for the degree of Doctor of Philosophy.

August, 1986

Herbet A. Bevis

Dean, College of Engineering

Dean, Graduate School

UNIVERSITY OF FLORIDA



3 1262 06554 8841